



CM-P00068841

Dissertation

*Decay and Snapback Studies on the LHC Dipole Model Magnets
A Scaling Law*

Michael Schneider

nr 0328323

Thesis-1998-Schneider

Dissertation

Decay and Snapback Studies on the LHC Dipole Model Magnets A Scaling Law

ausgeführt zum Zweck der Erlangung des akademischen Grades eines Doktors
der technischen Wissenschaften unter der Leitung von

o.Univ.Prof. Dipl.-Ing. Dr.techn. Hans Kirchmayr
Institut für Experimentalphysik, E 131, TU-Wien

Dr. Luca Bottura, Dr. Peter Sievers
CERN, LHC-MTA, Geneva, Switzerland

eingereicht an der Technischen Universität Wien
Technisch-naturwissenschaftliche Fakultät

von

Dipl.-Ing. Michael Schneider

Matr.Nr. 8725085

Enziangasse 9
A-2362 Biedermannsdorf

Wien, am

?

1998

↑ plus d'informations
sur p5 (experiments)

Deutsche Kurzfassung der Dissertation

Decay- und Snapback- Studien an den LHC-Dipol-Model-Magneten Ein Skalierungsgesetz

Beim Betrieb des Tevatron Beschleunigers wurde erstmals festgestellt, daß das Dipolfeld der supraleitenden Dipolmagnete beziehungsweise die Feldkomponenten höherer Ordnung (Feldfehler) dynamische Effekte (Decay und Snapback) aufweisen. Die Felddrift während des Strahlaufbaus (Injektion) zeigte nachhaltige Auswirkung auf Strahl-Parameter und die Strahl-Stabilität. Die Schwierigkeiten im Betrieb des Beschleunigers und die Probleme in der Vorhersage von dynamischen Effekten führten schließlich zum Entschluß die gesamte Population der supraleitenden HERA-Dipolmagnete unter kryogenischen Bedingungen zu messen. Die vorliegende Arbeit soll zeigen, daß diese kostspielige und zeitaufwendige Prozedur im Fall des Large Hadron Colliders (LHC) vermieden werden kann. Dazu haben wir an ein Meter langen LHC-Dipol-Magneten zwei Meßprogramme abgearbeitet.

Vom erste Programm, die sogenannten Standardmessungen, leiten wir statistische Zahlen, die Decay und Snapback charakterisieren, ab. Als wichtigstes Ergebnis finden wir, daß systematische Effekte nur auf den durch das Spulendesign erlaubten Feldkomponenten zu finden sind.

Das zweite Meßprogramm, die sogenannten Betriebszyklen-Experimente, zeigt die Auswirkung von Variationen der Betriebszyklen auf die dynamischen Effekte. Wegen der vorher erwähnten Systematik und der Bedeutung bezüglich Strahlstabilität konzentrieren wir uns auf das Verhalten der Sextupolkomponente des Dipolfeldes.

Die Ergebnisse der Betriebszyklen-Experimente werden im folgenden zum Modellieren der zu erwartenden Snapback-Amplitude als Funktion der Betriebszyklen verwendet. Wir zeigen die Möglichkeiten und Einschränkungen eines phänomenologischen Modells. Dieses Modell basiert auf der Vereinfachung eines theoretischen Stromdiffusionsmodells für das Rutherford-Kabel der supraleitenden Spulen. Die Anwendung neuronaler Netze zeigt schließlich wie das Problem der Vorhersage von dynamischen Effekten als Folge veränderlicher Betriebsbedingungen mit beliebiger Genauigkeit gelöst werden kann.

Eine abschließende statistische Simulation einer Serienmessung von Dipolmagneten zeigt uns wieviele Magneten unter kryogenischen Temperaturen gemessen werden müssen, um den Mittelwert der Sextupolkomponente der Population von Dipolmagneten mit entsprechender Genauigkeit vorhersagen zu können. Die Genauigkeit der Kenntnis dieses Mittelwertes ist durch die Anforderungen an die Kontrolle der Chromtizität gegeben.

Die Arbeit liefert somit wichtige Ergebnisse bezüglich der Planung der Serienmessung der 1232 supraleitenden LHC-Dipol-Magnete bis hin zur Implementierung eines im Beschleunigerbetrieb einsetzbaren Instruments zur Vorhersage dynamischer Effekte in den erlaubten Feldkomponenten der Dipolmagnete.

Abstract

Decay and Snapback Studies on the LHC Dipole Model Magnets A Scaling Law

In order to reach the nominal LHC luminosity of $10^{34} \text{ cm}^{-2} \text{ s}^{-1}$ the field quality during particle injection and the initial acceleration must be accurately controlled. High field superconducting magnets are known to have a rich spectrum of non-linear, dynamic field imperfections. Two effects are of particular importance for the beam stability, namely the field drift, "*decay*" at injection as well as the "*snapback*" during the first few seconds of acceleration. From previous experience at Tevatron and HERA, these effects are known to depend on the powering history. Because of this we measured the dependence of dynamic effects on operation cycle variations in seventeen one meter long model magnets as well as in two ten meter long magnets. We statistically analysed the field components. Based on these results we present two models, which focus on the prediction of the sextupole snapback dependence on the operation cycle history. The first model is based on the analogy of the charging and discharging of an RL circuit during the magnet powering sequences. The second model is a multi-layer perceptron (artificial neural network), which we trained to predict snapback by applying the operation cycle description on its input neurons. We discuss the restrictions and capabilities of both prediction techniques. A statistical simulation of different series measurement scenarios was used to estimate the number of magnets that must be measured cold in order to fulfil the beam quality requirements.

For my family, for their support and encouragement:

Maria, Josef, Sonja

Acknowledgments

This work was carried out within the scope of the Austrian Doctoral Student Program in the LHC-MTA group at CERN, Geneva, Switzerland.

I would like to express my special thanks to *Prof. Dr. Hans Kirchmayr*, head of the Institute of Experimental Physics at the Vienna University of Technology, and *Dr. Peter Sievers*, group leader of the LHC-MTA group at CERN. Both provided the administrative basis for my work in the LHC-MTA group. They initiated this project and supported me in the form of many motivating discussions.

I also owe thanks to *Dr. Luca Bottura*. He was my active supervisor at CERN. I highly appreciate his personal engagement, the stimulating discussions with him and his patience during this project.

I would also like to mention the valuable assistance of all the members of the MTA group at CERN. Their excellent cooperation provided the pleasant atmosphere for the successful realization of my thesis:

P. Sievers (Group Leader, Test Facilities for Long Magnets)
L. Walckiers (Deputy Group Leader, Test Facilities in Block 4)
L. Bottura (Field Measurements of Magnets), *A. Siemko* (Power Test of Magnets)

B. Millich (Secretary)

M. Buzio, L. Deniau, P. Pugnat, F. Rival, S. Sanfilippo,
E. Ainardi, Z. Ang, L. Larson, N. Smirnov, F.P. Villar
A. Arn, O. Dunkel, G. D'Angelo, B. Galmant, C. Giloux, P. Legrand, S. Schloss
F. Beauvais, J.M. Cottin, S. Decarroux, G. Deferne, F. Flamand, M. Gateau, C. Henriët,
M. Ky, R. Mompot, G. Rittaud, H.E. Sauce, P. Vignes, S. Vincent, P. Viret

Moreover I feel obliged to a number of helpful colleagues and friends for their friendly communication and cooperation regarding scientific life at CERN, Geneva, Switzerland, and general aspects of life in Preveessin-Moens, Pays du Gex, France:

C. Fabjan, R. Schmidt, K.H. Schindl
J. Billan, S. Ramberger, S. Russenschuck, A.P. Verweij, R. Wolf
P. Bauer, G. & M.C. Borri, E. Gomersbach, K. Heinilä, J. Ostler, P. Smith, R. Wedenig
M. Benedict, J. Lucas, C. Paul, M. Schaller and the farmers, V. Maroussov,
M. & K. Kostro and their youngsters, S. Reimoser & C. Gugler and baby Laura.
S. Lachavanne-Dufour

Finally I would like to thank *Mag. Birgit Bauer* for proof reading and correcting my English language.

Geneva, November 1998

Michael Schneider

Contents

Acknowledgments	5
1 Introduction	8
1.1 CERN	8
1.2 LEP, Standard Model and Higgs boson	9
1.3 LHC	10
1.3.1 Synchrotron Radiation and Luminosity	10
1.3.2 LHC Layout	11
1.3.3 The Accelerator Concept	12
1.3.4 The Superconducting Magnet System	19
1.3.5 The Superconducting Main Dipole	20
1.4 Scope of this Thesis	23
2 Historical Review of Decay and Snapback	25
2.1 Time dependent chromaticity change at Tevatron	25
2.2 Early Considerations of Flux Creep in SSC dipole magnets	32
2.3 Experience with Field Component Decay and first observations of Periodic Pattern at HERA	33
2.4 Contributions from UNK and SSC to the puzzle of slow field component decay	38
2.5 Clarifying the flux creep contribution at HERA	41
2.6 Periodic pattern studies at BNL	42
2.7 Most recent activities in beam parameter control at HERA	44
2.8 Historical studies at LHC	46
2.9 Conclusion of the Historical Review	48
3 Theoretical Models	49
3.1 Decay	49
3.1.1 Flux Creep in the Superconductor	49
3.1.2 Unbalanced currents in the Rutherford type cable	51
3.2 Snapback	56
3.3 Conclusion	56
4 Magnetic Measurements at LHC-MTA	57
4.1 Standard Magnetic Measurement Method	57
4.1.1 Theory of Measurement Technique	57
4.1.2 Complex Formalism for 2D Magnetic Field	58
4.1.3 Magnetic Flux through a Surface	59
4.1.4 Magnetic Flux picked up by a Rotating Coil	61
4.1.5 Voltage induced in a Rotating Pick-up Coil	61
4.1.6 Signal Processing	62
4.2 The Magnet Test Facilities	63
4.2.1 The Long LHC Dipole Model Test Facility (SM18)	63
4.2.2 The Short LHC Dipole Model Test Facility (Block4)	64
4.2.3 Temperature and Current Stability	65
4.3 The LHC dipole model test program	65

4.4	From Raw Data to Results	68
4.4.1	Analysis Tool	68
4.4.2	Feed Down Procedure	69
4.4.3	Integral Harmonics	70
4.4.4	Periodic Pattern Effect	71
4.4.5	Decay Characterization	74
4.4.6	Snapback Calculation	76
5	Experimental Results at LHC-MTA	77
5.1	Standard Operation Cycle Experiments	77
5.1.1	Operation cycle definition	77
5.1.2	Statistical Analysis	78
5.2	Operation Cycle Variation Experiments	83
5.2.1	Injection Variations	84
5.2.2	Pre Cycle Variations	85
5.3	Conclusion of Measurements	87
6	Modeling of Snapback	95
6.1	The Analytical Operation Cycle Model	95
6.2	The Neural Network based Snapback Model	97
6.2.1	Design and Training	97
6.2.2	ANN response to Operation Cycle Variations	98
6.2.3	ANN as an Averaging Tool	99
6.3	Results and Discussion of modeling	100
6.4	Conclusion of snapback modeling	100
7	Application to Series Measurements	106
7.1	Basic Considerations	106
7.2	The Parameterization	107
7.3	The Population	108
7.4	Series Measurement Scenarios	110
7.5	Conclusion	111
8	Conclusion of Decay and Snapback Studies	113
8.1	ANN Training, Testing and Implementation	114
8.2	Cold Measurements	115
8.3	Outlook	115
9	Appendix I: Introduction to Neural Networks	116
9.1	Biological background	117
9.2	The Multi Layer Perceptron	119
	References	122

1. Introduction

1.1. CERN

CERN, the European Laboratory for Particle Physics, is located on the Franco-Swiss border west of Geneva at the foot of the Jura mountains. When it was founded in 1954 it was Europe's first joint venture. Today it is funded by 19 Europe countries and provides particle physics facilities for some 6500 scientists. These researchers represent over 500 universities and institutes in more than 80 countries. Fundamental research is the reason for CERN's being, but the laboratory also plays an important role in finding applications and training tomorrow's scientists and engineers. The fundamental research is focused on exposing nature's most fundamental questions [1]. What is matter? Where does it come from? How does it stick together?

With its largest inter-linked accelerator complex in the world the laboratory provides beams of all kind of different particles. Colliding these particles allows probing the heart of matter and turning back time to the beginning of the universe, the Big Bang. The collision's results are recorded in detectors, which are placed around the beam collision point. Different layers in the detectors measure different properties of the emerging particles, while a magnetic field helps to identify particles of opposite charges and with different momentum.

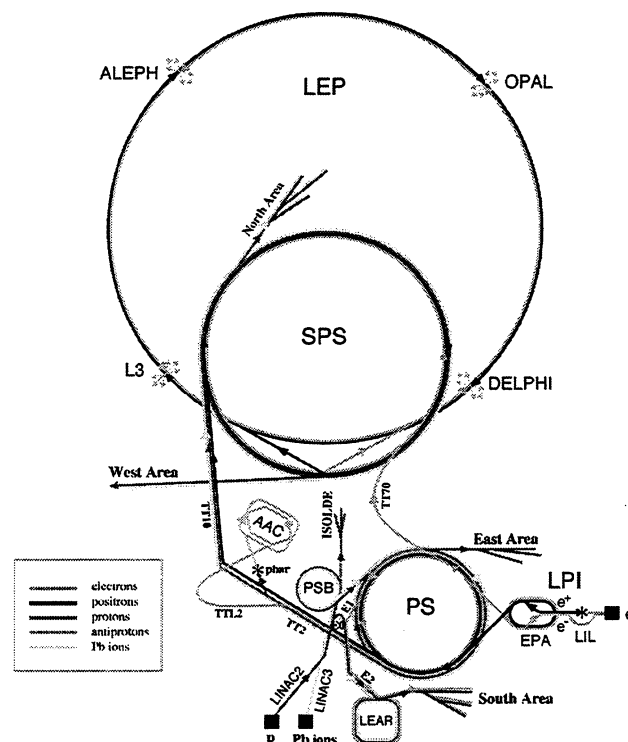


Figure 1.1 Present situation of CERN's accelerator system. LEP: Large Electron Positron collider, SPS: Super Proton Synchrotron, AAC: Antiproton Accumulator Complex, ISOLDE: Isotope Separator OnLine Device, PSB: Proton Synchrotron Booster, PS: Proton Synchrotron, LPI: Lep Pre-Injector, EPA: Electron Positron Accumulator, LIL: Lep Injector Linac, LINAC2: LINear ACcelerator 2, LINAC3: LINear ACcelerator 3, LEAR/LEIR: Low Energy Ion Ring

Accelerators at CERN exist in two types, linear and circular. All particle beams begin their lifetime in linear accelerators. But high energies would require linear accelerators of enormous length. For this reason CERN's big machines are circular accelerators. In this type of accelerator the particle beam goes around and around, gaining energy in each lap.

1.2. LEP, Standard Model and Higgs boson

CERN's largest accelerator is the Large Electron Positron collider, the LEP. It provides acceleration and collision of electron-positron particle beams, which counter rotate in a 27 km long tunnel. On its way through the tunnel, 100 meters below the ground, the beam is focused and bends on a curved track by 3368 magnets. Huge experimental halls, which are located at four points around the accelerator, host the ALEPH, the DELPHI, the L3, and the OPAL detectors [2].

LEP was designed to study one of nature's fundamental forces, the weak force, which fuels the sun, and is responsible for some forms of radioactivity [3, 4]. The weak force is carried by messenger particles called W^+ , W^- and Z . In 1984 Carlo Rubbia and Simon Van der Meer received the physics Nobel Prize for their decisive contributions to the large project which led to the discovery of the field particles W and Z , communicators of the weak interaction. The project was a magnificently executed scheme to collide protons and antiprotons in the existing Super Proton Synchrotron. The experimental results confirmed the unification of weak and electromagnetic forces, the electroweak theory of the Standard Model.

During the first part of LEP's lifetime the Z 's mass was measured to an extraordinary accuracy of 91.1884 ± 0.0022 GeV. The energy gain of particles during acceleration is realized by a combination of copper and superconducting cavities. The second and possibly last lifetime cycle of LEP, the so-called LEP2, was started in 1996. By 1998 an extended number of superconducting cavities pushed the beam energy up to 190 GeV. In this phase the LEP2 produces and studies the W particles. The preliminary measurements of the mass of the W boson is at present the best in the world. It is given by 80.35 ± 0.090 GeV.

The Standard Model can only be a stepping stone to a more complex theory. The Holy Grail of particle physics is the unification of nature's different forces. LEP's data suggested that this only happens if a new theory, supersymmetry (SUSY), is included. This theory introduces a new supersymmetric partner for each particle we already know. LEP's data showed a hint of SUSY in form of an anomaly in the number of times Z 's decay into b -quarks (b -branching ratio R_b). Experiments confirmed that R_b is far from what the standard model predicts, but adding SUSY to the calculations could help to bring theoretical calculation into agreement with the experiments. One expects to see the lightest SUSY particles in LEP2 experiments.

The Standard Model's biggest shortcoming is that it does not explain why particles have mass. Extending the Standard Model by the Higgs mechanism may solve this dilemma. According to this theory, the whole of space is filled with Higgs field, and by interaction with this field, particles acquire their mass. The Higgs field has at least one particle associated with it, the Higgs boson.

Increasing the LEP energy up to 200 GeV in 1999 will be the absolute limit of this machine. But due to the fact that the theory does not put an upper limit on the mass of a particle, the search for new particles and a better understanding of the universe requires much higher energies, which must be provided by stronger accelerators. Thus if LEP does not find these particles they could still be there waiting to be discovered at a more powerful accelerator like CERN's next generation accelerator, the Large Hadron Collider, LHC.

1.3. LHC

1.3.1. Synchrotron Radiation and Luminosity

The reason why LEP's center of mass collision energy is limited to 200 GeV is given by the synchrotron radiation. The emitted power P_s for a charged particle traveling on a circular path is given by Equation 1.1. In this equation e is the elementary charge of an electron, E is the particle energy, ρ is the curvature radius of the particle trajectory, and m_0c^2 is the rest energy of the particle. For LEP operating at 90 GeV we compute 15 MW. This power must be provided by the accelerating cavities, which have intrinsic limitations. Furthermore the power causes chamber heating and radiation hazards.

$$P_s = \frac{e^2 c}{6\pi\epsilon_0 (m_0 c^2)} \frac{E^4}{\rho^2} \propto \frac{1}{(m_0 c^2)^4} \frac{E^4}{\rho^2} \quad (1.1)$$

The required power can be dramatically reduced when accelerating heavier protons instead of electrons in an accelerator with equal energy and radius. This is a consequence of the dependence of P_s on the 4th power of the inverse of the rest mass m_0 . The rest energy of the electron is given with 0.511 MeV, while the rest energy of the proton is 938.19 MeV. This implies that the ratio of synchrotron radiation power loss between electrons and protons is $1.13 \cdot 10^{13}$ [5]. In contrast to electrons the synchrotron radiation becomes appreciable for proton energies above some 100 GeV.

Thus the main limiting factor for a proton accelerator is only the radius of the LEP tunnel, which will be used to host the new accelerator complex. The bending radius of the LEP tunnel determines the required dipole field, which bends the protons on a curved path. This dipole field is proportional to the energy of the protons in the accelerator.

The principal idea of the LHC design is to provide two counter rotating proton or heavy ion beams. But the density of these particle beams is relatively low in comparison to compact matter. Thus the probability of the required central collision for probing into the particles structure is low. Therefore a great effort in providing a sufficient high collision rate must be made. The number of events per second \dot{n} is given by Equation 1.2 where σ_T is the total cross section of the physical process, which is determined by nature, and \mathcal{L} is the luminosity of the accelerating machine.

$$\dot{n} = \sigma_T \mathcal{L} \quad (1.2)$$

The luminosity \mathcal{L} is a measure of the efficiency of the accelerator. It is defined by Equation 1.3 where f_r is the revolution frequency of the number of counter rotating particles N_1 and N_2 per bunch. The coefficient k is the number of bunches in each beam.

The variables σ_1^* and σ_2^* are the horizontal and vertical beam dimensions at the intersection point of the collision. [6]

$$\mathcal{L} = \frac{1}{4\pi} \frac{k f_r N_1 N_2}{\sigma_x^* \sigma_y^*} \quad (1.3)$$

All design efforts in the LHC are directed to provide proton-proton collisions with a center of mass energy up to 14 TeV with an extremely high luminosity of $10^{34} \text{ cm}^{-2} \text{ s}^{-1}$ and heavy ion (Pb-Pb) collisions with a luminosity of up to $10^{27} \text{ cm}^{-2} \text{ s}^{-1}$.

1.3.2. LHC Layout

The schematic layout [7] of the LHC is shown in Figure 1.2. The circumference is divided in eight octants. An octant starts in the center of an arc and goes to the center of the next arc. The arc is the part of the ring occupied by the regular half-cells. The insertion is located between two arcs. It consists of one dispersion suppression, one full straight section and a second dispersion suppression. Each of the insertions performs specified tasks. The two proton experiments using high luminosity are ATLAS and CMS. ALICE is an experiment that deals with heavy ion physics and LHC-B is devoted to B-physics. The two later insertions incorporate also the injection system. The beam cleaning, either Momentum or Betatron is performed in insertion 3 and 7. The beam abort insertion is located in Octant 6 and the radio frequency (RF) devices (cavities) are installed in insertion 4.

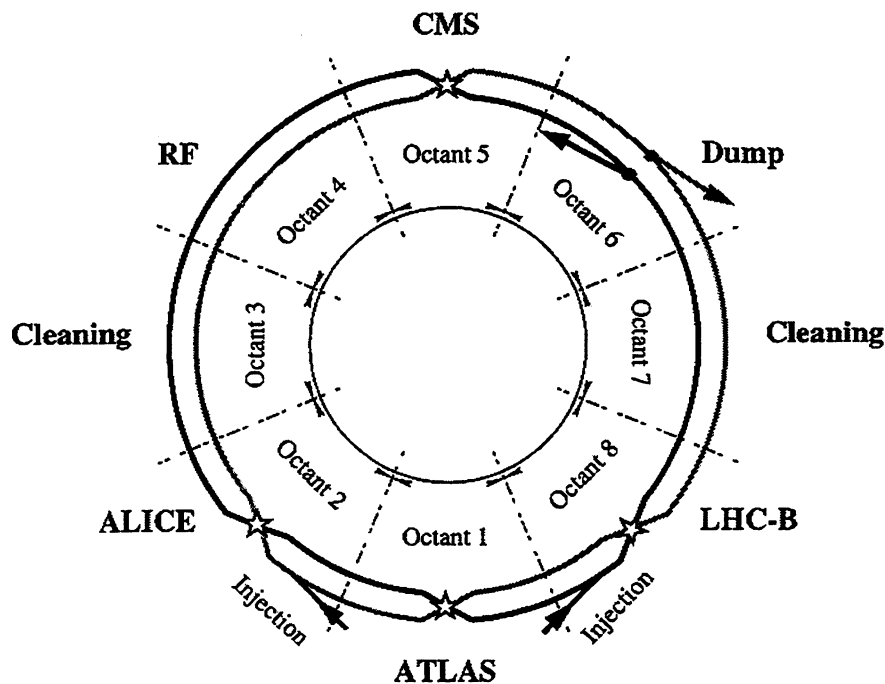


Figure 1.2: Schematic layout of the LHC [8].

The most important LHC performance parameters are collected in Table 1.1. The LHC will come in operation in 2005.

Table 1.1: LHC performance parameters. [10]

Machine circumference	[m]	26658.883
Injection Energy	[GeV]	450
Collision Energy	[TeV]	7
Dipole field	[T]	8.36
Luminosity	[cm ⁻² s ⁻¹]	10 ³⁴
Circulating current per beam	[A]	0.54
Bunch spacing	[ns]	25
Particles per bunch		10 ¹¹
Stored beam energy	[MJ]	334
Beam lifetime	[h]	22
Luminosity lifetime	[h]	10
Total radiated power per beam	[kW]	3.6

1.3.3. The Accelerator Concept

1.3.3.1. Equation of motion

The Lorentz force governs the motion of a charged particle in a beam transport channel or in a circular accelerator. [17]

$$\vec{F} = e(\vec{E} + \vec{v} \times \vec{B}), \quad (1.4)$$

Here \vec{E} and \vec{B} are the electric and magnetic field, \vec{v} is the particle velocity, and e is the electric charge of the particle. We consider now a reference frame where the xy-plane is transverse in respect to the particle motion parallel to the s-axis given by $\vec{v} = (0, 0, v_s)$.

The magnetic field only consists of transverse components $\vec{B} = (B_x, B_y, 0)$. Consequently the particle motion in the horizontal plane is given by the equilibrium of Lorentz $F_L = ev_s B$ and centrifugal force $F_z = mv_s^2/\rho$. From this equilibrium we compute the *beam rigidity*, which connects the bending radius of the particle trajectory and the magnetic field for a particle with given momentum. For a particle on the design orbit, where $x = x' = 0$, $y = y' = 0$ is valid, and design momentum we compute:

$$\frac{1}{\rho_x} = \frac{e}{p_0} B_y(0,0,s) = \frac{e}{p_0} B_{y0} \quad (1.5)$$

$$\frac{1}{\rho_y} = \frac{e}{p_0} B_x(0,0,s) = -\frac{e}{p_0} B_{x0} \quad (1.6)$$

The term $|B\rho|$ is the *beam rigidity*, which can be expressed in more practical units:

$$B\rho \text{ (Tesla} \cdot \text{Meter)} = 3.3356 p \text{ (GeV / c)} = 3.3356 \beta E \text{ (GeV)} \quad (1.7)$$

Here E is the total energy, p is particle momentum, and $\beta = v/c$.

In the case of an ensemble of particles characterizing a beam we assume that the transversal beam dimensions are small in comparison to the bending radius of the particle trajectory. Thus the field components may be expanded in series to the first order:

$$B_x(x, y, s) = B_{x0} + \frac{\partial B_x}{\partial x} x + \frac{\partial B_x}{\partial y} y \quad (1.8)$$

$$B_y(x, y, s) = B_{y0} + \frac{\partial B_y}{\partial x} x + \frac{\partial B_y}{\partial y} y \quad (1.9)$$

In this notation the zero order term gives the dipole field, while the linear terms are the quadrupole contribution to the magnetic field. Here we introduce the normalized gradient K_0 and the skew normalized gradient \underline{K}_0 defined as:

$$K_0 = \frac{e}{p_0} \left(\frac{\partial B_y}{\partial x} \right)_{x=y=0} \quad \text{and} \quad (1.10)$$

$$\underline{K}_0 = \frac{e}{p} \left(\frac{\partial B_x}{\partial x} \right)_{x=y=0} \quad (1.11)$$

In the case where the bending magnets of a circular accelerator deflect only in the horizontal plane, the linear unperturbed equations of motion for a particle having the design momentum p_0 are

$$x'' + \left(K_0 + \frac{1}{\rho_x^2} \right) x = 0 \quad \text{and} \quad (1.12)$$

$$y'' - K_0 y = 0 \quad (1.13)$$

where $K_0(s)$ and $\rho_x(s)$ are periodic functions of the s -coordinate due to orbit being a closed curvature. The period L may be the accelerator circumference C or the length of a "cell" repeated N times around the circumference: $C = LN$. Both expressions of the equations of for both planes in Equations 1.12 can be cast in the form

$$u'' + K(s)u = 0 \quad (1.14)$$

with

$$K(s + L) = K(s) \quad (1.15)$$

where u stands for x or y and $K(s) = K_0(s) + \rho_x^{-2}(s)$ or $K(s) = -K_0$. Equation 1.14 is called Hill's equation, which is the fundamental equation of motion when treating linear beam optics. This formalism allows us to establish transfer matrixes for each element in the accelerator. Thus particle can be transferred from one point to another point in the accelerator by simple matrix multiplication.

1.3.3.2. Beam Optics

The main magnets required in a modern accelerator are dipole magnets, which bend the beam, and quadrupole magnets, which focus and defocus the beam.

A positive charged particle on the design orbit in the horizontal plane follows a bending trajectory in the presence of a vertical dipole field. This is shown in Figure 1.3.

The quadrupole magnets provide focusing forces through their normalized gradient, given by Equation 1.10. A quadrupole that focuses (F-type) in one plane defocuses (D-type) in the other plane. The horizontally defocusing, D-type quadrupole, is obtained by permuting the N- and S-pole of an F-type quadrupole. The magnet poles, the field lines and the forces on a positive charged particle inside a horizontally focusing quadrupole are shown in Figure 1.4. The positive particle approaches the reader.

A machine of this type makes use of the so-called *alternate gradient* [29] concept. This concept provides focusing and keeps a small beam.

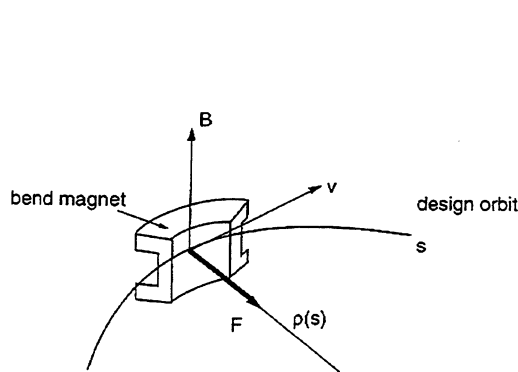


Figure 1.3: Force on a positive charged particle due to a dipole field. [17]

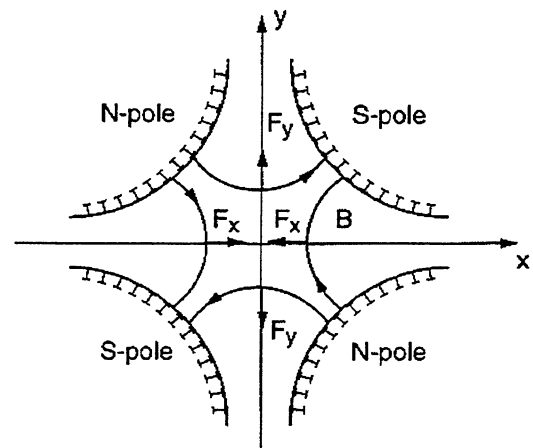


Figure 1.4: Focusing and defocusing effect on off-design orbit particles due to a quadrupole magnet. The particle carries positive charge. [17]

Figure 1.5 shows a schematic diagram of the major components of the accelerator. We see schematically a particle source, which pre-accelerates particles in order to inject them into the main accelerator machine. Bending focusing and accelerating elements compose the main accelerator complex.

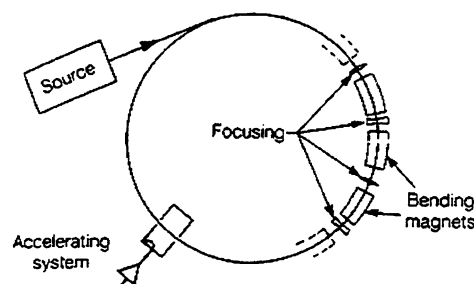


Figure 1.5: Schematic diagram of the major components of the accelerator, containing injection source, bending magnets, focusing elements, and finally accretion systems. [18]

A beam of particles is established in the LHC accelerator by injecting a sequence of particle bunches. These particle bunches are generated and accelerated in the pre-acceleration units of the LHC accelerator complex. When a bunch reaches the injection energy a so-called transfer line passes it from the SPS towards the LHC. The bunched structure is required because of the accelerating elements in the LHC. These elements are radio frequency devices, which accelerate particle bunches by electromagnetic waves. In order to provide a beam with the required luminosity at the intersection point of the collision experiments, the particles must be accumulated during the injection period and subsequently accelerated without any particle loss.

1.3.3.3. Beam Dynamics

The challenging task of providing stable particle trajectories starts already during the injection period. Bunches will be injected with a spread in energy and initial orbit around the design orbit. This mis-match may lead to beam perturbation, chaotic particle trajectories and consequently to particle loss.

The main effect on particles with the nominal momentum but off design orbit are additional forces due to the quadrupole magnets. These focusing and defocusing elements in the beam optics establish an oscillatory movement, called *betatron oscillations*, of the particle beam. Deduced from the betatron oscillation we can define the *machine tune*, Q , as the number of betatron oscillations per revolution. Due to the risk of resonance effects this number must be non-integer. The effect of focusing and defocusing elements in the beam optics is shown in Figure 1.6. The bold line shows the trajectory of a single particle while the dashed curve represents the envelope of the beam. This envelope can be expressed in terms of a *betatron function*.

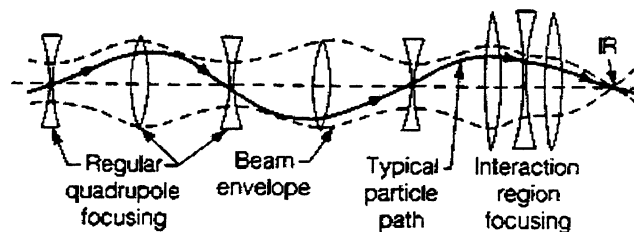


Figure 1.6: Particle trajectory and betatron function in presence of focusing elements. [18]

Off-momentum particles on or off the nominal orbit do not circulate with stable tune values because of changed focal length of the focusing and defocusing elements. This effect is defined in accelerator storage ring physics by the *chromaticity* [30], a parameter that describes the different focusing strength in the quadrupoles for particles with different momentum. A close similarity of this effect is given by the chromatic aberration in geometrical light optics, where rays of different wavelength find a different refraction index in a lens and therefore experience a different focal length. As a consequence we will have different betatron oscillation frequencies for particles with different momentum.

We define the relative chromaticity as the variation of betatron tune Q with the relative momentum deviation $\delta = \Delta p / p_0$:

$$\xi = \frac{\Delta Q}{Q} / \frac{\Delta p}{p_0} \quad (1.16)$$

In circular accelerators the chromaticity has a dramatically important influence on beam dynamics for two main reasons. First a momentum spread is always present in a particle beam; therefore the chromaticity produces a tune spread ΔQ . This implicates that a beam with a given momentum spread must be provided with an adequate machine chromaticity in order to accommodate the beam between the resonance lines of the tune diagram [31]. Second in case of bunched beams the chromaticity induces head-tail instabilities. The wake field produced by the leading part of the bunch (head) excites an oscillation of the trailing part (tail) of the same bunch. In half a synchrotron period the head and the tail of the bunch interchange their positions. This oscillation can be anti-damped and may cause beam loss. The growth rate of this instability is much faster for negative than for positive chromaticity and vanishes for zero chromaticity. Therefore most of the storage rings operate at zero or slightly positive ξ . The natural chromaticity of a storage-ring is determined only by the linear elements of the lattice, i.e. dipole and quadrupole. But the natural chromaticity of a strong-focusing storage ring is always negative, thus special correction elements have to be introduced in the lattice. In large rings with strong focusing lattice the main contribution to the chromaticity is due to the quadrupoles. For small rings the dipole contribution has to be taken into account.

1.3.3.4. Beam Quality

The nominal performance of the LHC is defined by the luminosity. In order to provide the required high luminosity at collision (7 TeV), several beam parameters have to be carefully monitored respectively adjusted during injection (450 GeV) and acceleration of the beam. These beam parameters are central momentum, closed orbit, betatron tunes, chromaticity, betatron coupling, beta-beating, dispersion, dynamic aperture.

The nominal value [24] of the betatron tune for the LHC is 63 units and needs to be controlled to a level of 0.003 for ultimate performance. Orbit excursions should be limited to less than 0.5 mm (rms value) of the closed orbit. The chromaticity, the change of tune with energy, should be limited to some units as compared to a natural value of approximately 600 units. These requirements translate into strict tolerances on the quality of the bending (dipoles) and focussing (quadrupole) magnetic field.

The dipole field has to be adjusted to the order of -7 , which appears to be a big challenge since the typical sextupole dynamic during injection respectively the initial acceleration is of the order of -4 . Furthermore a change of one unit of sextupole component of the dipole field translates into approximately 150 units of chromaticity.

Dynamic aperture [26], which is the largest stable transverse amplitude in a connected domain for a sample of "typical" particles circulating in a simplified model of the accelerator, has been the subject of intensive simulations. Beam-beam effects, tune spread and excitation of resonance give its major limitations. It is confirmed [25] that minimizing tune spread with multipole correctors increases the dynamic aperture. In contrast to older machines these corrections at LHC have to be applied to the sextupole as

well as to the decapole component. The target dynamic aperture of the LHC is 12σ (RMS beam size at the maximum betatron amplitude in the arcs), which is adequate for safe operation. But dynamic aperture is also influenced by the errors along the machine azimuth. In such cases sorting strategies can be used to provide the mutual compensation of the residual error [27].

The tolerances of the beam parameters are determined by some specialties [23] of the LHC machine design. Firstly the LHC is a large machine and the effects of errors tend to be amplified and are often inter-linked. Several manufacturers will build the same type of magnet. The machine is electrically split into eight sections requiring tracking between the power converters of magnet families. The safety margins are small because it is expensive to increase them. The energy stored in the beam is very large. A small loss (10^{-4} at injection) might lead to a quench of a magnet with several hours to recover. And finally the LHC has to fit into an existing infrastructure, which means there is less flexibility.

All of these particularities of the LHC machine implicate several challenging tasks for the design, construction, quality control and finally the operation of the accelerator.

1.3.3.5. Field Errors

An ideal dipole and quadrupole field can be generated by the current distributions shown in Figure 1.7. An ideal dipole field is given by a $\cos(\phi)$ current distribution while an ideal quadrupole field is obtained with a current distribution proportional to $\cos(2\phi)$ [19]. The parameter ϕ is the azimuth angle. The dipole current distribution provides a constant B_y field component in the median plane of the magnet. The field components B_x and B_y of the quadrupole show a linear dependence of the position in the magnet's aperture. This provides focusing or defocusing, dependent on the plane we observe, for particles that are circulating in an off-design orbit.

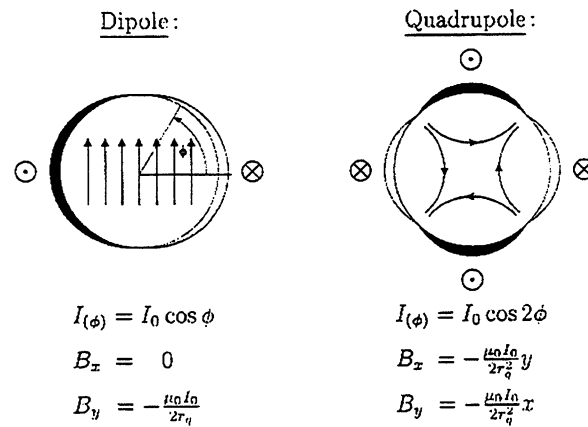


Figure 1.7: Generation of a pure dipole and quadrupole field by use of homogenous current shells. [19]

The technical realization of the dipole and quadrupole current distributions is performed by a discretization of the homogenous current shells. This approximation introduces a

number of field imperfections, which in order to characterize a certain field quality, must be minimized and corrected.

As customary for accelerator magnets, the magnetic field in the LHC dipoles is expanded in a two-dimensional Fourier series:

$$\mathbf{B}(x, y) = B_y + iB_x = 10^{-4} B_1 \sum_{n=1}^{\infty} (b_n + ia_n) \left(\frac{x + iy}{R_{ref}} \right)^{n-1} \quad (1.17)$$

where b_n and a_n are the *normal* and *skew* multipole coefficients, normalized to the main field component B_1 . The reference radius R_{ref} is initially set to 10 mm for the LHC. During the preparation of this thesis the reference radius was changed to 17 mm. In order to be consistent through the thesis we decided to proceed our data treatment with the original value. Note finally the scaling factor 10^{-4} in front of the multipole coefficients. The normal and skew multipole coefficients as defined above are expressed in so-called "units". Regarding the summation index we have to mention that the LHC project makes use of the European notation starting with index number 1 for the dipole field component. According to this notation the sextupole or decapole component are indexed with number 3 respectively 5. In contrast to this notation we will often find the index number 2 in charts showing sextupole behavior in our historical review. This numbering is in consistency with the so-called American notation.

Field errors in superconducting dipoles have several origins. We show a typical example of the various contributions to the magnetic field in Figure 1.8. We report the normal sextupole b_3 behavior along the loadline of a LHC dipole in a typical accelerator (like) operation cycle.

As for normal conducting magnets we can define field errors of *geometric* origin that result from the deviation of the placement of conductors from the ideal current distribution giving the desired magnetic field [9]. Similarly, at high field (approximately 6 T in the LHC dipoles) significant deviation from linearity and field errors is caused by the *saturation* of the iron yoke. The geometric and saturation field contributions are reproducible, can be predicted accurately and may be largely inferred from warm measurements.

Additional effects peculiar to superconducting magnets are caused by the known DC and AC diamagnetic property of a superconducting cable. The LHC magnets are wound using flat (Rutherford) cables, built up from 20 to 40 superconducting, multifilamentary, twisted NbTi strands. Each strand contains thousands of fine superconducting NbTi-filaments. Each filament in turn behaves as a diamagnetic material, whose contribution to the magnetic field quality can be appreciable at the low field levels required for the LHC injection. This contribution is often referred to as *persistent currents*, in relation to the long lasting (ideally infinite) duration of the shielding currents responsible for the diamagnetic behavior of the filaments [21]. Similarly the *eddy currents* arising in a Rutherford cable during energy ramps (and associated field changes) act collectively resulting in another diamagnetic contribution to the field [22]. Persistent and eddy current contributions are reproducible, but they require that the magnet is measured in superconducting state.

Finally, the LHC will have to deal with a new class of unexpected effects, which are as well associated with the properties of the superconducting cable. The effect is a *decay* of

the magnetic field and field errors during long periods (>100 s) of constant current excitation, followed by a rapid recovery of (approximately) initial value before the drift as soon as the current is ramped (here called *snapback*). At present these two effects, as will be discussed later on, are not fully understood and cannot be predicted accurately. Their order of magnitude is comparable and larger than the set tolerances to achieve the machine performance. The sextupole decay and snapback in a typical accelerator cycle is, for example, of the order of 0.5 units as shown in Figure 1.8.

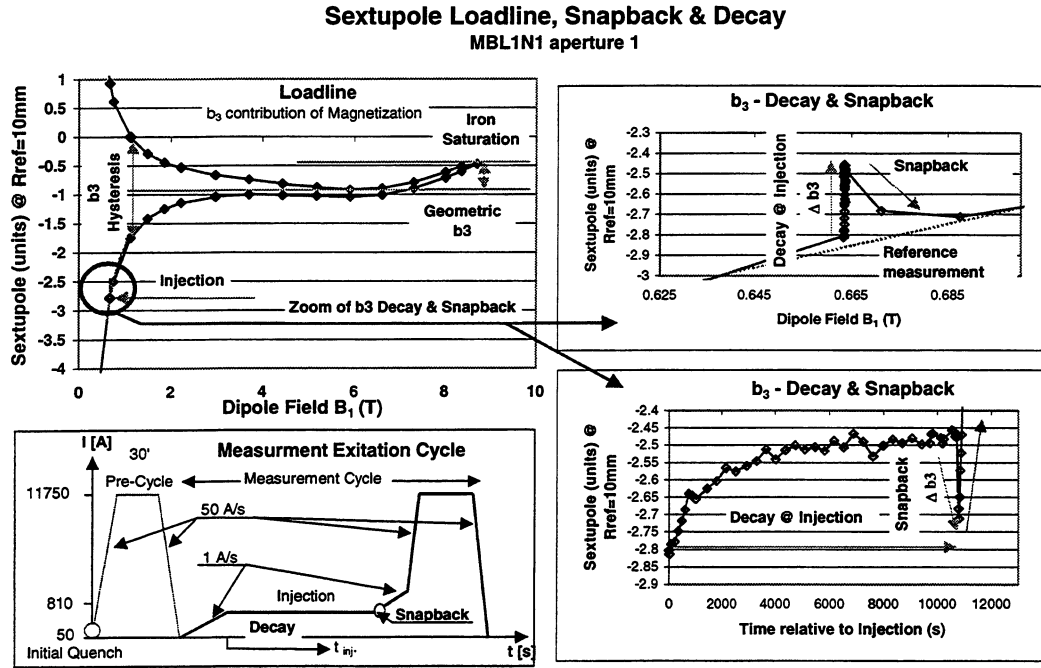


Figure 1.8: Sextupole *loadline*, *snapback* and *decay* for a 10 meter long LHC model magnet. The bottom left picture shows a typical test cycle. The top left picture shows the sextupole magnetization behavior along a full excitation cycle. The constant excitation current at injection leads to the sextupole field component decay, which is shown in the two right hand side pictures. We can see also the fast bounce back (*snapback*) when the acceleration ramp starts.

1.3.4. The Superconducting Magnet System

In the LHC there will be 1232 main bending dipoles, 386 main quadrupoles, to which small correctors have to be added. In total there will be about 8400 superconducting units of different size and importance [9]. The LHC magnets are thus one of the most massive application of superconductivity. The conductor quantity will be about 1200 t, of which approximately 400 t will be NbTi alloy. The total mass to be kept at 1.9 K temperature will be close to 30000 t distributed on a 27 km circumference. The technical choice for NbTi superconducting technology was made in the scope of reaching the required 8.4 T reliably and economically. This field corresponds to the nominal beam energy and the curvature of the LEP tunnel.

1.3.5. The Superconducting Main Dipole

The superconducting main dipole consists of the most challenging feature in magnet design. The design is based on a cost saving two in one design.

1.3.5.1. The Dipole Cable

The coil of the LHC dipole consist of two layers of windings, 15.4 mm wide, with a different superconducting Rutherford type cable for each layer [13]. Figure 1.9 shows a typical Rutherford type cable structure.

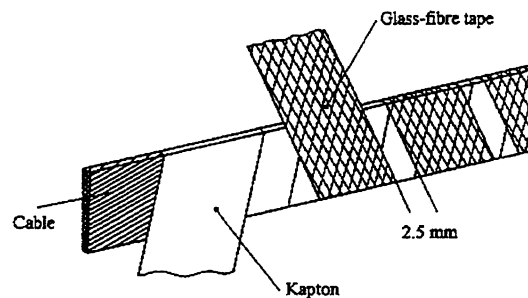


Figure 1.9: Rutherford type cable enclosed by its insulation. The insulation of the cable consists of a half-overlapping layer of kapton with a 25 μm thick glass-fibre tape, pre-impregnated with epoxy resin with spaces of 2.5 mm between successive turns. [76]

The inner cable of the dipole is made of 28 strands 1.065 mm in diameter, with a Cu/superconductor ratio of 1.6. The outer cable is made of 36 strands, each 0.825 mm in diameter. Each strand is built up by a structure of thousands of NbTi-superconducting filaments embedded into a copper matrix. The strands are annealed before coating and cabling. The cable is manufactured by passing the strands through a turk's head, where they are strongly deformed. This process finally leads to the flat Rutherford type structure. The total number of LHC twin aperture dipoles will require the fabrication of around 6600 km of superconducting cable. The cable specifications for inner and outer layer are shown in Table 1.2.

Due to the particularities of the geometric structure of the cable the research was focused on the control and understanding of the importance of the value and distribution of the inter-strand resistance. Parallel strands following the two faces of the cable are touch-crossing strands from the opposite face of the cable. These crossing points are electrically characterized by a crossing resistance (R_c). A second resistance appears in form of the contact between adjacent strands (R_a) in each face of the cable. This network of resistors forms loops in the cable structure. Consequently field sweeps will induce coupling currents between the strands, resulting in dynamic field distortions of the magnet field, and in energy losses.

Crossing and adjacent resistance have been the subject of intensive studies. A target of R_c in the range of 10 to 20 $\mu\Omega$ was specified as a balance between AC loss heating and unbalanced current distribution currents [15, 16]. The inter-strand resistance is difficult to control as it depends not only on the coating material, but also on storage conditions, temperatures and pressures in the curing cycle and pre stress in the coil.

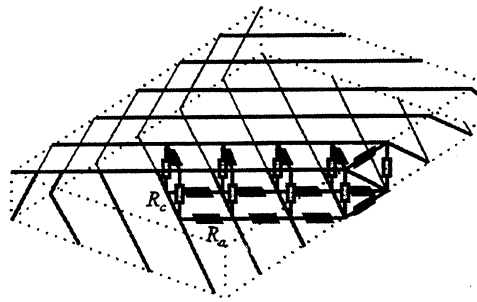


Figure 1.10: Transparent cross section of the Rutherford type cable showing crossing and adjacent resistance in the network model. [76]

Table 1.2: LHC main dipole cable parameter. [66]

		outer layer	inner layer	
Cable Height	mm	15.4	15.4	insulated
Cable inner width	mm	1.6197	1.9728	insulated
Cable outer width	mm	1.8604	2.3073	insulated
Cable height	mm	15.10	15.10	bare
Cable inner width	mm	1.362	1.736	bare
Cable outer width	mm	1.598	2.064	bare
Radial insulation thickness	mm	0.150	0.150	
Azimuthal ins. thickness	mm	0.130	0.120	
Number of strands		36	28	
Diameter of strands	mm	0.825	1.065	
CU/SC Ratio		1.90	1.60	
T_{ref}	K	1.90	1.90	
J_c	A/mm ²	1953.0	1.433.3	9.0 T, T_{ref}
dJ_c/dB	A/mm ² T	550.03	500.34	

1.3.5.2. The Dipole Structure

Figure 1.13 shows a longitudinal section through the superconducting dipole for the LHC. The two beam channels are incorporated into a single iron yoke and a cryostat. The coils are formed of two winding layers, each layer divided in blocks made of keystone cables. The cables are of the same width but of different thickness, resulting in the desired gradient of current density for optimum use of the superconducting cable. The number of blocks, the exact positioning, and the number of turns in a block have been the subject of intensive comparative studies. Historically the dipole cross section (Pink Book [11], White Book [12]) was represented by the five-block design. This design has been subject to several changes [10]. Finally (October 1997) the last design proposal is based on a six-block geometry. The best coil as far as tunability, margin and sensitivity to tolerances are concerned, is a design named V6-1 [66]. The differences in the quarter cross section design are shown in Figure 1.11 and Figure 1.12.

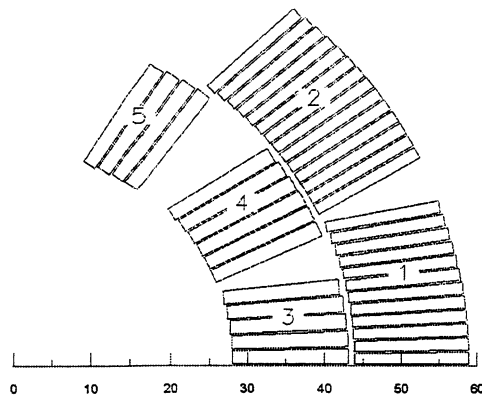


Figure 1.11 Five-block design of the quarter cross section of the LHC main bending dipole magnets. [66]

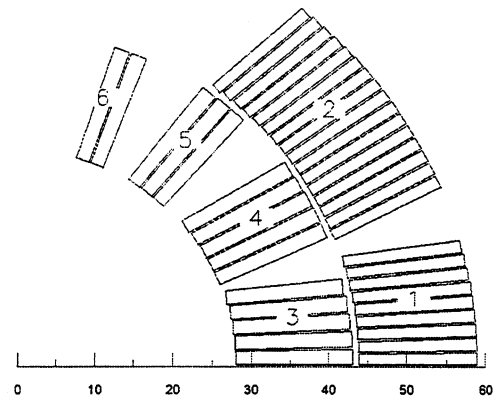


Figure 1.12 Six-block design of the quarter cross section of the LHC main bending dipole magnets. [66]

The coil is produced in the following way. The cables are insulated by two half overlapping wraps of polyimide tape and a third wrap of polyimide tape with an adhesive. After winding, the adhesive is cured by heating each coil layer in a curing mould. The standard heat treatment for 0.5 hours at 190 °C under pressure is used in the fabrication of the coil to glue the polyimide insulation onto the cables. The cable insulation [14] is of particular importance for optimized superfluid helium penetration in order to provide additional enthalpy and to profit from its very high thermal conductivity. Now the final structure and size of the coil is achieved. Inserting perforated glass-epoxy spacers between the inner and outer coil shells provides channels for the circulation of the cooling helium. The insulation to ground is composed of superposed polyimide film layers and includes the quench protection heaters.

The coils have to be surrounded by a force containment structure in order to prevent tensile stress from arising in the coils under the action of the electromagnetic force. The force containment structure consists of the collars, the iron yoke, and the shrinking cylinder.

The cold mass kept at 1.9 K is delimited on the outside by the shrinking cylinder and on the beam side by the inner wall of the beam pipes. The cold mass is installed inside a cryostat. Its main components are a radiation shield at 5 K, a thermal shield at 70 K, and the outer cylinder wall of the vacuum vessel. Three feet support the cold mass. The center foot is fixed, while the other two can move on rollers to accommodate thermal contraction or expansion.

Attached to the ends of each dipole magnet are one small sextupole and one small decapole corrector to compensate the corresponding multipole errors of the main dipole. The main and auxiliary bus bars, which accommodate the cables to power the magnets of the arcs, are located in grooves in the iron yokes [8, 9].

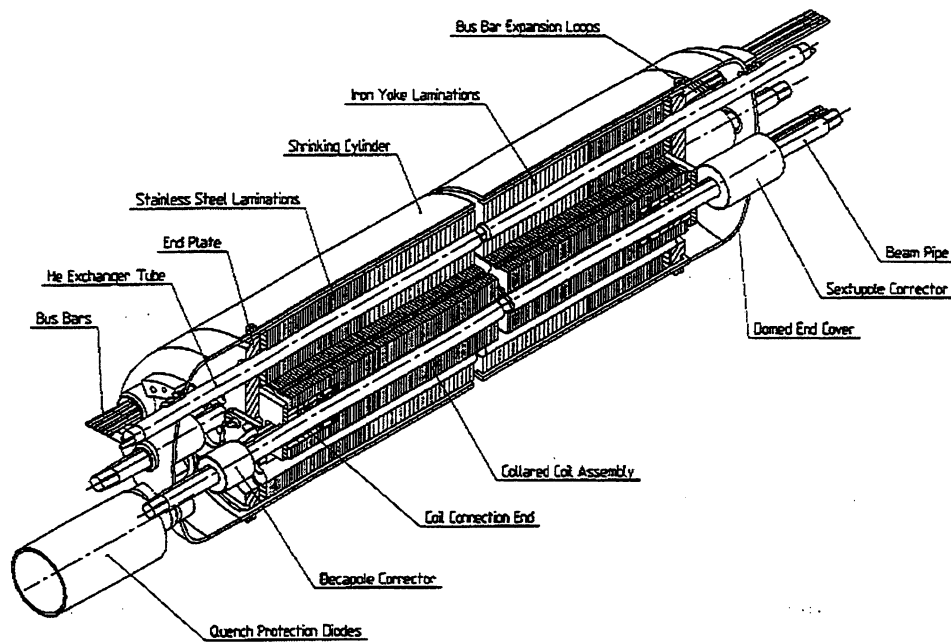


Figure 1.13: LHC main dipole cold mass assembly [10].

1.4. Scope of this Thesis

This thesis covers historical aspects, theoretical modeling and experimental measurements of field decay and snapback. We provide the statistical average and standard deviation of the amplitude of the decay respectively snapback as well as the time constants of the field component decay. This knowledge finally allows the establishment of a scaling law of decay respectively snapback in one-meter long LHC dipole model magnets that appear to be applicable for LHC operation. A statistical simulation of a series measurement scenario provides information concerning the number of magnets which must be measured cold in order to reach a certain accuracy of the sextupole snapback mean, which must be known for the LHC chromaticity control.

The contents of this thesis are structured in the following order:

Chapter two covers a historical review of experimental results of decay, snapback and field periodicity. We show results of experiments at SSC, HERA, UNK, BNL and historical LHC activities and thereby gain phenomenological knowledge.

In chapter three the most recent activities concerning the theoretical understanding of the observed effects are presented. The chapter provides the theoretical background in the scope of flux creep in strong pinning type-II superconductors, the existence of boundary induced coupling currents or supercurrents, and finally a theory about magnetization decay due to the current redistribution between the strands of the Rutherford type cable.

Chapter four introduces the experimental equipment and measurement technique, which was used in our magnetic measurement laboratories. We explain our standard data

treatment of the magnetic field studies, which were performed on a number of one-meter and ten-meter long LHC dipole model magnets.

In chapter five experimental results of our magnetic measurement programs are presented. The results are presented in two main sections. One section covers standard measurements from which we derive statistical values concerning the characterization of the field component decay and snapback. The second section is dedicated to snapback behavior studies due to variations in the power conditions of the magnets.

In chapter six we present two approaches towards a scaling law of operation cycle variation influence on the snapback amplitude. Firstly we show modeling based on the idea of charging and discharging a simple RL-circuit. The second approach towards the snapback prediction is given by use of artificial neural networks. We discuss the applicability and accuracy of both methods.

An application to series measurements in form of a statistical simulation in chapter seven provides us with the minimum required number of cold measured magnets in order to fulfil accuracy requirements of the chromaticity.

The conclusion, chapter eight, provides an overview of experience concerning the measurement of dynamic effects at LHC-MTA and possible scaling or prediction procedures. It covers basic considerations concerning the application of an artificial neural network in a correction system for dynamic effect of the LHC. We announce the application of a hall plate based measurement device for future sextupole dynamic studies.

2. Historical Review of Decay and Snapback

Firstly this chapter gives a historical review of measurements and research covering slow field component decay as well as snapback. The starting point is the first observation of time dependent chromaticity change at the Tevatron. An overview of experiments at SSC, HERA, UNK, BNL, and LHC is then provided. The Tevatron and HERA operation experience emphasizes the importance of acquiring basic knowledge concerning field dynamics respectively field dynamics correction.

2.1. Time dependent chromaticity change at Tevatron

The Tevatron was the first storage collider ever built by use of superconducting magnet technology. The collider is designed to operate either in *fixed target mode* or in *collider beam mode* [28].

In fixed target mode particles pass through a chain of four pre-accelerators before they reach the final stage, the Tevatron. The first unit of the acceleration chain is the Cockcroft-Walton. Electrons are added to hydrogen atoms and the resulting negative charged ions are attracted to a positive voltage and accelerated to 750 keV. The following linear accelerator (LINAC) accelerates the ions up to 400 MeV. Before entering the Booster, the third stage of acceleration, the ions pass a carbon foil, which removes the electrons and leaves only the protons. The Booster is a rapid cycling synchrotron, which raises the energy of the protons to 8 GeV. The Booster normally cycles twelve times in rapid succession, loading twelve pulses, so called bunches of protons into the Main Ring. The Main Ring is a synchrotron that is built up with 1000 conventional, copper-coiled magnets, and installed in a tunnel of 6,3 km circumference. The Main Ring is the injection unite for the final acceleration stage, the Tevatron, which allows proton acceleration from 150 GeV up to 900 GeV. This final stage contains the 1000 superconducting magnets, which produce a much larger magnetic field at a lower operation cost than conventional magnets. Furthermore the increased magnetic field allows the installation below the Main Ring in the same tunnel. Thus the cost-intensive construction of another tunnel can be avoided.

When operating the Tevatron in collider beam mode, the beam of protons is collided with a beam of antiprotons. To produce antiprotons, protons are first accelerated to 120 GeV in the Main Ring, extracted and focused on a target area. The collision produces a wide range of secondary particles including many antiprotons. They are selected and stored in the Antiproton Storage Ring. When a sufficient number has been produced, the antiprotons are re-injected into the Main Ring and passed down into the Tevatron where they are simultaneously accelerated to the collision energy of 900 GeV with a counter-rotating beam of protons. This is the working principle of the Tevatron.

But during initial coasting beam tests big changes in the beam behavior in the course of several hours were observed. The reason for this effect was found to be a *time variation* of the *chromaticity* [30].

In the Tevatron the chromaticity, which should be limited to 2 units in order to avoid beam degradation, excited a change of 70 units during several hours of observation [33]. Furthermore large variations in initial tunes and chromaticity were observed. These variations depended on the details of the recent operation history of the machine. This fact is shown in Figure 2.1. We see fractional initial tunes as function of time and

momentum offset. The chromaticity is the slope of the lines, which changes rapidly at first and then more slowly.

Data taken from beam measurements showed that the behavior of chromaticity is consistent with a time varying sextupole moment of the machine. But beam measurements are only sensible to the average over all the dipoles. This allows the conclusion that the sextupole moment of all 774 superconducting dipoles changes in time. Thus the chromaticity of the machine is given by (neglecting corrector setting):

$$\xi_{x,y}(t) = -22.5 + \langle \eta \beta_{x,y} b_3(t) \rangle \quad (2.1)$$

with -22.5 the natural chromaticity, η the dispersion function, β the betatron amplitude, and b_3 the sextupole coefficient of the magnets in the ring.

The temporal drift in the sextupole component of the dipoles was verified in measurements on a small sample of dipole test coils in the magnet test facility. One of these measurements is shown in Figure 2.3. In consistency with the change of chromaticity the decay of the sextupole component showed two time constants.

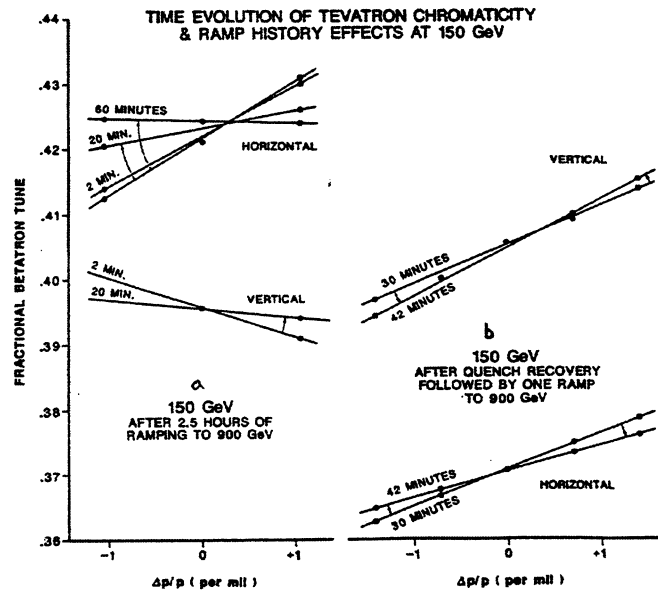


Figure 2.1: Temporal change of chromaticity versus momentum offset while Tevatron energy is fixed to 150 GeV (injection energy). [33]

Basic considerations concerning the source of the observed sextupole decay during constant magnet excitation focused mainly on temperature variations and on eddy current effects. But the well-monitored temperature showed only marginal variations and could therefore be excluded as interfering factor. Also the eddy current could not explain the observed effects either because of the existence of two time constants.

While lacking a theoretical explanation of the effects it was undoubtedly a success to put the Tevatron into operation. Since the sextupole decay was understood to be the source of chromaticity change during particle injection, the solution of chromaticity control was found by reading the curve shown in Figure 2.2 and setting the sextupole corrector power converter. On the other hand it was understood that cycling the machine six times before

each 150 GeV store would avoid different initial tunes [34]. But the performance during these early days of commissioning was not impressive. The machine preparation usually took more than one hour of resting at 150 GeV (see Figure 2.2) before the fastest part of the sextupole decay died away and proton antiproton filling procedure started. Besides one of the biggest outstanding problems occurred in the initial sequence of transmission from 150 GeV to 900 GeV. A chromaticity variation at the beginning of the ramp led to transverse *emittance* [32] increase.

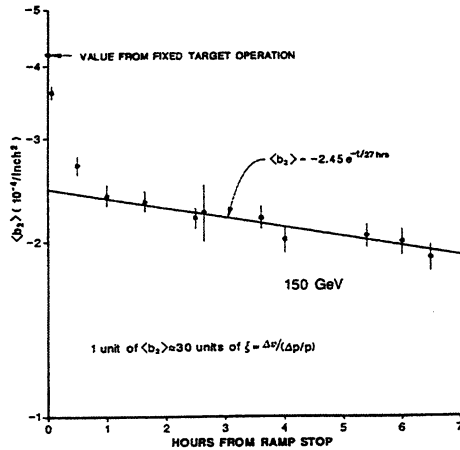


Figure 2.2: Preparation of injection at Tevatron. Injection started after one hour when fit for b_3 -decay became sufficient. [33]

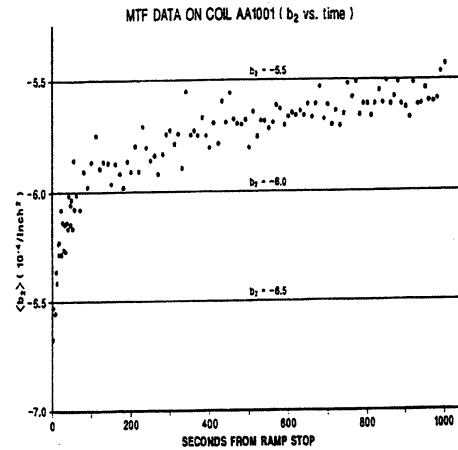


Figure 2.3: Magnet test facility measurement result showing the typical two time constants. [33]

Two years after Finley et al. presented the first paper about sextupole decay induced chromaticity variations in the Tevatron, Johnson and Herrup showed first results of chromaticity correction algorithms, which reduced variations in chromaticity by one order of magnitude in comparison to the uncorrected operation. In order to correct the sextupole Equation 2.1, the chromaticity of the machine, was extended by a time dependent sextupole term $S(t)_{x,y}$. The sextupole as function of time was fitted by a linear dependence on $\ln(t)$ [34]. The function consists of two parameters and is shown in Equation 2.2.

$$b_3(t) = A + B \ln(t) \quad (2.2)$$

A comparison of data of sextupole decay from early measurements in March 87 with most recent ones from January '89 was provided by Johnson and Herrup. They concluded that the significant difference in these two results required the installation of a permanent chromaticity measurement at 150 GeV. Figure 2.5 shows the dipole's b_3 -decay rates deduced from the routine shot set up over a five-week period. We see two lines according to the choice of fit parameters. The dashed and the solid curve are the fits to the data taken in March '87 and January '89 respectively.

The remaining spread in chromaticity was considered to be due to the prior powering history of the dipoles. It is stated that a longer duration on flat top current resulted in a lower initial sextupole and the subsequent decay deviated from being linear to $\ln(t)$. The effect of powering history on the b_3 -decay rate is clearly shown in Figure 2.5. The b_3 -decay rate at injection for cycles containing a flat top duration longer than 3 hours differs

significantly from cycles in which the magnet has been operated on flat top for less than 3 hours. Another chart of interest (Figure 2.4) can be found in the publication of Johnson and Herrup. It is the first ever documentation of a sextupole hysteresis curve including decay and snapback at injection (marked with an arrow). [34]

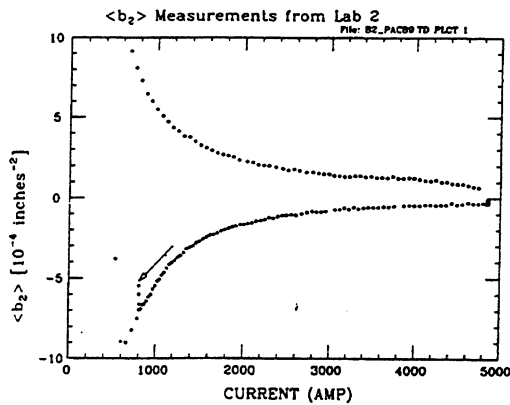


Figure 2.4: First ever published sextupole hysteresis including decay and snapback at injection (marked with an arrow). [34]

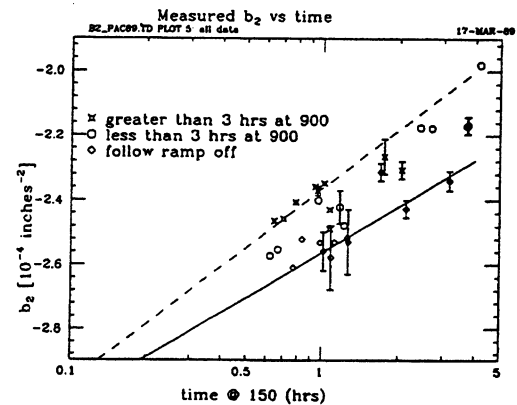


Figure 2.5: Spread in sextupole decay rate in measurements of March '87 and January '89. [34]

The next step towards optimum performance of the Tevatron was a detailed examination of the above mentioned chromaticity variation during at the start of the ramp [35]. The chromaticity measurement was performed by varying the RF frequency and recording the corresponding change in tune of the beam. In contrast to the well-controlled chromaticity during the injection, tune lines disappeared at the start of the ramp and reappeared several seconds later. Thus, for several seconds, the Tevatron chromaticity was over 30 units away from the goal of $2 < \xi < 4$. Consequently the normalized transverse emittance increased and there was some loss of bunched beam. Laboratory measurements on a single Tevatron-style dipole magnet showed that a fast sextupole bounce back (snapback) from the final injection decay value to the original hysteresis curve was the reason for this effect. The following investigations were focused on the influence of the variation of injection porch duration on sextupole snapback. But unfortunately no functional dependence of snapback as a function of injection porch duration was deduced.

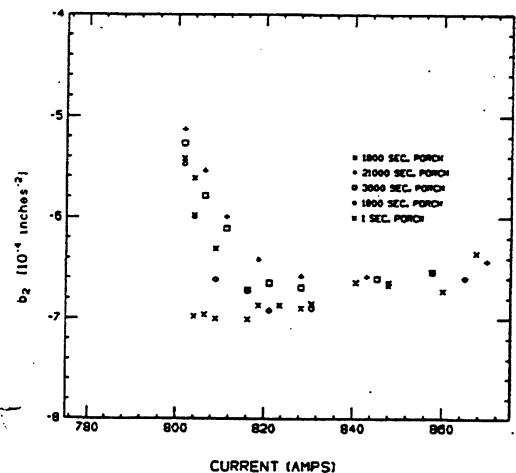


Figure 2.6: First systematic sextupole snapback investigation at the Tevatron. Snapback is plotted as the function of dipole excitation current for different injection porch duration. [35]

Therefore the data in Figure 2.6 was used to correct the dynamic effects of each acceleration run. The difference between that curve and the hysteresis was calculated. Immediately before the ramp, so-called look-up tables were generated. In these tables the time at injection current and acceleration energy specify a ramping condition. Loading these tables into the hardware ramp generator in order to provide sufficient sextupole correction, finally led to an overall transmission rate of 96% for protons and antiprotons to an energy of 900 GeV [35].

R.W. Hanft presented a first systematic survey of experiments concerning the sextupole decay behavior and its dependence on operation cycle variations in March 1989 [37]. Because of the important circumstance that this is the first presentation of a dedicated measurement program of dipole magnets as far as dynamic effects are concerned, we will go through his report in details and learn as much as possible from his experience.

The first part of the presentation deals with results obtained from one 0.81 m long model Tevatron magnet, which was installed in a vertical deware. The magnetic field was measured with a Morgan coil rotating at 6 Hz. In order to derive normalized data, all magnets were quenched before each run. The helium bath temperature was 4.2 K for most of the experiments. Long term and transition stability of the power converter was also considered.

The first experimental run shows the dramatic influence of different types of approaches on one certain dipole excitation current. Once the magnet is ramped directly to 400 A, the decay rate is significantly smaller than in a quite similar cycle containing a current ramp up to 4 kA and a ramp down to 400 A. Apart from different absolute decay rates we see another interesting detail. Both decay curves show significant change in decay rate after a certain time on the porch. After that time the decay becomes $\log(t)$ like. Thus the source of the effects was at first suspected to be "flux creep". The dipole current cycles are shown in Figure 2.7 and the results are shown in Figure 2.8. The nominal ramp rate is given with 100 A/s.

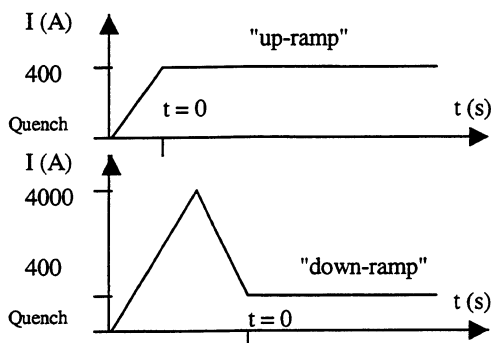


Figure 2.7: Current cycles for the first decay experiment.

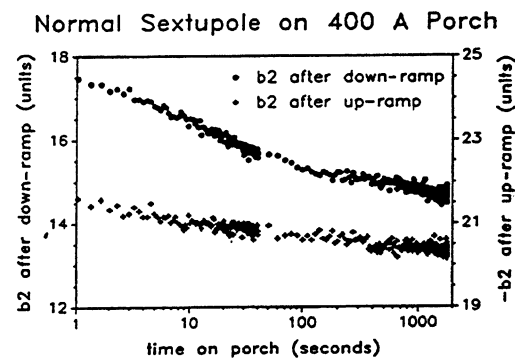


Figure 2.8: Time evolution of the normal sextupole on a 400 A porch. [37]

The basic shape of cycle was retained during the second experimental run. A change of the measurement porch from 400 A to 800 A provided one modification. The other modification was given by a variation of the ramp rate (25 A/s, 100 A/s, 200 A/s, 800 A/s) for the first slope approaching directly at 800 A and at 4 kA in case of cycle two.

Both results showed that the decay rate strongly depends on the ramp rate prior to the porch for the first 10 s on porch. Thereafter the sextupole showed a linear decay in a logarithmic time scale. The cycle including the 4000 A peak current (Figure 2.10) showed a more pronounced decay than the cycle with direct approach at 800 A (Figure 2.9).

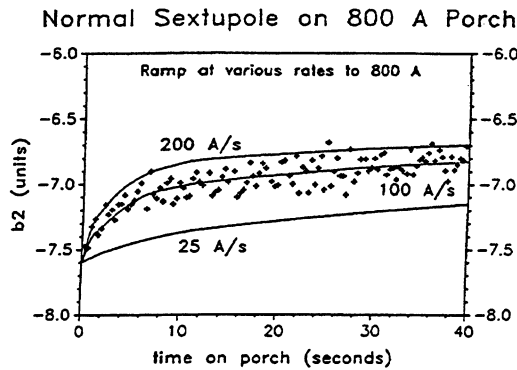


Figure 2.9: Time evolution of the sextupole on an 800 A porch on an up-ramp. [37]

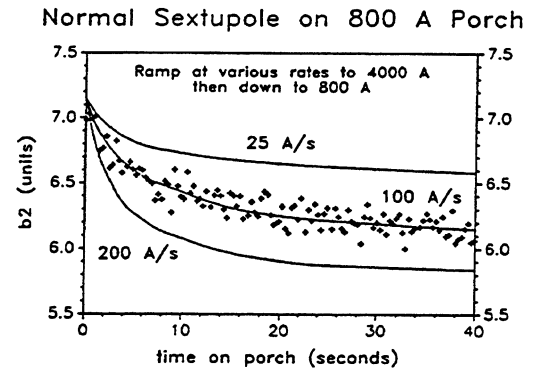


Figure 2.10: Time evolution of the sextupole on an 800 A porch on a down-ramp. [37]

The design of the current cycle for the third experimental run was strongly orientated to the real operation cycle as in use for the fixed target model. The cycle and the magnetic measurement results are given in Figure 2.11 and Figure 2.12. It is remarkable to see that sextupole as well as decapole decayed approximately linear with $\log(t)$. But there was said to be a structural particularity after a long duration on injection porch. Performing the same experiment for different temperatures (3.6 K and 3.2 K) revealed a more negative value of sextupole at the start of the porch than expected in simple theory due to the increase of the superconductor's critical current J_c with decreasing temperature. It was observed that the sextupole change rates per time decade are the same for all temperatures.

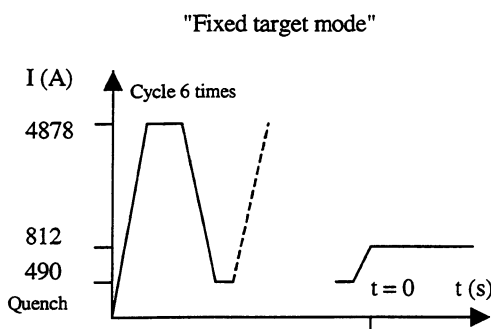


Figure 2.11: Current cycle for Tevatron's fixed target mode.

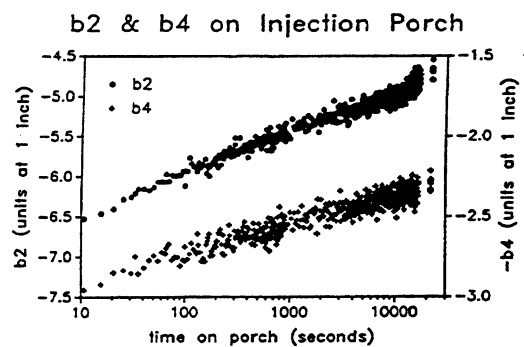


Figure 2.12: Time evolution of sextupole and decapole on the injection porch at 812 A of an accelerator-like current waveform. [37]

On the bases of these snapback studies an experiment was designed by varying the time structure at the beginning of the current waveform while increasing the current at the end

of injection porch duration. The result of this experiment showed that sextupole snapback is a function of the current and not of the current change rate in time.

Some other experiments were performed on seven randomly chosen dipole magnets passing the production test facility. All magnets were powered by use of a standardized current cycle. This standardization was the basis for the comparison of the results obtained from different magnets. The cycle started with quenching the magnet, followed by a nominal ramp of 110 A/s up to 4 kA. After a 1-second-long flat top the magnet was ramped down to 0 A. The measurements were made at 0 A where the time scale is set to zero. Four of these magnets (see Figure 2.13) showed in consistency with the short model magnets, an initial rapid decay followed by a $\log(t)$ behavior after a few seconds. Furthermore the remnant dipole was said to follow the decay of the sextupole, indicating that both fields arise from the same currents. The influence of the ramp rate (10 A/s, 25 A/s, 110 A/s, 300 A/s) during the ramp from 0 A to 4 kA is shown in Figure 2.14. Higher ramp rates yielded larger remnant magnetization, which initially decayed more slowly. But for longer times on porch the decay rate of the slow ramp exceeded that of the higher one.

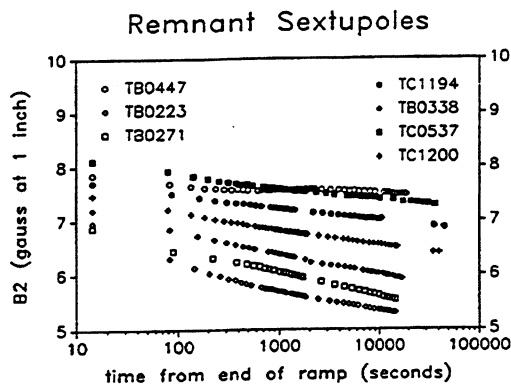


Figure 2.13: Decay of remnant sextupole after a single per-cycle. [37]

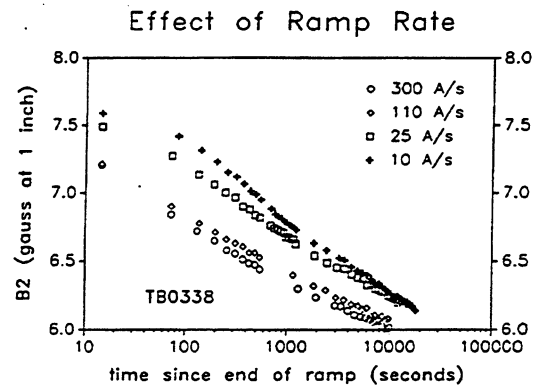


Figure 2.14: The influence on remnant sextupole behavior caused by varying the ramp rate of a single pre cycle. [37]

The effect of multiple consecutive ramps on sextupole decay and remnant sextupole is shown in Figure 2.15. As the number of ramps was increased, the remnant sextupole observed at the end of the final ramp decreased in magnitude. Observing the slope one can see that the remnant sextupole decayed more quickly. The most pronounced effect was observed for data taken after one and two ramps. Investigations into the effect of the flat top duration (Figure 2.16) of a single ramp showed that a longer flat top duration resulted in lower initial sextupole. But the subsequent sextupole decay could no longer be approximated by a linear $\log(t)$ dependence.

Finally we will end our digression through the first experiments and experience at Tevatron with two statements from leading researchers at Tevatron, which show the state of time dependent effects research at the end of the last decade.

Concerning the linear logarithmic behavior of decay Hanft concluded:

"In many situations the time evolution of field harmonics exhibits a $\log(t)$ dependence indicative of flux creep. Detailed understanding is not yet available, and it is clear that a complete description must accommodate other processes."[37]

Herrup however, does not sound too enthusiastic as far as flux creep was concerned:

"Although theoretical understanding of the process in terms of the critical state model and flux creep have provided useful guidelines for plotting the results of these measurements, we have not yet been able to understand the details of our measurements based on these pictures.

...we observed a large number of as yet puzzling effects which we have not fitted into a coherent phenomenological framework." [36]

But even if the situation concerning the theoretical understanding of the observed effects was not satisfying, a sufficient correction of the existing Tevatron machine was derived from the available chromaticity and sextupole field component measurements. This correction provided a sufficiently low loss rate of particles on their way from injection to collision energy.

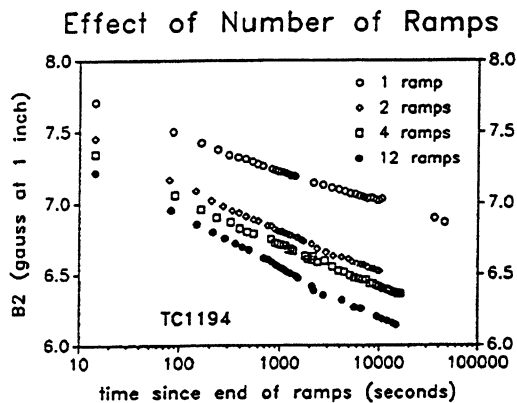


Figure 2.15: The effect on remnant sextupole behavior caused by making multiple consecutive ramps prior to measurement. [37]

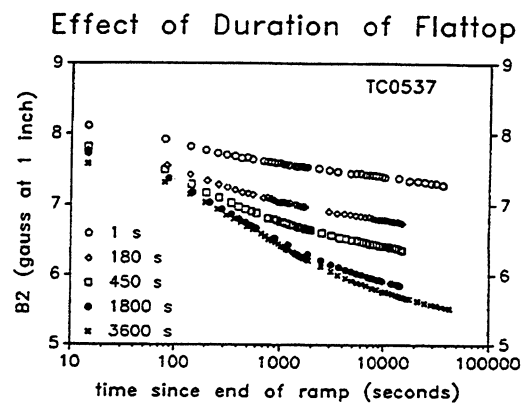


Figure 2.16: The effect on remnant sextupole behavior caused by varying the duration of the single flat top.[37]

2.2. Early Considerations of Flux Creep in SSC dipole magnets

The Superconducting Super Collider (SSC) project [38], which was founded due to a recommendation of the HEPAP, the High Energy Physics Advisory Panel of the US Department of Energy (DOE), was historically thought to become the leading edge particle accelerator world-wide. This machine [40] would provide 20 TeV on 20 TeV proton-proton collision with a luminosity of $10^{33} \text{ cm}^{-2} \text{ s}^{-1}$. This value must be seen in comparison to the Tevatron design luminosity of $10^{30} \text{ cm}^{-2} \text{ s}^{-1}$. The SSC beam energy was designed to be sufficient enough to probe into domains of particle physics where markedly new phenomena were expected. The concept of the SSC accelerator design was based on a series of four major injectors of increasing energy leading into the superconducting Collider Ring System. The injector system consisted of a Linac (600

MeV), the Low Energy Booster (8 GeV/c), the Medium Energy Booster (100 GeV/c), and the High Energy Booster (1 TeV), which would be superconducting in order to limit the physical size. In the Collider Ring the proton beams were housed one above the other in an underground tunnel of 83 km in circumference. A standard dipole was designed to have a magnetic length of 16.6 m and a maximum field of 6.6 T. The total number of dipoles was 7680. Due to a budget reduction the project was terminated by a Congress decision in July 1993 [39].

In 1989 W.S. Gilbert edited the first SSC publication concerning the subject of field component decay [41]. He stated results obtained from nine magnets. The studies dealt with the subject of power supply overshooting, influence of ramp rate on decay, and finally influence of temperature on decay. Concerning power supply overshooting results showed different initial sextupole values and different decay rates. The ramp rate experiment did not show any obvious systematic impact on decay. But the temperature influence experiment revealed for the first time that measurements at 4.3 K and 1.8 K show significantly different decay rates. This last result must be seen in relation to the results from Tevatron where measurements at 4.2 K, 3.6 K and 3.2 K did not show any significant change in decay rate. Gilbert concluded that SSC dipole models show a roughly linear log time relationship and suggested flux creep as source of the phenomenon. Furthermore the effect was assumed

"...to be a bulk property effect and not particular sensitive to the details of the conductor design."

2.3. Experience with Field Component Decay and first observations of Periodic Pattern at HERA

The Hadron-Electron Ring Accelerator facility (HERA) is the final accelerator-storage ring of the Deutsches Elektronen-Synchrotron (DESY) laboratory in Hamburg, Germany [42]. Similar to other machines the DESY accelerator chain consists of several pre-accelerators providing the required particle injection energy for the HERA machine. HERA is designed to provide 820 GeV protons to collide with 30 GeV electrons with a luminosity of $5 \cdot 10^{31} \text{ cm}^{-2}\text{s}^{-1}$. The construction started in 1984 and was finished in 1990. The first electron-proton collision took place on 19th October 1991. The magnet system of HERA [46] contains 650 superconducting dipole and quadrupole magnets and more than 1500 superconducting corrector units. The ring is installed in a 6.3 km long tunnel, the superconducting proton storage ring above the electron storage ring. The injection energy of the proton ring, which requires a dipole current of 250 A, is 40 GeV. The nominal field for the main bending HERA dipole magnets is 4.682 T, which is achieved by a nominal operation current of 5027 A. Dipoles and quadrupoles are powered in series.

Alarmed by the activities during the Tevatron commissioning phase and the circumstance that filling the HERA machine with its 210 proton bunches lasted approximately 30 minutes first measurement took place at HERA. Because of the importance of chromaticity and tune control and the unsatisfying situation as far as the theoretical explanation or modeling were concerned all dipole magnets were to be measured under cryogenic nominal operation conditions [43].

A normalized power cycle, which started with quenching the magnet, was chosen in order to provide comparable magnetic measurement results. The dipole magnets showed linear decay in the logarithm of time for dipole and sextupole field component. An equal behavior was seen in the 12-pole of the quadrupoles. But the strict linear logarithmic fit could only be successfully applied in a time window of 200 to 2000 seconds after start of injection.

The first results of these series measurements were presented at the 11th International Conference on Magnet Technology. This presentation revealed at least one new aspect. The most important result was the fact that decay rates differed by a factor of two for magnets built by different superconductor producers. This result is shown in the histogram of Figure 2.17, where the number of magnets is plotted versus the sextupole decay rate between 200 and 2000 seconds at injection porch. But it is also mentioned that the systematic offset must be seen in the light of a random error for each measurement, which might be due to insufficient power converter regulation. This uncertainty for one magnet, which was measured repeatedly over a period of two months, is shown in the small insert of Figure 2.17.

Furthermore it is of high interest that the systematic offset in sextupole decay for two different superconductor producers is also seen in the dipole. There is a significant correlation between B_1 and b_3 for both producers. The correlation is shown in Figure 2.19 and the standard current cycle is shown in Figure 2.18. Special investigations concerning the powering history influence on the sextupole decay rate were started. The number of pre-cycles was varied between 1 and 6. In contrast to Tevatron results no change in decay rate was observed. Changing the ramp speed of the injection approach from 1 to 20 A/s or extending the break at 6000 A to 30 minutes did not show an appreciable effect on the decay rate.

For the machine operation it was clear that no theoretical approach in this relatively new field of research would help to guarantee optimum performance of beam parameters. Thus at DESY a systematic measurement program was established in order to analyze the influence of current cycle variations on the field component decay. The mission goal of this task was to search for cycles, which reduce the decay behavior. First results showed that for dipole (Figure 2.20) as well for as sextupole (Figure 2.21) a lower flat top current of the pre cycle led to a significantly reduced decay [44].

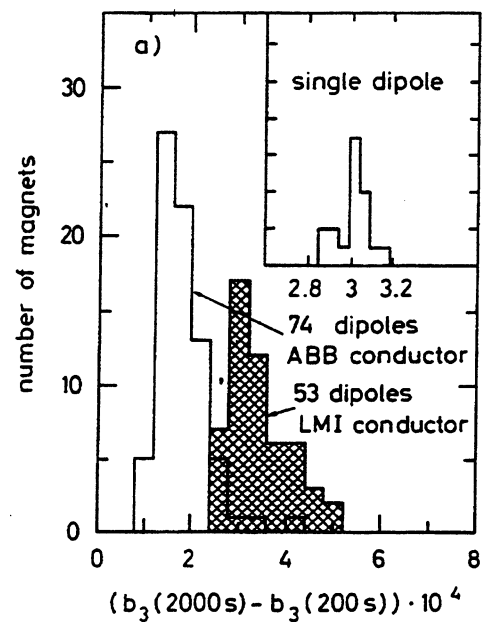


Figure 2.17: Decay rates for the sextupole components of dipoles assembled with two different conductors. [43]

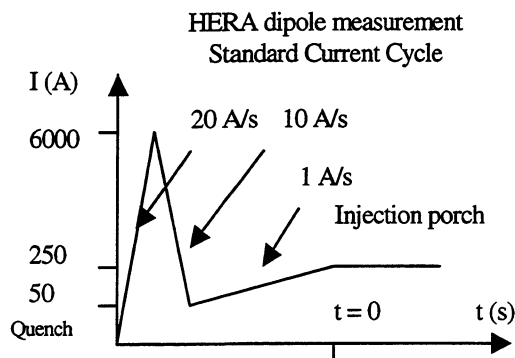


Figure 2.18: Standard current cycle for superconducting dipole series measurements at HERA.

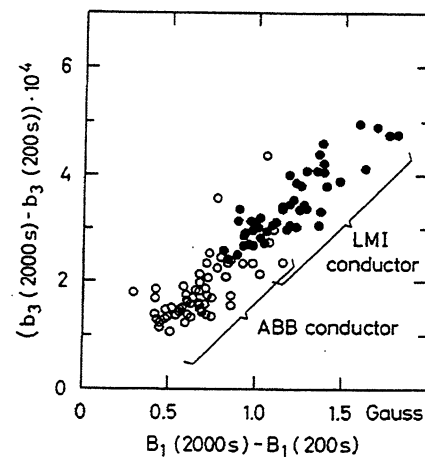


Figure 2.19: Correlation between the decay rate of the sextupole and the main field in the HERA dipole magnets. [43]

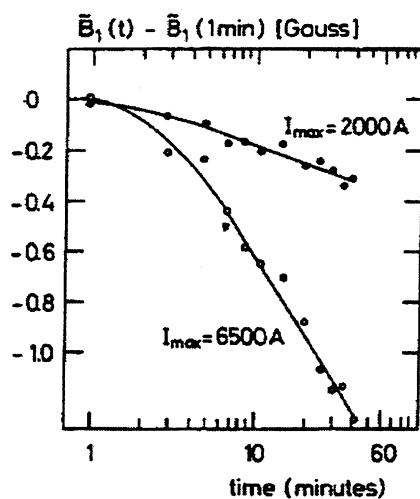


Figure 2.20: Dipole decay rate during injection as function of a single pre-cycle current. [44]

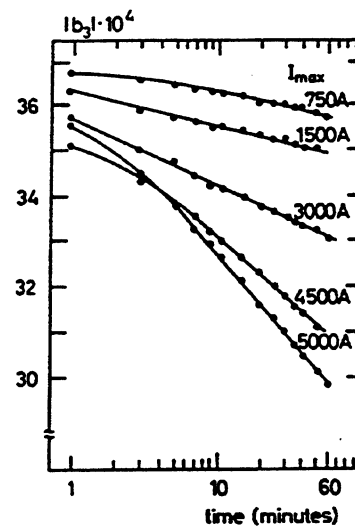


Figure 2.21: Remnant sextupole of a HERA dipole as function of a single pre-cycle current. [44]

But due to the fact that an initial quench for all 600 magnets was not applicable for machine operation another procedure had to be defined. When a new injection was needed, the magnets were usually powered to high current. Thus another cycle containing a second pre-cycle with maximum currents of 750 A, 2000 A, 3000 A, and 4000 A was tested. Unfortunately all measurements showed the same decay rate during injection porch.

Another attempt of defining a cycle with reduced decay was performed by introducing a break in the down-ramp part of the second cycle (Figure 2.22). While a break of 30 minutes at high current had no effect, a waiting period at low currents (250 A or 50 A) turned out to be quite efficient.

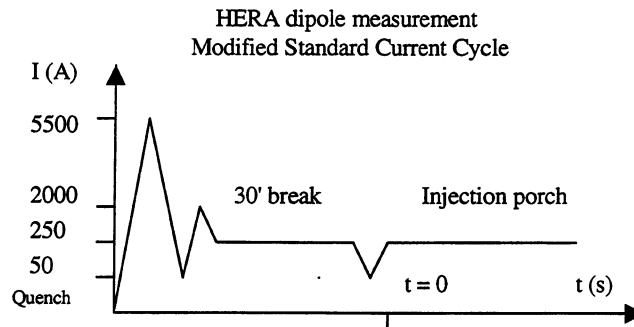


Figure 2.22: Modified standard current cycle for HERA dipole measurements.

The big advantage of this new initialization procedure is not only that the decay during injection is significantly reduced; furthermore the hysteresis curve is reached much faster than with the single pre-cycle initialization. The influence on decay is shown in Figure 2.23, while the effect on snapback is plotted in Figure 2.24. Today the break before approaching the injection is called pre-injection porch. One has to note that it is of crucial importance to reach the injection porch by following the up-ramp. Following a down-ramp would mean that injection would be reached on the upper branch of the hysteresis.

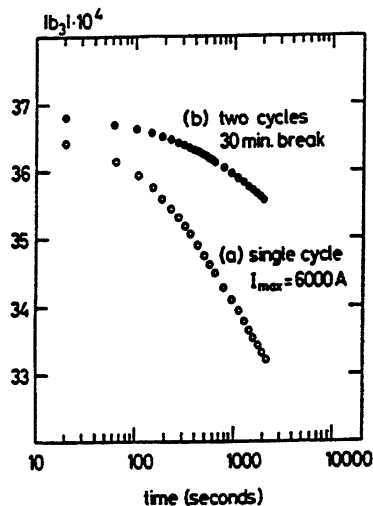


Figure 2.23: Comparison of the sextupole decay in case of one single pre-cycle and two cycles with additional break. [44]

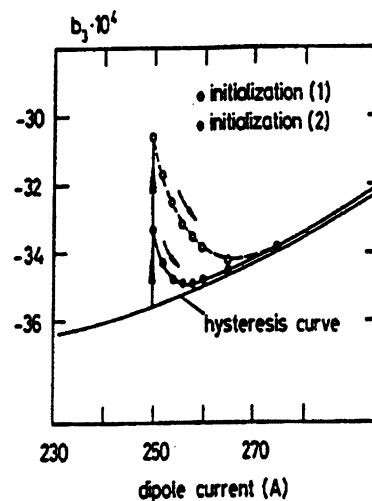


Figure 2.24: Influence of modified initialization cycle on the sextupole snapback. [44]

As far as the influence of different initialization procedures on decay and snapback is concerned, we have to understand that neither the relative spread between different magnets from one producer, nor the difference between magnets built from the two superconducting cable producers was effected.

Finally H. Brück concluded the extensive studies of the HERA dipoles with the statement:

"...In spite of the unsatisfactory state of the theoretical understanding, the extensive measurements made on all HERA magnets will provide sufficient information for a reliable compensation of the field distortion." [45]

As an implication of the experimental experience the early considerations (June 1990) about a correction system of HERA included two reference dipole magnets, one from each producer, which were powered in series with the ring magnets. They are equipped with NMR probes for dipole component measurements, pickup coils and sextupole sensors. The measured field values and their dynamics were used to be included in a feed back loop in order to set sufficient corrector magnet currents [44].

Apart from studies of field decay and snapback, another conspicuous phenomenon was observed in HERA dipole magnets. The surprising observation was made that sextupole field exhibits a sinusoidal structure along the axis of the magnet [47]. The so-called periodic pattern was for the first time observed during measurements with a sextupole detector. The detector was built up by three hall probes, which were mounted on an equilateral triangle. The hall plates were powered with an AC current source and temperature stabilization was foreseen. The time resolution of the sensor was given with 0.3 seconds and the spatial resolution was better than 0.5 mm. The field periodicity was also detected in the dipole field by use of the NMR probe. Finally a 2 cm long tangential pick-up coil was used to determine all normal and skew harmonics. It was observed that the periodicity exists in all allowed and non-allowed harmonics.

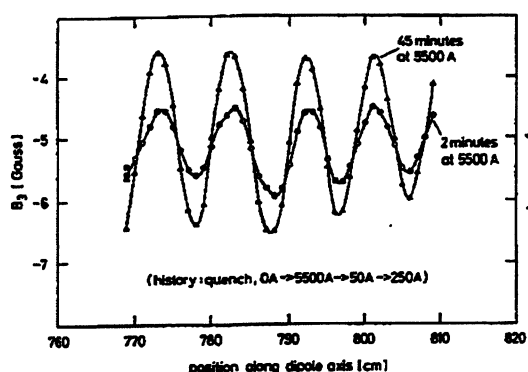


Figure 2.25: Sextupole periodic pattern at injection as function of flat top duration in the preceding cycle. [47]

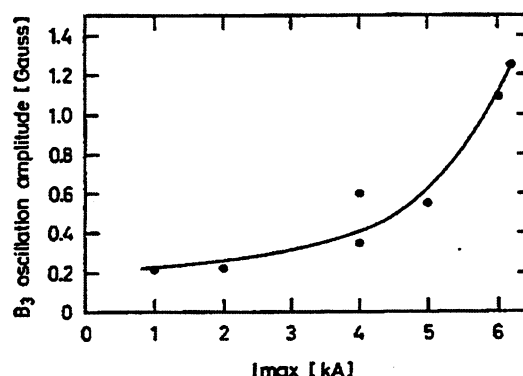


Figure 2.26: Sextupole periodic pattern amplitude at injection as function of flat top current in the preceding cycle. [47]

The periodicity vanished when the magnet was brought into the normal state and the spatial wavelength corresponded with the twist pitch length of the superconducting cable of the coil. This and the fact that the periodicity does not exist in the virgin magnet but appears gradually with increasing current lead to the assumption that the periodic structure in the field components might be caused by super currents flowing in the strands of the Rutherford-type cable. Moreover the periodicity persisted for more than 12 h without attenuation when the magnet was exposed to a certain power history and finally set to zero transport current. The periodicity was invariant through the whole hysteresis loop.

Even though this newly observed effect has no direct connection to the concept of decaying field components, the importance of periodic pattern is best described in a quotation presented in 1991.

"...The oscillation amplitude measured at low field depends strongly on the magnitude and duration of the maximum field in the preceding cycle. A similar dependence was previously observed for the decay rates of the magnetization. Both effects are probably related."

The results leading to this opinion are shown in Figure 2.25 and Figure 2.26 where the periodic pattern amplitude is plotted as function of flat top current respectively flat top duration. We should at least keep these two charts in mind because they somehow contain the basic idea of our phenomenological model, which we derived after studying a dynamic effect scaling law.

2.4. Contributions from UNK and SSC to the puzzle of slow field component decay

The Accelerator-Storage Complex (UNK) was one of the traditionally very ambitious projects of the former Soviet Union. Similar to other machines of this type, the accelerator system hosts a chain of pre accelerators usually based on normal conducting magnets. The final Accelerator-Storage Complex was designed to contain 3500 superconducting magnets. Most of them should have been the 2200 superconducting dipole magnets. The design luminosity of the UNK hadron-hadron collider was given by $10^{32} \text{ cm}^{-2} \text{ s}^{-1}$. The UNK should have provided accelerating mode with a fixed target and proton-proton collider mode.

The project was established in 1982. But due to a budget reduction and changes in the political structure of the Soviet Union research on the superconducting part of the machine was terminated in 1990. This decision in conjunction with the more dramatic termination of the SSC project by the US congress might lead to the opinion, those projects of these financial and time dimensions can no longer be afforded by single nations.

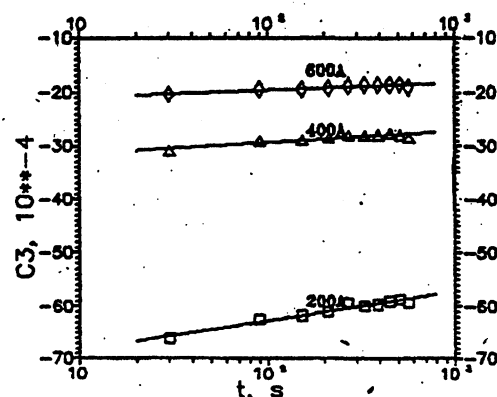


Figure 2.27: Influence of the injection current level on the sextupole decay rate of a superconducting UNK dipole magnet. [48]

The importance of dynamic effect studies at UNK was mainly determined by the considerations that the machine should operate at a nominal ramp speed of 0.1 T/s. This ramp speed must be seen in comparison to the ramp speed of 0.01 T/s for HERA and 0.04 T/s for SSC.

Concerning the slow field drift at injection one has to mention one experiment of interest. The influence of a different injection current on the sextupole decay during injection was investigated. The result of this experiment shows a significant decrease in the decay rates for an increasing injection current [48].

Meanwhile the research effort at SSC showed serious progress. M. Wake [49] reported about a test of several 1.5 meter models of the SSC collider dipoles at Fermilab. Details of the construction were discussed and measured and computed field components were compared. The evolution of periodic pattern in respect to the finally reached current was shown. But experimental results were not yet understood.

Another interesting study of time dependent effects in a full-length (17 meter) 4 cm aperture SSC dipole prototype was provided by A. Devred et al. [50]. The magnet was built at BNL and cold tested at Fermilab. The applied measurement technique was based on a 0.6 meter long rotating coil unit. The revolution period was 3.2 seconds while the maximum data rate was one measurement per 20 seconds. Data were "*feed down*" corrected from the 22 pole because of errors due to misalignment of the rotating coil's center and the magnetic center of the dipole coil. To avoid an unwanted influence of the powering history on the results of field component decay, the magnet was quenched (*cleansing quench*) followed by a cycle simulating a colliding beam cycle (*per-cycle*), ramped down to 120 A in two minutes and finally ramped up to *injection porch* at 635 A. Measurements were taken at injection. The effect of the flat top current and temperature variations on the sextupole decay was of primary interest.

A series of different flat top current experiments were performed. The decay was characterized by a faster transition within the first 300 s on injection, but it was independent of the pre-cycle flat top. The following long lasting phase strongly depended on the flattop current. Both phases were characterized by a logarithmic decay. The decay as function of different flat tops is shown in Figure 2.28. Plotting the second decay rate versus the pre-cycle flattop current revealed another interesting fact. The decay rate appeared to be independent of the current below a certain threshold and increased linearly with flattop current. This circumstance is shown in Figure 2.29. Again we have to remind to keep this particular result in mind for later use. Furthermore we may compare this result with the periodic pattern amplitude dependence on the flat top current (Figure 2.26).

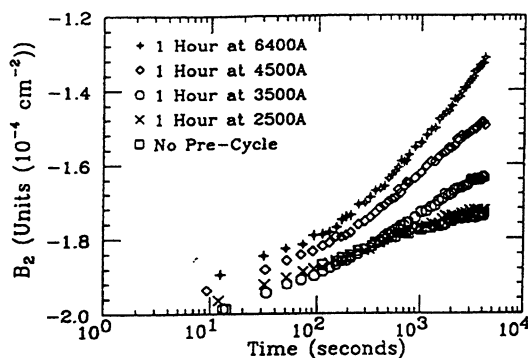


Figure 2.28: Influence of the flattop current on the decay of the sextupole component of a SSC 17 meter long dipole magnet during injection. [50]

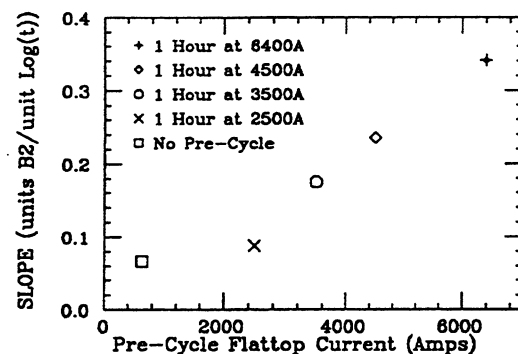


Figure 2.29: Decay rate as a function of the flattop current for a full-length superconducting SSC dipole magnet. [50]

The research focused on temperature influence on sextupole decay was based on two current cycles. One cycle was given by quenching the magnet and performing a single

ramp to injection. The other cycle started with quenching the magnet, followed by a single pre-cycle to 6400 A for 15 minutes, finally ramping down the magnet to 120 A and approaching at injection. Three different temperature cycles were introduced in both current cycles. Two measurements were performed with fixed temperature at 4.35 K respectively 3.8 K. The third temperature cycle starts with 4.35 K. But after 600 seconds on injection, the temperature were dropped by 0.5 K. Both current cycles and sextupole measurements are shown in Figure 2.30 to Figure 2.33.

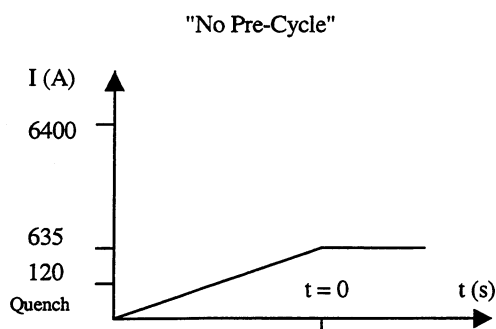


Figure 2.30: SSC temperature experiments - direct ramp to injection porch.

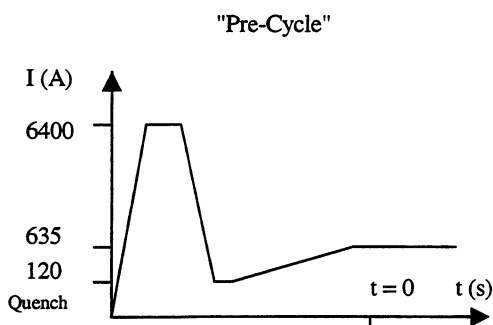


Figure 2.32: SSC temperature experiment - pre-cycling before ramping to injection porch.

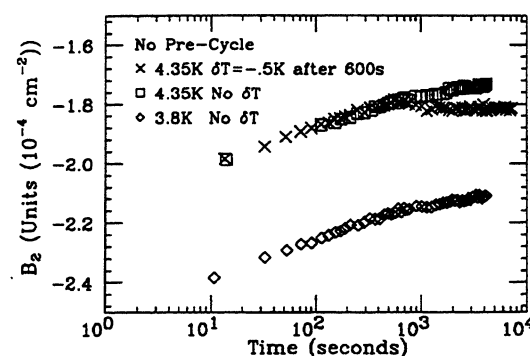


Figure 2.31: Sextupole decay during injection versus time without pre-cycling of the magnet. [50]

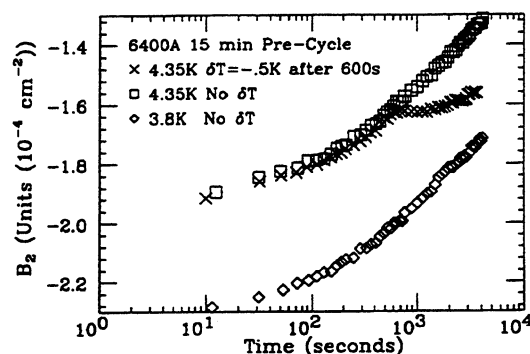


Figure 2.33: Sextupole decay during injection versus time including pre-cycling of the magnet. [50]

The first obvious result was a difference in the initial magnetization of both cycles. This was consistent with the expected difference between a virgin curve of a superconducting material and following the hysteresis while repeatedly cycling down to a minimum current. Both curves (4.35 K and 3.8 K) showed a systematic offset as well a parallel decay behavior. The difference between the 4.35 K decay curve and the 3.8 K decay curve was understood as an increase of the magnetization due to an increased critical current caused by lower temperatures. Up to here the system of a superconducting cable was well understood.

Again we see significantly different decay rates concerning different power cycle forms. Off course this fact was observed already several times before.

But the results of the temperature variations in both experiments was the real milestone in the research concerning slow field component decay is given in. It was observed that in case of the "No Pre-Cycle" experiments a decrease of temperature while on the injection porch effectively stopped the decay. In contrast to this result a decrease of temperature in case of the other cycle reduced the decay rate but did not stop it. The fundamental difference led to the conclusion that in case of the cycle without pre-cycle the major contributions to the field component decay must be made by flux creep. But in the other case the decay must consist of two contributions. One of course was supposed to be still flux creep, while a second, stronger source boosted the decay. The second source seemed not to be affected by the temperature. This fundamentally new understanding of two interacting effects must be explicitly mentioned at this point because it provided the basis for our phenomenological model. Furthermore it opened the way to research in direction of "Supercurrents" or "Boundary Induced Coupling Currents" (BICCs). This finally led to our present understanding and modeling of the electromagnetic properties of the superconducting Rutherford-type cable.

Today we believe that R. Stiening for the first time ever (1991) published the idea of time dependent trapped currents with sextupole symmetry within the superconducting cable of the magnet. These currents should be superimposed to the transport current in the strands of the Rutherford-type cable. He explained:

"It is the purpose of this note to point out that the time dependence of trapped currents is a powerful mechanism for causing the time dependence of 'persistent current' multipoles." [51]

Some other authors [16, 20] followed this idea in the last seven years proving us with a good fundamental knowledge about current imbalance in the strands of the Rutherford-type cable and the impact on field quality in superconducting magnets. But there are still some open remaining questions, which require research.

2.5. Clarifying the flux creep contribution at HERA

Following the opinions and experiments of several researchers in the last sequences of this historical review, we see that the effect of the slow time dependent decay of the field components must consist of at least two components. These components are firstly the trapped currents in the strands of the cable, which decay in time, and secondly the natural decay of the magnetization of the superconducting material due to flux creep.

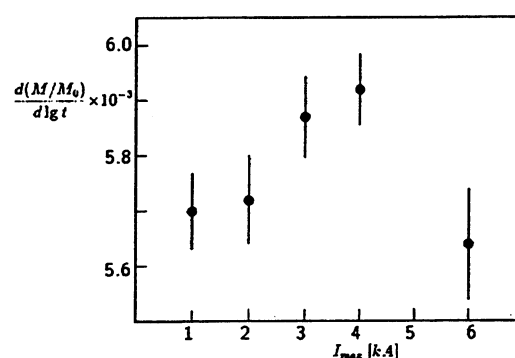


Figure 2.34: Decadic decay rate of magnetization as function of the pre-cycle current from HERA cable samples. [52]

In 1992 we received an interesting contribution to the clarification of the question of the strength of the flux creep influence on the total field component decay. In his diploma M.

Halemeyer introduced a method for measuring the magnetization of superconducting HERA cables and its time dependence [52]. In contrast to methods using only short samples of strands of the superconducting cable this new method allowed the determination of the magnetization of a cable of a few meters of length. A dipole coil, in which the sample coil was inserted, formed the experimental set-up. A decapole sensitive pick up coil was used for the measurements. This experiment verified that the magnetization decay due to thermally activated flux creep was independent of the applied current cycle. Furthermore it was proved that the geometric properties like the twisting of the strands of the superconducting Rutherford-type cable, did not influence the natural decay rate of magnetization. The result of this experiment was given in form of the decadic decay rate

$$\frac{d(M(t)/M(t_0))}{d \log(t)} = (0.579 \pm 0.012) \frac{\%}{\text{Decade}} \quad (2.3)$$

The decadic decay rate as function of the pre-cycle current is shown in Figure 2.34. We see a constant decay rate for all pre-cycle currents.

2.6. Periodic pattern studies at BNL

After understanding that two interacting effects may cause the field component decay and identifying one of them as the magnetization decay due to flux creep in the superconducting Rutherford-type cable, one significant part of the puzzling effect was not yet truly understood. But due to the fact that there was a strong indication that periodic pattern causes enhanced field component decay, the direction of research was defined. Thus from 1992 to 1994 a series of publications by the Brookhaven National Laboratory (BNL) focused on the subject of periodic pattern. The measurement technique in most of the experiments was based on sextupole sensitive Hall plate configurations [54].

The periodic pattern study of Ghosh et al. involved 15 magnets of different accelerators and different length. But although each of the 15 magnets of the population had unique features a very common behavior was observed. In all cases the wavelength of periodicity was equal to the twist pitch of the inner cable. Even magnets with one, two, three or four layers had similar pattern properties. Normal and skew components showed a random phase. It was observed that the skew component amplitude variation could be larger than the normal one. The amplitude of the oscillation decreased with the harmonic number. The amplitude of the periodic pattern only appeared when the magnet was held at high field for some time. For a given field level the observations revealed exponentially increasing amplitude with time. This observation for the first ever led to the idea of a close parallelism between the observed phenomenon and the charging of an electric circuit (Figure 2.35). The typically observed time constant was 500 seconds [55]. The decay of the periodic pattern amplitude was characterized by at least three time constants. Furthermore it was stated that such a sum of exponential functions might look like a straight line in a plot with a logarithmic time scale. Increasing the current up to a certain level and holding it constant while measuring the sextupole periodic pattern amplitude before ramping to the next level showed an almost linear increase in peak to peak amplitude with increasing current (Figure 2.36) [55].

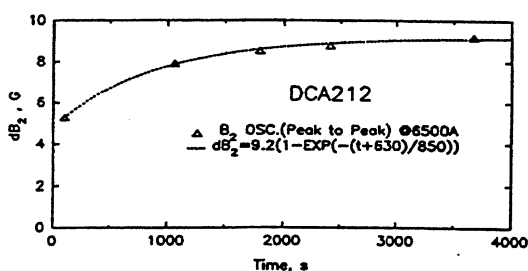


Figure 2.35: Sextupole peak to peak amplitude as function of the flat top time at 6500 A of the magnet excitation current. [55]

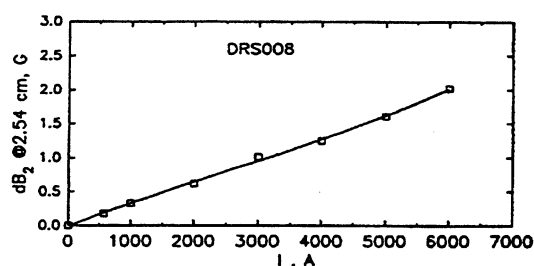


Figure 2.36: Sextupole peak to peak amplitude as function of the magnet excitation current. [55]

Heating the outer layer of the coil showed no effect on the periodic pattern amplitude, while increasing the heat energy until the inner layer reached normal state, erased the periodic pattern amplitude.

Thus W.B. Sampson and A.K. Ghosh prepared another experiment at BNL [57]. They installed a pair of prototype SSC coils in the bore of a 7 T test dipole. This magnet was thought to be a good test device because the cable of the magnet was wound from one single piece of conductor. Thus the cable had very uniform strand to strand properties and early measurements indicated much less axial periodicity than for the typical SSC coil. The experiment should reveal if axial oscillation could be induced in windings free of transport current. Due to the length of the SSC coil only half of it was in the bore of the test magnet. The soldered ends were removed and there was no contact between the two layers of the SSC coil. Stainless steel foil heaters were installed on the windings near the end and not in the field. First investigations showed that axial periodic pattern appeared in the bore of the coil, which was not powered and not inside the test magnet. The amplitude of the periodicity increased as the field was increased and decayed at constant level. Decreasing the field led to a decreasing periodic pattern amplitude. Thus change in sign was possible because of the decay during constant excitation level. The amplitude measured inside the test magnet was twice as high as outside. These basic observations clearly showed that earlier speculations about establishing periodic pattern at high field level close to the critical current were wrong.

When the periodicity outside the test magnet was erased by heating a spot heater at a field level above zero, the periodic patterns were established with an opposite sign in amplitude as soon as the field of the test magnet was reduced to zero. This technique was applied in a study of field step influence on the amplitude of periodicity. Equal steps in field were applied to the up and down ramp. A measurement sequence and an elimination of the periodicity followed each step. For each field level the amplitude as well as the time dependence was found to be equal. The importance of these experiments is expressed in the conclusion of this work, in which the existence of unbalanced currents is explicitly mentioned.

"The fact that axial pattern appear in the part of the coil not in the applied field implies that unbalanced currents are induced in the strands of the superconductor and that the phenomenon is not a magnetization effect." [57]

But there were still some open questions concerning the long-lasting decay of the trapped current. Because of the enthusiasm about periodic pattern the original idea that flux creep caused field component decay was suddenly completely absent in topical discussions.

Other experiments dealt with the ramp rate influence on the periodic pattern structure of a number of SSC dipoles [58]. The results generally revealed that magnets with intermediate inter-strand resistance ($79 \mu\Omega$) showed quite a different behavior from magnets with low inter-strand resistance ($6 \mu\Omega$). These experiments verified that conductors of very low inter-strand resistance show enhanced periodic pattern oscillations during ramping.

Deduced from all the experimental results available already in the middle of 1992 it was clear that the problem of decaying field components must be in a close connection with the unbalanced currents in the Rutherford-type cable.

"It can be stated that without establishing an oscillation pattern, the sextupole drift in time is very small. Therefore enhanced sextupole decay must be a result of significant unbalanced currents that decay in a manner which changes the average sextupole field." [55]

2.7. Most recent activities in beam parameter control at HERA

Meanwhile the interest at HERA was obviously focused on establishing procedures, which provide the required beam parameter control during injection and acceleration. The dramatic influence of slowly decaying persistent currents during injection on the chromaticity of HERA is shown in Figure 2.37. The change in chromaticity exceeded far beyond the maximum accepted limit of a few units [63].

Thus the machine is equipped with two reference magnets - one magnet for each producer. They are connected in series to the ring magnets in the accelerator tunnel and therefore represent the behavior of the whole magnet assembly. A change of injection field is detected with NMR probes and Hall probes and the horizontal orbit correction coils are adjusted. During the ramp a stationary pick-up coil is used to measure the dipole field in the reference magnet. It synchronizes all other elements in the machine to the dipole field independent of the particular details of the hysteresis curve.

Measurements with a rotating coil give the sextupole contribution of the dipole magnets. Changes in the sextupole component due to persistent current decay, hysteresis or re-induction are computed and sextupole correction coils are set at injection and during the ramp to 150 GeV, where persistent current effects no longer play an essential role. This is because of three reasons. Firstly the saturation current density decreases rapidly with the increasing dipole field. Secondly the main current in the conductor gradually displaces the persistent currents. Thirdly the relative contribution of the sextupole component to the main dipole field also decreases. The quality of this correction system can be seen in Figure 2.38. In contrast to Figure 2.37 we see well controlled chromaticity values during injection.

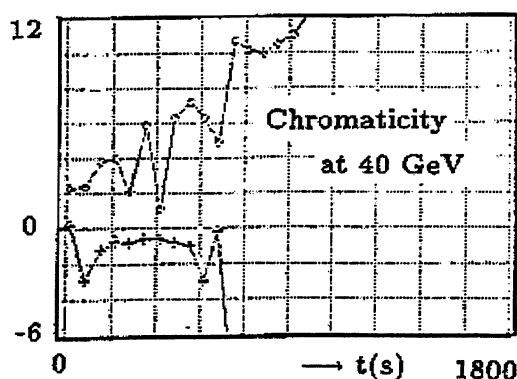


Figure 2.37: Drift of chromaticity in both planes in different directions due to changing the sextupole component during injection. [63]

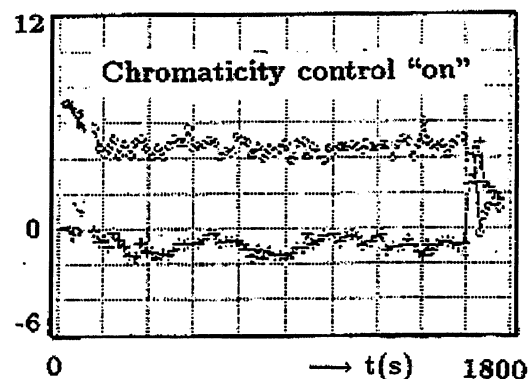


Figure 2.38: Chromaticity control by use of the feed back loop during injection. [63]

The start of the acceleration ramp is one of the most critical points in the accelerator operation. At HERA this part of the energy transition is divided into sections (see right part of Figure 2.39) [64]. The first section covers the acceleration from 40 to 70 GeV. It is shown that a linear correction system does not provide the required chromaticity change limitation for this energy range. Due to a linear correction the chromaticity change is still 20 in the horizontal and -30 in the vertical plane. Thus a non-linear correction based on a closed loop by means of the rotating coil system is necessary. At 70 GeV a short delay is required in order to switch the power converters to higher ramp rates. During this time a small decay followed by snapback is also observed.

But unfortunately the technique of the closed loop correction system based on the rotating coil measurements is one of the most delicate procedures in the routine operation. The system contains a large number of components, which implies a high failure probability. Thus another technique of sextupole correction by use of look-up tables was designed.

The fundamental concept of the correction system based on look-up tables is the reproducibility of the behavior of the sextupole component of the magnets. This was proved during the commissioning of the HERA magnets and some years of normal operation. The parameterization of the look-up tables is given by the duration at injection. Within a single section of the ramp a sufficient number of changes in ramp-rates provides the non-linear correction of the sextupole component. The required information concerning the generation of the look-up tables is provided by sextupole measurements, which have to be made once during machine studies before the luminosity run time period. Tests have shown that one has to expect a maximum chromaticity error of ± 2.5 due to uncertainty in the reproducibility. But the average chromaticity error is only ± 0.5 . Apart from chromaticity control the look-up table technique is successfully applied to tune control as well. The effect of this tune correction method is shown Figure 2.40.

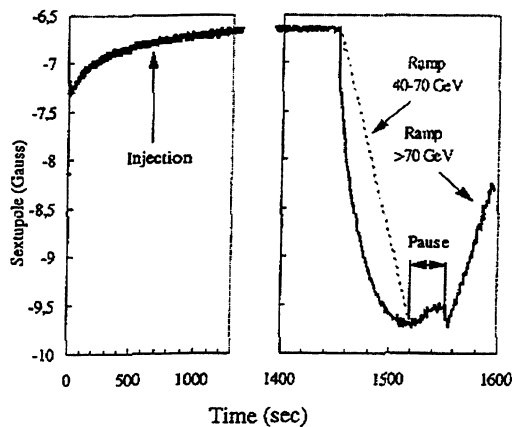


Figure 2.39: Measured sextupole field component during injection and ramp from 40 to 150 GeV. [64]

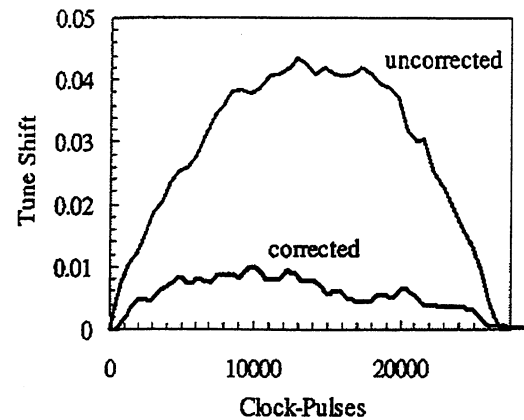


Figure 2.40: Plot of uncorrected and corrected tune shift using look-up tables for the energy range from 300 to 677 GeV. [64]

2.8. Historical studies at LHC

At LHC several dipole model magnets were tested in the previous years. All the experiments showed structurally very similar results concerning the dynamic effects, as mentioned above in case of the superconducting magnets of other projects.

The field components showed persistent current contribution along the excitation cycle, which led to a hysteresis. The integral field components decayed in time and showed significant temperature influence [59].

Spatial periodic patterns along the length axis of the magnet existed and they decayed in time. Two full-scale prototype magnets were tested by use of an array of 7 coils covering a length of 175 mm, longer than the twist pitch (110 to 120 mm) of the Rutherford type cable [61]. With the help of this set of coils the periodic pattern amplitude could be directly deduced. The results of these measurements are shown in Figure 2.41. One sees the periodic pattern amplitude between the start and the end of the low current plateau. It is obvious that periodic patterns show more pronounced amplitudes at both ends of the magnet than in the straight section. There is a symmetry between left and right end.

Apart from these qualitative observations some quantitative verifications of characteristic parameters derived from a prediction model were established. And finally the following four sources of non-uniform currents in the strands of the Rutherford-type cable, which were thought to be the source of the periodic patterns, were mentioned:

1. non-uniform contact resistance at the cable joints ;
2. non-uniform critical density J_c at high field ;
3. incomplete cable transposition with respect to self and external field change ;
4. non-uniform cable-contact resistance R_c along the length of the cable .

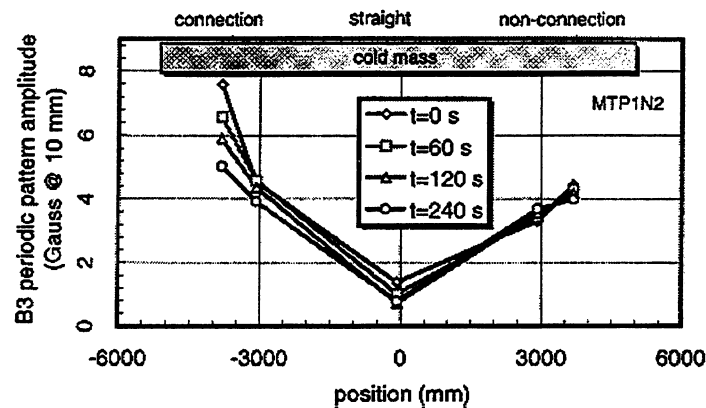


Figure 2.41: Amplitude of periodic patterns of the normal sextupole during a low current plateau at different times after the ramp-down at 20 A/s. The measurements were performed at different locations along the length of the MTP1N2 dipole. [61]

Regarding the search for procedures, which reduce the strength of decay and snapback during injection, L. Bottura reported about an interesting experiment in 1996 [60]. Based on the fact that snapback is a ΔB phenomenon rather than a change rate process the magnet excitation current during injection was increased by 20 A in 1000 seconds. The 20 mA/s slope was approximated within the resolution of the power converter by a consecutive sequence of 1 A steps during the injection period. Thus a discrete series of mini snapback was visible during injection, as shown in Figure 2.42. But one has to note that this special operation condition is very unlikely to be applied to real machine operation.

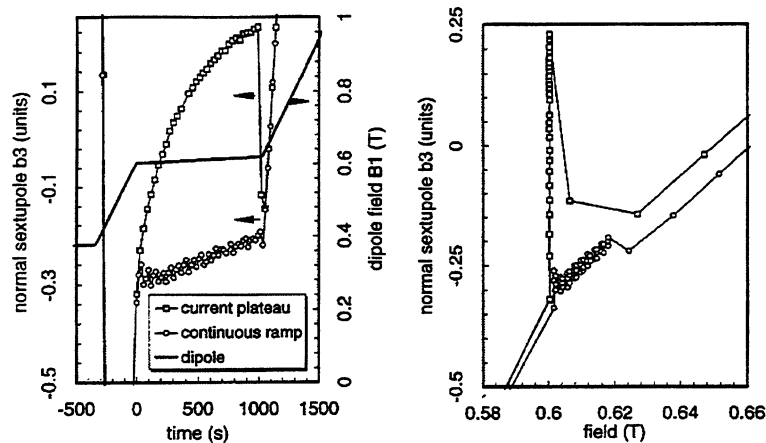


Figure 2.42: Sextupole field component of the LHC dipole magnet MTP1N2. The dipole current at injection is maintained constant in one case and changed in 1 A steps over 20 minutes, for a total of 20 A, in the other. Sextupole and dipole are plotted versus time at injection in the left plot, while sextupole for both cases is plotted versus dipole field in the right plot. [62]

Furthermore it was said that the inter-strand resistance should not exceed a lower limit of $10 \mu\Omega$ because of beam optics consideration [59]. Some other experiments cover the flat-top duration and current influence on the field component decay as well as the impact of variations in temperature on the harmonic components [60].

2.9. Conclusion of the Historical Review

Dynamic effects (decay and snapback) had a dramatic impact on the performance of all the operating accelerating storage rings, which work with superconducting magnets. It is experimentally verified that conventional flux creep considerations alone cannot sufficiently describe the phenomenon of the slow field component decay during the constant current excitation of the superconducting dipole magnets. The slow field component decay is considered to be a combination of at least two components. One component must be due to natural magnetization decay because of thermally activated flux creep, while the other component finds its origin in the electromagnetic properties of the Rutherford-type cable. Exposing such a cable to a changing magnetic field, like in the windings of a magnet, is understood to be the reason for periodic patterns. It was shown that periodic patterns behave very similarly to operation cycle variations like the integral field decay. Furthermore the decay of field components depends strongly on the operation temperature as long as periodic patterns can be neglected. Thus the second contribution to the field component decay could be the decay of periodic patterns. Concerning the machine operation the strong non-linear dependence of the field component decay on the recent machine operation history is one of the most unpredictable factors of a proper correction system. This system should provide a certain beam parameter quality in order to perform collision experiments with the design luminosity. Thus online measurements on reference magnets, look-up tables, and / or operator interventions are today's commonly used operation scenarios.

In order to complete the historical review we present the operation current respectively the field dynamics of the main bending magnets and the energy range of the accelerators, which have been mentioned in this chapter. The parameter r_0 is the reference radius to which field errors in different projects have been quoted.

Table 2.1: Some parameters of the superconducting accelerator machines, which have been mentioned in the chapter of the historical review.

	r_0	I_{inj}	I_{nom}	\dot{I}	Transfer Function	B_{inj}	B_{nom}	\dot{B}	E_{inj}	E_{nom}
	[mm]	[A]	[A]	[A/s]	[T/kA]	[T]	[T]	[T/s]	[TeV]	[TeV]
UNK	35	690	5000	100	0.989	0.69	5.11	0.1	0.4	3
SSC	10	670	6715	4	1.017	0.66	6.6	0.004	2	20
TEVATRON	25.4	666	3996	70	1	0.66	4		0.150	0.9
HERA	25	250	5027	10	1.074	0.23	4.48	0.01	0.04	0.820
LHC	10	760	11750	10	0.74	0.54	8.36	0.0074	0.45	7

3. Theoretical Models

The present understanding of the physics of decay and snapback is mainly based on the new idea of the existence of boundary induced coupling currents or supercurrents, flowing in the Rutherford-type cable over long distances and arising with long time constants in comparison to eddy currents. The source of these currents is localized in the head of the magnet where a spatial variation of the field sweep rate can be observed. These currents cause a current imbalance in the cross section of the Rutherford type cable, which leads to field component periodicity on the cable. Today we believe that the field component decay is mainly due to the decaying current imbalances in the Rutherford type cable. In addition the thermally activated flux creep, which is an intrinsic property of the superconducting phase of the Rutherford type cable also gives a non-negligible contribution.

The snapback can be understood simply as a fast re-establishing of the magnetization due to the transport current increase when the magnets are ramped to higher fields. The nominal field sweep rate is sufficient to erase the magnetization loss during constant excitation within a few seconds.

This chapter is devoted to a summary of the physical understanding. We start with flux creep, the best known of the phenomena quoted. We then prove the existence of supercurrents by means of a simple two-wire modeling and full-scale cable simulation.

3.1. Decay

The phenomenon of thermally activated flux creep was originally thought to be the only source of field component decay. Today we believe that flux creep make a non-negligible additional contribution to field component decay in superconducting LHC magnets.

3.1.1. Flux Creep in the Superconductor

Technical superconductors belong to the so-called strong pinning type-II superconductors, which are e.g. in use in the cable of the LHC magnet coils. In contrast to pure type-II superconductors strong pinning forces between the flux lines and pinning centers characterize them. In case of a transport current the pinning mechanism provides a compensation of the Lorentz force on the flux lines, which appears due to the interaction of transport current and flux lines. Without any compensation the Lorentz force would establish flux flow and consequently energy dissipation would arise. A sketch of flux line penetration into a type-II superconductor due to an external field $\mu_0 H$ and the effect of the transport current on the flux line structure is shown in Figure 3.1 [72, 73, 74].

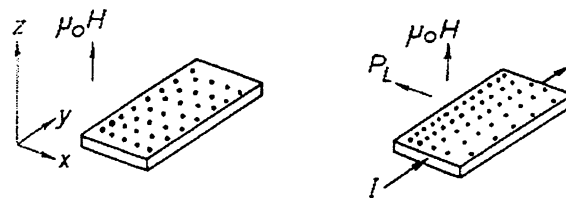


Figure 3.1: Schematic configuration of a superconductor in the mixed state, which is exposed to a magnetic field without any transport current (left) respectively with transport current (right). [72]

The equilibrium between pinning and Lorentz forces can be defined with:

$$\vec{F}_L = \vec{j}_c \times \vec{B} = -\vec{F}_v. \quad (3.1)$$

Here \vec{F}_L is the Lorentz-force density per unit volume and \vec{F}_v is the pinning force density. \vec{F}_v is a property of the superconductor and depends on B and T.

$$F_v = F_v(B, T) \quad (3.2)$$

According to the force equilibrium (Equation 3.1) between the Lorentz-force and pinning force, this leads to:

$$j_c = \frac{F_v(B, T)}{B} \quad (3.3)$$

Pinning forces are provided by inhomogenities in the crystal structure of the superconductor, which lead to pinning centers for the flux lines. Energetically seen these pinning centers establish pinning potentials where flux lines are caught. The depth of the potential wells can be significantly reduced in the presence of any additional force, which introduces a gradient of the potential. The effect of pinning centers on flux lines and the energetic considerations are schematically shown in Figure 3.2.

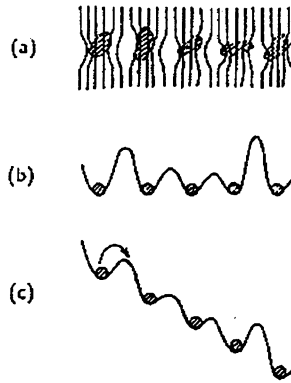


Figure 3.2: Schematic visualization of the flux creep problem. a) Attracting effect of the pinning centers on the flux-lines. b) Flux-lines and pinning potentials without any external force. c) Reduction of the pinning potentials due to the potential of the Lorentz force in the presence of a transport current. [52]

The energy barriers in this potential valley model are characterized by the reduced diffusion activation energy U_p . Without any reducing effects we can define a hopping rate which is proportional to $\exp(-U_p/k_B T)$. A so-called hopping rate can be defined by multiplying the exponential with r_0 , which is some characteristic oscillation frequency of the flux-line in its potential ($\sim 10^{10}$ Hz).

The Lorentz-force diminishes the effective pinning force by establishing a gradient in the potential structure. This effectively increases the hopping rate of flux lines. The hopping rate is also a function of the temperature. Thus in total the flux creep rate must depend on the temperature and the external field or transport current variations.

It can be shown [73] that the critical current is time dependent. For long time observations the $j_c(t)$ dependence can be written in the form:

$$j_c(t) = j_c(t=0) \left(1 - \frac{k_B T}{U_p} \ln t \right). \quad (3.4)$$

This clearly shows that the critical state is not a stationary state. The superconducting system tends to relax in the thermodynamically equilibrium state where $B = \text{constant}$ is valid.

The starting point of modeling the magnetization due to persistent currents of a cylindrical superconducting filament is the existence of shielding currents, which tend to keep the interior of the filament free of flux. In accordance with Bean's model of the critical state the current density of the shielding current is given by j_c . The magnetization of a fully penetrated strand is:

$$M = \frac{2\mu_0}{3\pi} \lambda j_c d$$

where d is the diameter of a cylindrical filament. In this notation j_c is the field dependent critical current density [62]. As assumed above j_c decays logarithmically in time and is temperature sensitive. The parameter λ is the ratio of the superconductor in the strand cross section, because of the magnetization to the unitary volume of the cable.

The magnetization of the strands respectively filaments in the cable of the magnet's coil contribute to the total field in the magnet's aperture. Hence the persistent current sextupole component of the dipole field will also show a logarithmic dependence on time and a certain temperature sensitivity.

3.1.2. Unbalanced currents in the Rutherford type cable

3.1.2.1. Existence of Unbalanced Currents

The theoretical framework, which describes the field component decay and periodicity, is mostly based on the idea of R. Stiening [51]. According to him, any change of current distribution in the cable is associated with a periodic variation of the local magnetic field along the cable. Later publications further expand his idea of the current distribution and redistribution in the Rutherford type cable. These theoretical activities provide the physical background of our present understanding of the field component periodicity, decay and snapback. [75, 76, 77]

3.1.2.1.1. Two-wire cable

A good starting point is the analytical treatment to establish the existence of current imbalance in a twisted two-strand model of the Rutherford-type cable. [77, 78, 79, 80]

The modeling of the two-wire configuration is shown in Figure 3.3. The wire is defined by a sequence of several inductive and resistive elements. The resistive elements of the wire are geometrically located at the crossing points of the two cables. L_0 is the inductance of a half twist pitch length l . It can be approximated by $L_0 = (\mu_0/\pi)[\ln(b/d) + 1/4]l/2$, where b is the width of the cable and d is the wire diameter. The ideal two-strand model in its continuum model approximation is given by a uniform and distributed transverse conductance $G' = 2/(R_c l)$ and inductance $L' = 2L_0/l$ per unitary length. The cable is exposed to a sharp spatial variation of the field sweep rate in only one single loop of its twisted structure. The driving voltage in the loop is

$$U(t) = \int \dot{B}(t) ds. \quad (3.5)$$

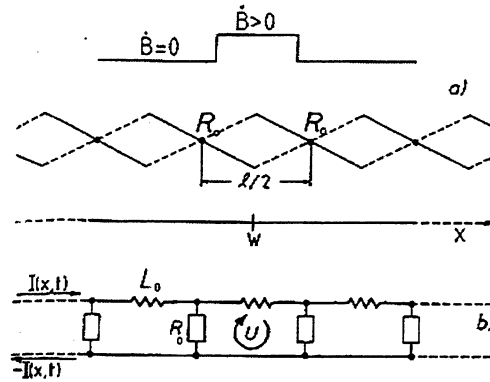


Figure 3.3: Geometry of the two-wire cable model. \vec{B} is perpendicular to the paper plane and applies only in one single loop of the two-wire model. [78]

It can be shown that the current in each strand satisfies the current diffusion equation (Equation 3.6) with a diffusivity coefficient (Equation 3.7).

$$\frac{\partial^2 I}{\partial x^2} = L' G' \frac{\partial I}{\partial t} \quad (3.6)$$

$$D = (L' G')^{-1} \quad (3.7)$$

The space and time dependent solution of the problem is

$$I(x,t) = \sum_{k=1}^{\infty} b_k \cdot \sin(\pi k x / L) \cdot (1 - e^{-t/\tau_k}) \quad (3.8)$$

with $k=1, 3, 5, \dots$ and with a time constant. The variable L is the total cable length.

$$\tau = \pi^{-2} L' G' L^2 \quad \text{and} \quad \tau_k = \tau / k^2. \quad (3.9)$$

The coefficients b_k are functions of the shape of the steady state supercurrents.

$$b_k = (-1)^{(k-1)/2} 8 I_m / (\pi^2 k^2) \quad (3.10)$$

The maximum steady state supercurrent appears at the position of the loop. The value is given by Equation 3.11.

$$I_m = U / (2R) \quad (3.11)$$

where R is the contact resistance of half of the cable length.

The decisive factor of this theory is the quadratic length dependence of the time constant τ . It is remarkable that this theory describes precisely the experimental observations of the temporal supercurrent behavior for the two-wire model, where the length was stepwise reduced. Measuring the local magnetic field variation in this loop by a Hall probe experimentally verifies this theory. It proves that a simple theoretical model can fit

unbalanced currents, which are induced for quite complex \dot{B} powering conditions. The basic model configuration and the measurement results are shown in Figure 3.4 and Figure 3.5. Based on the good agreement between modeling and experimental verification we believe that this modeling provides a good hint for the parameterization of the temporal field component decay in superconducting magnets made of the Rutherford-type cable by use of a single exponential function or a composition of at least two exponential functions.

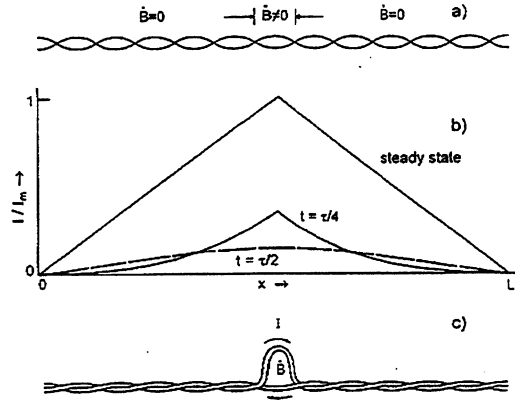


Figure 3.4: a) Experimental set up of the two-wire current diffusion model. b) Steady state current distribution and some other charging situations. c) Experimental realization of the single current loop. [80]

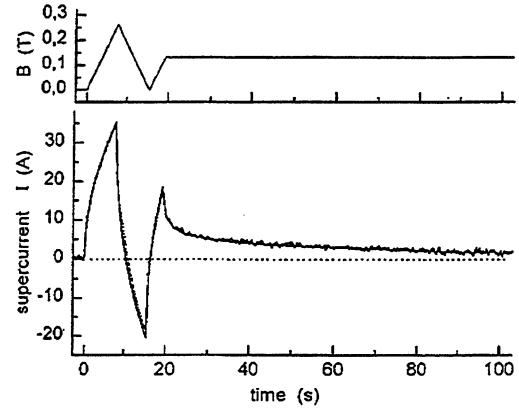


Figure 3.5: Field ramp of the background coil and measured signal of current distribution. [80]

3.1.2.1.2. Multi-strand cable

In contrast to the analytical solution of the steady state current diffusion problem, numerical simulations of the full scale Rutherford-type cable accurately deal with the geometry in addition to the arbitrary distribution and magnitude of the sources $\Delta\dot{B}_\perp$. The parameter $\Delta\dot{B}_\perp$ is the spatial variation of the time derivative of the field component normal to the broad face of the cable. Based on results of the numerical studies, A.P. Verweij derived the current imbalance ΔI of the long-range currents caused by a spatially localized variation of the field change rate. This variation typically appears at the end of the magnet, where the cable bends around the beam pipe. [16, 76]

If the characteristic (=diffusion) length ξ_D is significantly smaller than the cable length, the current imbalance ΔI in a strand is

$$\Delta I \approx 0.88 \frac{w \xi_D}{R_c} \left(1 - e^{-\frac{N}{9.6}} \right) \Delta\dot{B}_\perp \quad (3.12)$$

and the diffusion length of the current imbalance along the cable is

$$\xi_D \approx 0.5 \sqrt{\frac{R_c L_p \pi d^2}{2 \rho N}} \quad (3.13)$$

where ρ is the effective strand resistance that is used in the model to present the longitudinal electric field associated to the current flow in or out of the superconducting filament. This parameter is usually in the range of 10^{-14} Ohm. The parameter w is the width of the cable, which is characterized by a uniform interstrand resistance R_c . The cable consists of N strands with the strand diameter d .

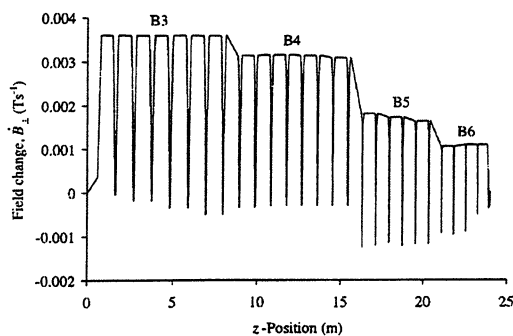


Figure 3.6: Typical field change along the length of the cable of the inner coil of a 1 m long LHC dipole model magnet with a 50 mm aperture. [76]

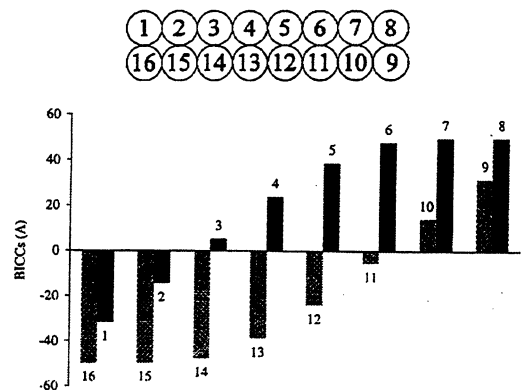


Figure 3.7: Illustration of the magnitude of the BICCs in a 16-strand cable at a certain z-position. The labels indicate the strand position. [76]

3.1.2.2. Unbalanced Currents and Magnetization Decay

After establishing the existence of unbalanced currents in the Rutherford-type cable, which are induced during ramps of the excitation cycle of the magnet, we have to deal with the decay of the field components during the constant current excitation because of the redistribution of unbalanced currents.

At the start of injection the filaments in the strand are left in a fully magnetized state determined by the previous change of the main field in the magnet coils. We believe that the following decay of the field components in the LHC dipole magnets during injection porch is caused by the change of the initial filament magnetization due to the current redistribution among the strands of the cable [20, 60]. Two mechanisms, which lead to a strand magnetization decrease, have been identified: strand *self-field* effect and the *external-field* change. The external-field change is a cumulative effect from all strands in the cable and the neighboring turns. Thus the total change of field during the constant excitation of the magnet can be defined as:

$$\Delta B_{tot}(t) = \Delta B_{ext}(t) + \Delta B_{self}(t) \quad (3.14)$$

The magnetization change due to the self-field effect for one strand is always negative, because the transport current change tends to wipe out the magnetization of the outer shell of the strand. As each strand is twisted in the cable, the average magnetization change over the cable volume can be calculated from the average change of the strand transport current density:

$$\Delta M_{self} = -\frac{2\mu_0}{3}\eta d|\Delta J|_{avg} \quad (3.15)$$

where η is the ratio of the strands cross-section to the cable cross-section.

In addition, each strand sees a changing external field, which rotates along the cable period equal to the cable twist pitch L_p , similar to what is measured as field periodicity along the length axis of the magnet's aperture. The direction of the field change is therefore not necessarily parallel to the initial magnetic moment \mathbf{M} of the filament. Thus the magnetic moment must be treated as parallel $M_{||}$ and perpendicular M_{\perp} , in respect to the direction of the dipole's main field. But it is proved that M_{\perp} varies periodically over a cable twist pitch so that there is no contribution to the field integral over the magnet. Therefore it is not necessary to take M_{\perp} into account for field error calculations.

The oscillating external field increases over approximately one half of the twist pitch and decreases over the other half. For field increases the magnetization remains on the same branch of the hysteresis loop. In this regime an increasing field causes only a little change in the magnetization. On the other hand, for a field decrease a new penetration layer is formed with reversed shielding currents, causing a large change of the magnetization. In sum, the magnetization is lowered over approximately half a cable pitch, while it changes little over the other half. For small field changes ($\ll J_c d$) the change of the original magnetization is defined as:

$$\Delta M_{ext} = -\frac{\lambda}{2}|\Delta B|_{avg} \left[1 - \frac{|\Delta J|_{avg}}{J_c} \right] \quad (3.16)$$

where λ is the ratio of the filament cross-section to the cable cross-section.

In conclusion, on average the magnetization decays during a current plateau. For small changes compared to the critical current, the total change of M is:

$$\Delta M_{||} \approx -\frac{\lambda}{2}|\Delta B|_{avg} - \frac{2\mu_0}{3}\eta d|\Delta J|_{avg} \quad (3.17)$$

Figure 3.8 shows different cycles of a typical magnetization curve of a strand, differing only by a different minimum cycle field. Increasing or decreasing the external field by ± 20 mT leads to quite different changes of the initial magnetization.

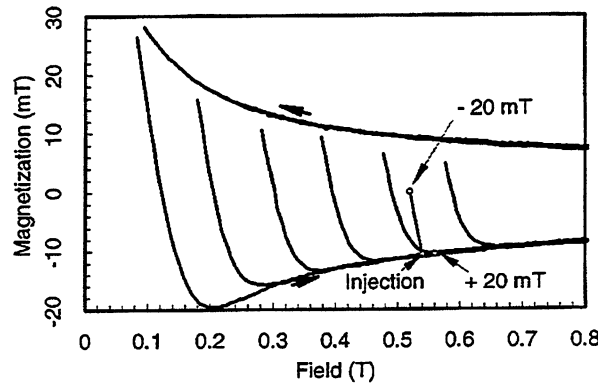


Figure 3.8: Typical magnetization curve of a strand. Also shown is the change of magnetization due to a field change of ± 20 mT. [20]

3.2. Snapback

After constant excitation at the beginning of the ramp upward to higher fields the magnetization of the filament respectively strands is reestablished within a field increase of approximately 20 mT. This change in field is due to the main current increase in the cable of the magnet's coil. This explains why the missing magnetization during the constant excitation is immediately regained after starting the ramp [20, 60]. Typical magnetization parameters at injection in case of the LHC are given in Table 3.1.

Table 3.1: Typical values of important magnetization parameters near LHC injection ($T=1.9K$, $B=0.54T$, filament diameter $d=6\mu m$). [20]

Parameter	Typical value	
Magnetization of filament	35	mT
Magnetization of strand	12	mT
ΔB , which is required to go from one branch of the hysteresis to the other	100	mT
Change of magnetization of a filament for a 10 mT field rise	-0.35	mT
Change of magnetization of a filament for a 10 mT field decrease	-20	mT
Typical critical current density λJ_c of strand	$7 \cdot 10^9$	A/m ²

3.3. Conclusion

The combination of the elements of the theoretical framework indeed explains the systematic drift of the allowed multipoles. The internal field change necessary to explain the observed drift of the harmonics is small, in the range of 10 mT. Such a field change can be generated in a typical Rutherford type cable for accelerators by a current redistribution among the strands of some 10 Amperes. This is a value, which is coherent with the expected current imbalance, e.g. generated by the local field variations discussed in the previous section.

As shown in this chapter we can provide several physical phenomena, which are responsible for the observed effects. But a closed formalism, which for example describes the induction of current imbalances and matches it with field periodicity, field component decay respectively magnetization loss does not yet exist.

4.1.2. Complex Formalism for 2D Magnetic Field

In the body of a dipole far from the magnet ends the conductors can be considered as rectilinear and parallel to the beam orbit. Let us built up an orthogonal reference frame where O designates an origin. The vector \vec{z} designates a direction parallel to the conductor and x and y are the coordinates in a perpendicular surface. The current flows parallel to the z direction and is described by a current density vector $\vec{J} = J_z(x, y)\vec{z}$, where $J_z(x, y) \neq 0$ inside the conductor, and $J_z(x, y) = 0$ everywhere else. According to Maxwell-Ampere's law, $\vec{\nabla} \times \vec{H} = \vec{J}$, a two dimensional magnetic field, uniform in \vec{z} , is generated by $J_z(x, y)$.

$$\vec{H} = H_x(x, y)\vec{x} + H_y(x, y)\vec{y} \quad (4.1)$$

where

$$\frac{\partial H_y(x, y)}{\partial x} - \frac{\partial H_x(x, y)}{\partial y} = J_z(x, y). \quad (4.2)$$

In free space (inside the aperture of the magnet) the magnetic flux density, \vec{B} , is given by $\vec{B} = \mu_0 \vec{H}$, where $\mu_0 = 4\pi 10^{-7} \text{H/m}$ is the permeability of vacuum. In free space Equation 4.2 becomes

$$\frac{\partial B_y(x, y)}{\partial x} = \frac{\partial B_x(x, y)}{\partial y}, \quad (4.3)$$

and from Maxwell-Gauss equation we derive

$$\frac{\partial B_y(x, y)}{\partial y} = -\frac{\partial B_x(x, y)}{\partial x}. \quad (4.4)$$

Equation 4.3 and 4.4 are the Cauchy-Riemann conditions for a function $f(s) = u(x, y) + iv(x, y)$ of a complex variable $s = x + iy$. Thus we introduce the complex magnetic flux density $B = B_y + iB_x$. In all regions without current, \vec{B} is a continuous, single-value, and differentiable function of the complex variable \bar{s} . Hence it can be considered as a regular (or holomorphic), analytic function. A function of this type can be expressed by a power series expansion in a region G of the complex plane where it is analytical. This region, by virtue of the properties discussed above, is coincident with the aperture of the magnet. Thus we define a radius R_d being the maximum radius of the aperture and establish the Taylor series around the origin of the aperture for s , $|s| < R_d$:

$$B(s) = \sum_{n=0}^{\infty} B^{(n)}(O) \frac{s^n}{n!}. \quad (4.5)$$

where $B^{(n)}$ is the n^{th} derivative of B with respect to s . In Europe it is customary to re-write Equation 4.5 in the form

$$\mathbf{B}(s) = \sum_{n=1}^{\infty} (B_n + iA_n) \left(\frac{s}{R_{ref}} \right)^{n-1} \quad (4.6)$$

where the index n is shifted by 1. Here, A_n and B_n , the skew and normal absolute multipole coefficients, are related to $\mathbf{B}^{(n-1)}(O)$ for $n, n \geq 1$, by

$$B_n + iA_n = \frac{\mathbf{B}^{(n-1)}(O)}{(n-1)!} R_{ref}^{n-1} \quad (4.7)$$

The reference radius R_{ref} is free in choice. A change of the reference radius will change the multipole coefficients according to

$$B'_n + iA'_n = \left(\frac{R'_{ref}}{R_{ref}} \right)^{n-1} (B_n + iA_n). \quad (4.8)$$

In contrast to the magnetic flux density, which is invariant against coordinate transformation, $\mathbf{B}(s) = \mathbf{B}'(s')$, we derive the harmonic coefficients due to a translation of the reference frame by

$$B'_n + iA'_n = \sum_{k=n}^{\infty} (B_k + iA_k) \binom{k-1}{n-1} \left(\frac{\Delta x + i\Delta y}{R_{ref}} \right)^{k-n} \quad (4.9)$$

The parameters Δx and Δy are the x and y displacement coordinates between the origins of the reference frames. This displacement can be written as $\bar{s} = \bar{s}' + \Delta x + i\Delta y$. B_n and A_n are the original harmonics (x, y -system) and B'_n and A'_n are the transformed harmonics in the translated system (x', y' -system).

If the reference frame is rotated by an angle θ , the harmonics in the original system (x, y) transform into the translated system (x', y') according to:

$$B'_n + iA'_n = (B_n + iA_n) e^{in\theta} \quad (4.10)$$

Since the dipole field is expected to be 10^4 times larger than the multipole coefficients it is customary to introduce the dimensionless multipole coefficients, a_n and b_n , defined as

$$b_n + ia_n = 10^4 \frac{B_n + iA_n}{B_1} \quad (4.11)$$

The above representation of the magnetic flux density by a series expansion is customary to deal with all issues regarding the field quality of superconducting magnets in the accelerator community.

4.1.3. Magnetic Flux through a Surface

We consider a surface, Σ , which is parallel to the z -axis and forms an arc Γ at the intersection with the xy -plane. The two outer most extremities of Γ are designated by \bar{s}_1 and \bar{s}_2 in the xy -plane.

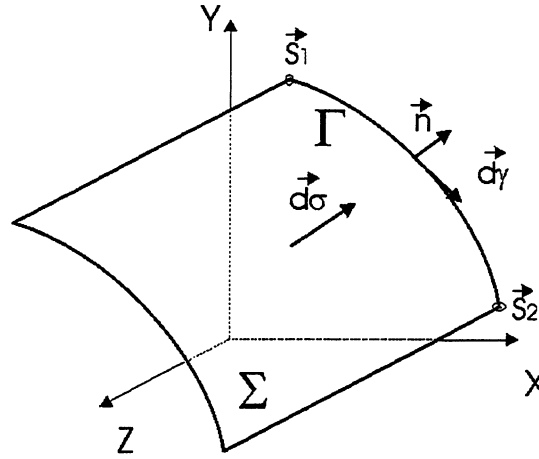


Figure 4.2: Magnetic flux through a surface, which is parallel to the z -axis. The outer most extremities in the xy -plane are determined by \bar{s}_1 and \bar{s}_2 .

The magnetic flux through the surface is given by

$$\Phi = \iint_{\Sigma} \vec{B} \cdot d\vec{\sigma} \quad (4.12)$$

where $d\vec{\sigma}$ is a surface element vector. Because of the special geometry $d\vec{\sigma}$ can be expressed as $d\vec{\sigma} = L(\vec{e}_z \times d\vec{\gamma})$. Here $d\vec{\gamma}$ is the arc element vector, which is given by the coordinates $(-dy, dx, 0)$. Hence the flux through the surface becomes

$$\Phi = L \sum_{\Gamma} (-B_x dy + B_y dx), \quad (4.13)$$

which can be written as

$$\Phi = L \operatorname{Re} \left[\int_{\Gamma} ((B_y + iB_x)(dx + idy)) \right]. \quad (4.14)$$

Using the definition of the complex magnetic flux density $B(s)$ and the complex variable s we can write Equation 4.14

$$\Phi = L \operatorname{Re} \left[\int_{s_1}^{s_2} B(s) ds \right]. \quad (4.15)$$

Replacing $B(s)$ by its power expansion and performing the integration finally leads to

$$\Phi = \operatorname{Re} \left[\sum_{n=1}^{\infty} K_n (B_n + iA_n) \right] \quad (4.16)$$

where K_n is the complex *sensitivity factor of order n* , which is given as:

$$K_n = \frac{LR_{ref}}{n} \left(\frac{s_2^n - s_1^n}{R_{ref}^n} \right) \quad (4.17)$$

4.1.4. Magnetic Flux picked up by a Rotating Coil

Let Σ be the average surface of a turn of a N -turn pick up coil rotating around the z -axis. The angle θ reckons the coil rotation with respect to a zero mark. For $\theta \neq 0$ the vectors $s_1 = s_{1,0} e^{i\theta}$ and $s_2 = s_{2,0} e^{i\theta}$ designate the position of the two extremities of the arc Γ in respect to the reference values $s_{1,0}$ and $s_{2,0}$ for $\theta = 0$. Substituting this in Equation 4.16 and 4.17 we derive

$$\Phi = \text{Re} \left[\sum_{n=1}^{\infty} K_n (B_n + iA_n) e^{in\theta} \right] \quad (4.18)$$

where

$$K_n = \frac{NLR_{\text{ref}}}{n} \left(\frac{s_{2,0}^n - s_{1,0}^n}{R_{\text{ref}}^n} \right). \quad (4.19)$$

The *sensitivity factor of the order n* of the *rotating pick-up coil* can be real or complex. Thus different multipoles of the magnetic field are seen with different sensitivities. The geometric design parameters of the coil and the choice of the reference radius determine these sensitivities.

In case of an array of pick-up coils the sensitivity is given by the superposition of the sensitivity factors of the coils. Thus the total *sensitivity of order n* of the coil array, K_n^{tot} , is given by

$$K_n^{\text{tot}} = \sum_{p=1}^P \varepsilon_p K_n^p. \quad (4.20)$$

Here K_n^p is the sensitivity factor of order n of the p^{th} coil. According to the polarity of the electrical connection of the coils, the parameter ε_p is either $+1$ if the p^{th} coil is connected in series, or -1 if the p^{th} coil is connected with opposite polarity.

4.1.5. Voltage induced in a Rotating Pick-up Coil

When the N -turn pick-up coil rotates with an angular velocity ω , the angle θ can be computed for any given time t as $\theta = \omega t + \theta_0$, where θ_0 is the coil angle at $t = 0$. According to Faraday's law, the voltage, V , induced in the coil during the rotation is

$$V = -d\Phi/dt = -\omega \text{Re} \left[\sum_{n=1}^{\infty} in K_n (B_n + iA_n) e^{in(\omega t + \theta_0)} \right]. \quad (4.21)$$

A single coil is insufficient to measure the small multipole field components of high order (b_3, b_5, b_7, b_9) in the presence of the large dipole background field. This is the reason for using a configuration of two coils with equal width and equal number of turns connected electrically in series with opposite polarity. The dipole contribution to the "compensated signal" $V_{\text{comp}} = V_A - V_B$ vanishes. The dipole field, "absolute signal" is derived from V_A only.

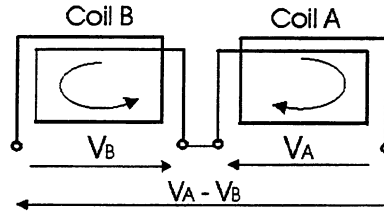


Figure 4.3: Connection diagram for *absolute* (V_A) and *compensated* ($V_A - V_B$) magnetic measurements.

The sensitivity factor of order n for this two-coil array is given by

$$K_n = \frac{1}{n} \left(\left(\frac{R_2}{R_{ref}} \right)^n - \left(\frac{R_1}{R_{ref}} \right)^n - \left(\frac{R_4}{R_{ref}} \right)^n - \left(-\frac{R_3}{R_{ref}} \right)^n \right) \quad (4.22)$$

The geometry of the two-coil array, which is in use for the dipole field quality studies is shown in Figure 4.1.

4.1.6. Signal Processing

The signals obtained from the rotating coil array are split in accordance to the electrical connections in a *compensated* and *absolute* signal. During a rotation of 2π of the rotating coil system the signals are sampled as a function of the angle θ_k in a discrete series of k points for a total of M points uniformly distributed over one turn. We obtain the flux increments between two angular positions by integrating the measured voltage from the rotating coil.

$$\Delta\Phi_i = \int_{\theta_i}^{\theta_{i+1}} V dt \quad (4.23)$$

From this we finally obtain the magnetic flux Φ_k as sum over the flux increments $\Delta\Phi_i$. In order to derive the harmonic field coefficients we pass the flux increments to a discrete Fourier transformation (DFT). We then derive the transformed flux (in frequency domain) $\underline{\Phi}_k$, as

$$\underline{\Phi}_k = \sum_{k=1}^M \Phi_k e^{-2\pi i(k-1)\frac{n-1}{M}} \quad (4.24)$$

where $n = 1 \dots M$. Here M is the maximum number of harmonics, which is of interest. It can be shown that the relation between the DFT coefficients and the harmonic coefficients for an even number of points M is given by

$$C_n = B_n + iA_n \approx \frac{2}{M K_n} \underline{\Phi}_k \quad (4.25)$$

with $n = 1 \dots M/2$. The M flux values give M complex Fourier coefficients, but only the coefficients in the range 1 to 15 are retained. The real part of the Fourier coefficients is

proportional to the normal field harmonics and the imaginary part is proportional to the skew harmonics. The component with $n = 1$ is the dipole.

4.2. The Magnet Test Facilities

The magnetic measurements at LHC-MTA were performed in two different measurement stations. Both stations were located on the French CERN site. One measurement station, referred to here as *Block4*, was designed to analyze the field quality of one-meter long LHC dipole model magnets. The second test station dealt with 10-meter long LHC dipole model magnets and 15 meter long LHC prototype magnets and is referred to as SM18. The SM18 hall will host the measurement stations for future pre-series and series measurements.

4.2.1. The Long LHC Dipole Model Test Facility (SM18)

SM18 is equipped with a horizontal measurement bench, a so-called *Chaconsa bench*. The measurement bench provides the fundament on which 10-meter long LHC dipole prototypes are aligned with high mechanical precision. The dipole magnet occupies half of the bench while the other half is equipped with a support system for the rotating coil. The outer most part of the dipole magnet is connected to *the cryogenic feed box*. Here the current leads for the dipole coil are connected to the cables of the power supply. Furthermore the cold mass is provided with liquid helium through this box. The cryostat of the magnet is connected with an anti-cryostat, which is inserted in the aperture. This allows magnetic measurements at room temperature in SM18.

The rotating coil in SM18 is a single segment coil of 750 mm length and 50 turns. It is the last piece of several interconnected round ceramic parts, which are assembled in order to form a 12 meter long *measurement shaft*. The coil signals are passed from one part of the assembly to the other by electrical connectors.

The whole measurement shaft is hosted outside, in front of the magnet's aperture and is supported against bending by a vertically split pipe. Furthermore the pipe is cut in longitudinal pieces corresponding to the length of the single shaft pieces.

The horizontal and vertical partitioning of the support pipe allows a sequential horizontal opening or closing of the support pipe when the measurement shaft is pushed in or pulled out of the magnet's aperture. This longitudinal movement is performed by a stepper motor, which drives the so-called *rotating unit* along the Chaconsa bench.

The rotating unit consists of a stepper motor for azimuthal rotation of the measurement coil. The motor is equipped with an angular encoder. The measurement signals from the rotating coil unit and the angular encoder are passed to the data acquisition system for integration of the flux increments as explained in the previous section.

The voltage from each coil group is sent to a VME-Bus integrator. Consecutive to additional amplification the voltage is then converted into frequency. The pulses from the voltage to frequency converter are counted. These counts represent the integration in time, which is determined by the trigger pulse of the angular decoder. A measurement is defined as a complete forward and backward rotation. The interval of $[0...2\pi]$ is equally spaced by N sampling points. This finally leads to the flux increment Ψ_k per rotating angle segment between two trigger pulses. This flux increment is available at the output of the VME-Bus integrator. The averaging over forward and backward rotation cancels the first order field change effects during measurements (suitable for on-the-fly

measurements), first order electronic drift in the integrator, systematic offset in the angular encoder and symmetric torsion effects. In order to derive the harmonic coefficients the flux values from absolute and compensated signal are passed to a digital Fourier transformation (DFT).

A workstation in SM18 performs the DFT and data acquisition. Furthermore it controls the positioning of the rotating coil unit and the magnet current power converter. A schematic drawing of the measurement equipment in SM18 is shown in Figure 4.4.

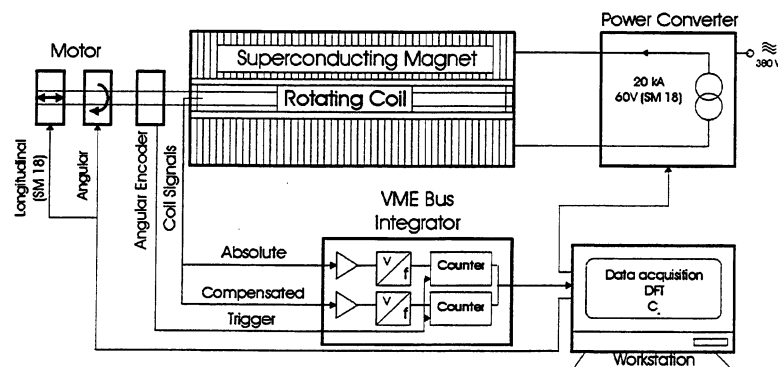


Figure 4.4: Schematic drawing of the experimental set-up and principal signal flow.

4.2.2. The Short LHC Dipole Model Test Facility (Block4)

The Short LHC Dipole Model Test Facility, Block 4, is designed to perform tests on one-meter long LHC dipole model magnets. The short model magnet is installed in a vertical cryostat and the rotating coil is inserted in the magnet's aperture from above.

The magnet's cryostat is filled with helium at atmosphere pressure (1 bar). The cryostat is divided in two portions by a λ -plate providing the separation between the saturated, 1-bar, normal helium bath above the plate and the sub-cooled superfluid state below the plate. The sub-cooled superfluid state in the lower portion of the dewar is achieved by means of a heat exchanger, where saturated superfluid helium conditions are obtained via Joule-Thomson expansion of liquid helium from 1 bar down to approximately 15 mbar. The λ -plate has a number of leak-tight penetrations for superconducting bus-bars, instrumentation wires and a sliding bearing for the rotating shaft for magnetic measurements.

The principle of the measurement technique is given in analogy to SM18 by the rotating coil device. But in contrast to the single element coil in SM18, the coil in Block 4 is segmented longitudinally. These segments allow the studying of the longitudinal field quality of the one-meter long model magnets within one single measurement run, while longitudinal scans of the field quality require a re-positioning of the single coil in SM18. The measurement shaft in Block 4 covers the central part of the magnet with three 20 mm long coils, while two outer coils have a length of 24 mm each and cover the magnet's ends. The rotating coil in Block4 is driven by a DC-motor with a typical rotation frequency of 1 Hz. An angular encoder is connected to the shaft. It determines the angular increments, required for the DFT, as described above. The system control and data processing respectively data acquisitions are performed by a workstation running a LabView virtual instrument application.

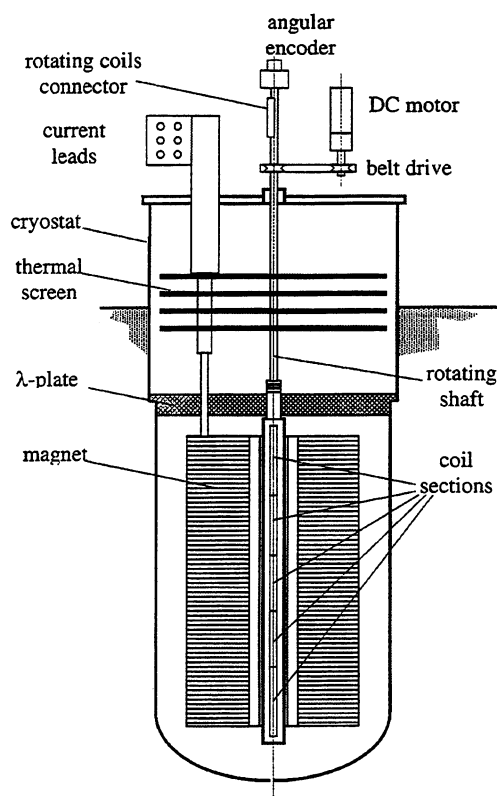


Figure 4.5: The one-meter long LHC dipole model magnet inserted in the cryostat and in Block4. [71]

4.2.3. Temperature and Current Stability

Due to our excursus of the historical aspects of dynamic effect studies we know that temperature and current stability are important for measurements of dynamic effects. The stability of these parameters is of great importance for the reproducibility of test conditions during the experiments. The test environment described above provides temperature stability to a level of ± 0.03 K. For the power supply with a maximum current of 12 kA we have an accuracy of 6 ppm of the full range (20 kA).

4.3. The LHC dipole model test program

In the next chapter we will discuss results of the magnetic measurements on the dipole models and prototypes built in the R&D program for the LHC. Magnets were produced either in full length (10 and 15 meter) to demonstrate feasibility, or in short length (1 m) to parametrically study manufacturing features with a fast turn-over.

The short dipole model test program [65, 66] at LHC, launched mid-1995, allows convenient studies of different design and assembly options on 1 m long LHC dipole magnets. The test program covers single (labeled *MBSMS*) and twin (labeled *MBSMT*) aperture magnets. The structures of the cross-section and the longitudinal section of the magnet are shown in Figure 4.6 and Figure 4.7 respectively. The key features of the design are reported in Table 4.1. Each magnet was equipped with a certain instrumentation for the standard test. The assembly contained voltage taps, in total 50 per

model, for *quench detection and localization*. Capacitance gauges between coils and collars were installed in order to measure *coil stress distribution*. Bullet gauges were used to measure the *longitudinal force on the end plate*, and strain gauges on the yoke laminations were used to monitor the *contact between yoke halves*.

All model magnets were designed, fabricated and tested in-house with a rate of up to one magnet per month. Often already tested models were re-worked and re-assembled, with modified parameters, which created a number of different versions for some magnets.

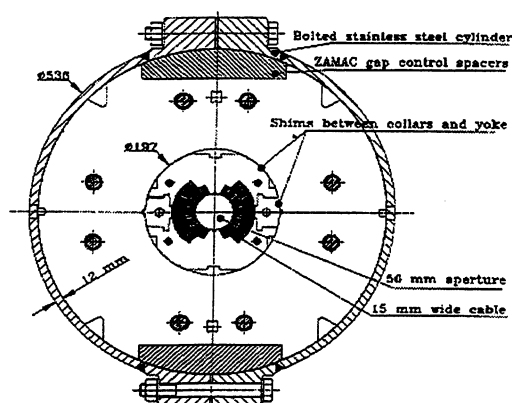


Figure 4.6: Schematic drawing of the cross section of the MBSMS type model magnet. [67]

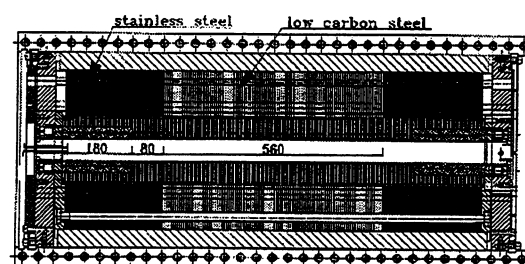


Figure 4.7: Schematic drawing of the longitudinal section of the MBSMS type model magnet. [67]

Table 4.1: Reference design features of the one-meter long LHC dipole model magnet program. [67]

Coil inner diameter	56 mm
Nominal quenching field	9.65 T @ 1.9 , 13240A
Current @ 8.4T	11500 A
Ratio peak field-central field	1.05
Overall coil length	1080 mm
Length of magnetic yoke steel	560 mm
Magnetic length	862 mm
Total inductance	3.2 mH
Magnetic forces per quadrant @ 8.4 T	$\Sigma F_x = 1650 \text{ N/mm}$ $\Sigma F_y = -820 \text{ N/mm}$
Total axial force @ 8.4 T	19 tons
Cu/Sc of inner/outer strands	1.60 / 1.90

Each model magnet underwent a sequence of tests concerning training behavior, quench localization, loss measurements, and a series of magnetic measurements. The magnetic

measurements will be dealt with in the next section. In total we analyzed magnetic measurement data on 17 one-meter long LHC model magnets. The magnets and their inter-strand resistance are listed in Table 4.2.

Table 4.2: Average inter-strand resistance in the poles and in the coil deduced from AC loss measurements on the one meter long LHC dipole model magnets. [71]

<i>Magnet</i>	<i>R_c pole 1</i> ($\mu\Omega$)	<i>R_c pole 2</i> ($\mu\Omega$)	<i>R_c average</i> ($\mu\Omega$)
MBSMS3	-	-	-
MBSMS4	3.58	4.02	3.79
MBSMS5	2.63	3.47	2.99
MBSMS6	5.74	5.32	5.52
MBSMS7	5.67	5.82	5.74
MBSMS8	6.62	6.33	6.47
MBSMS9	5.96	6.49	6.21
MBSMS10	23.75	23.75	23.75
MBSMS11	27.91	25.35	26.57
MBSMS12	11.93	11.42	11.67
MBSMS13	-	-	-
MBSMS14	not produced		-
MBSMS15	18.06	17.18	17.61
MBSMS16	-	-	-
MBSMS17	-	-	-
MBSMS18	-	-	-
MBSMT1A1	15.80	16.10	15.95
MBSMT1A2	19.70	28.10	23.16
MBSMT2A1	4.70	4.20	4.44
MBSMT2A2	9.20	7.00	7.95

Apart from short models, eleven 10-meter long and one 15-meter long dipole magnet were produced. In Table 4.3 we conclude the design features of these magnets. The design of the first five magnets (MTP...) is based on the first design concept, which is given by 50 mm aperture, 10 meter length and 17 mm cable width and six-block coil quarter cross-section. The second group of magnets (MBL1...) represents the 10-meter long LHC dipole models. They are featured by a 56 mm aperture, 15 mm cable width and five block design. The Magnet MBP1A1 is a fifteen-meter long LHC dipole prototype, which relies on equal specifications like the 10-meter long models.

Table 4.3: Conclusion of the design features for the R&D dipole magnets of the LHC.

<i>Magnet</i>	<i>Aperture</i> (mm)	<i>Blocks per coil</i> <i>quarter cross-</i> <i>section</i>	<i>cable</i> <i>width</i> (mm)	<i>length</i> (m)
MTP1A1, -A2, -A3 MTP1N1, -N2 MTP1AJ, MTP1EH	50	6	17	10
MBL1N1, -N2 MBL1AJ1, -AJ2	56	5	15	10
MBP1A1	56	5	15	15

In the introduction we already mentioned the core characteristic of the dipole magnet's cable. The reference design features of the 15-meter long LHC main bending dipole magnets are listed in Table 4.4.

Table 4.4: Reference design parameters for the 15-meter long LHC main bending dipole magnets. [10]

Current @ 8.4T	11500 A
Overall coil length	14467 mm
Magnetic length	14200 mm
Overall length of cold mass	~15000 mm
Mass of cold mass	23.8 t
Outer diameter of cryostat	914 mm
Overall mass of cryomagnet	~27.5 t
Total inductance (both channels)	108 mH
Magnetic forces per quadrant @ 8.4 T	$\Sigma F_x = 1700 \text{ N/mm}$ $\Sigma F_y = -140 \text{ N/mm}$ (inner layer) $\Sigma F_y = -600 \text{ N/mm}$ (outer layer)

We explicitly mention the electrical parameters of the cables used for the coils of the 10-meter long prototype MTP1A3 (*white book design*) and the 10-meter long model MBL1AJ2 (*yellow book design*) because they were involved in the experiments described in the next chapter. The cable's inter-strand resistances for these magnets are shown in Table 4.5. The results derived from the experiment show that short models have a similar performance and training behavior to long magnets.

Table 4.5: Average inter-strand resistance in the poles and in the coil deduced from AC loss measurements on the 10-meter long LHC prototype MTP1A3 and the 10-meter long LHC dipole model MBL1AJ2.

Magnet	$R_c \text{ pole 1}$ ($\mu\Omega$)	$R_c \text{ pole 2}$ ($\mu\Omega$)	$R_c \text{ average}$ ($\mu\Omega$)
MTP1A3 aperture. 1	14	17	15.5
MTP1A3 aperture. 2	14	14	14
MBL1AJ2 aperture. 1	1.39	1.27	1.33
MBL1AJ2 aperture. 2	1.48	1.37	1.43

4.4. From Raw Data to Results

The data we obtain from the DFT are usually stored in an ASCII file. The following data treatment depends on the measurement station from which we receive the data files. The particular differences are due to geometric differences in the type of measurement coil. This section explains how raw-data obtained from the two measurement stations are treated during the process of data analysis.

4.4.1. Analysis Tool

The R&D data of each magnet are stored on a network disk and treated locally on PC running MS-Windows 95. The decision to use MS-Excel for data treatment is mainly based on the flexibility and transparency of operations. It must be stated that pre-series

and series measurement data are treated on workstations running in-house produced C code. This is due to the fact that magnet qualification must be done with sufficient speed while the magnet is still on the measurement bench.

4.4.2. Feed Down Procedure

The sequence of data treatment processes starts with the feed down removal procedure for non-allowed multipole coefficients. This procedure is necessarily due to the off-centering between the magnetic center and the rotating coil center. The correction is necessary only for measurements from which information about non-allowed harmonics are deduced. The feed down procedure is split into two parts: a *center localization* and a *feed down correction*.

The present magnet design is optimized to provide small B_7 and B_9 . Non-allowed harmonics like (B_{10}, A_{10}) and / or (B_{12}, A_{12}) should be zero or very small in comparison to allowed harmonics like B_{11} and B_{13} . They are not allowed due to the geometry of the coil. Thus a first order approximation for dipole center location forces the non-allowed harmonics to zero.

We derive the dipole center localization with the help of the following considerations. The parameters Δx and Δy are the x and y displacement coordinates between the magnetic center of the dipole and the center of the rotating coil unit. This displacement can be written as $\bar{s} = \bar{s}' + \Delta x + i\Delta y$, where \bar{s}' is the actual reference frame in which measurements have been performed. The transformation due to coordinate translation is given by Equation 4.9. From a first order approximation with $k = n$ to $n+1$ we derive the displacement Δx and Δy as:

$$\Delta x \approx \frac{R_{ref}}{n} \frac{B'_n B'_{n+1} + A'_n A'_{n+1}}{B'^2_{n+1} + A'^2_{n+1}} \quad (4.26)$$

$$\Delta y \approx \frac{R_{ref}}{n} \frac{A'_n B'_{n+1} - B'_n A'_{n+1}}{B'^2_{n+1} + A'^2_{n+1}} \quad (4.27)$$

The index n is an even number. According to the above-mentioned multipoles we use the numbers 10 and 12. Thus all multipole coefficients with index n are the measured non-allowed harmonics, while coefficients with index $n+1$ are the normal allowed harmonics B_{11} or B_{13} respectively the skew non-allowed harmonics A_{11} or A_{13} .

The rotating coil in Block 4 consists of five coils in a longitudinal arrangement. This implies that Δx and Δy values derived for each single coil in this array must be on a line because of the mechanical installation of the coils. The quality of this correlation depends on either the results from zeroing B_{10} or B_{12} , or an average of both offsets was used as input for the feed down correction. An example of a typical center localization result is given in Figure 4.8. In Figure 4.9 we see the same results plotted in a $\Delta x \Delta y$ -scatter graph. This shows the good agreement between the expected linear correlation and the result of computation. In contrast to Block 4 the coil displacement in SM18 can only be computed for one coil.

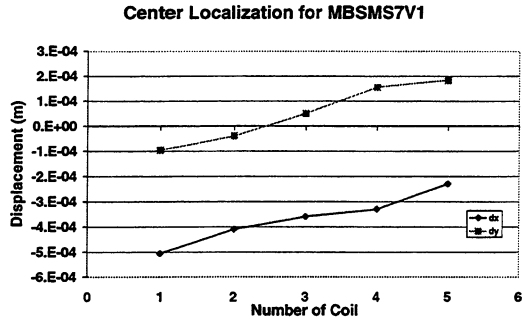


Figure 4.8: Result of center localization procedure for MBSMS7V1 in x and y direction.

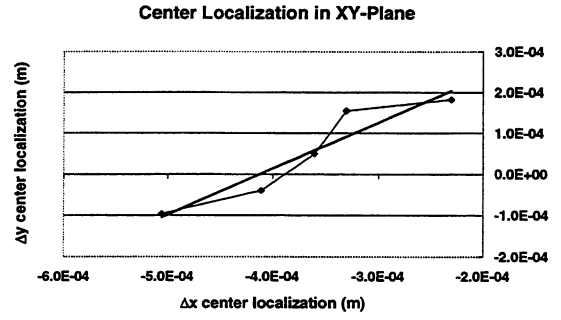


Figure 4.9: Plot of center localization in the XY-Plane for MBSMS7V1.

The displacement values are finally used to derive the feed down corrected multipoles by use of the following two equations for normal

$$B_n \approx B'_n - \frac{n}{R_{ref}} (B'_{n+1} \Delta x - A'_{n+1} \Delta y) \quad (4.28)$$

and skew

$$A_n \approx A'_n - \frac{n}{R_{ref}} (A'_{n+1} \Delta x + B'_{n+1} \Delta y) \quad (4.29)$$

non-allowed harmonics.

The feed down procedure is applied to data found at high field values because of the dominant geometric contribution in comparison to the persistent current contribution to the multipole coefficients above 6 T. Iron saturation effects can be neglected. They effect significantly only low order multipole coefficients. Furthermore the multipole coefficients have to be recalculated to a reference radius of 16 mm, which is the measurement system outer radius. Here we have the same accuracy for all orders of harmonics.

4.4.3. Integral Harmonics

Concerning the measurement technique in Block4 we have to recall that the rotating coil unit is built up by five adjacent coils of different length. In order to derive integral values of field harmonics we have to use Equation 4.30.

$$\langle b_n \rangle = \frac{\sum_{i=1}^5 b_n^i B_1^i l^i}{\sum_{i=1}^5 B_1^i l^i} \quad (4.30)$$

In this notation the index i represents the number of the coil and the length of the coils are given by l^i . In contrast to Block 4 the measured harmonics in SM18 are used without any averaging because only one measurement coil is used.

4.4.4. Periodic Pattern Effect

Figure 4.10 shows a plot of typical sextupole raw data versus time from measurements of the one meter long LHC dipole model magnet MBSMS4V1, which were performed in Block4. We see the sextupole signals measured by each of the five coils along the length of the magnet. Note that the decay and snapback is plotted with respect to the initial injection value of each coil signal. The coils are labeled L01, L23, L45, L67 and L89. This chart shows the particularity of Block4 measurements. The signals of the inner three coils shows a positive decay direction of the sextupole component, which is in accordance with the assumption of net decay of magnetization on allowed harmonics. But the outer two coils show exactly the opposite behavior. At the end of the constant excitation current phase the weight of the negative contribution becomes stronger than the weight of the positive contribution from the inner three coils. Consequently the integral decay (Figure 4.10) of sextupole tends downwards when resting for a long time at constant excitation current. Other magnets on the other hand showed a continuation of drift in positive direction because of different contributions from each coil in the five-coil array of the Block4 rotating coil measurement shaft.

Observing the snapback at the initial ramp to higher operation current reveals another interesting effect. The snapback measured with each of the coils appears to be equal and independent from the extent of the individual decay. The integral value showed an undershooting of the zero value for magnets with turn around decay behavior, while magnets with continuing decay showed a certain overshooting of the zero value. Over the whole population of tested magnets we observed a random distribution of overshooting and undershooting of the snapback phase.

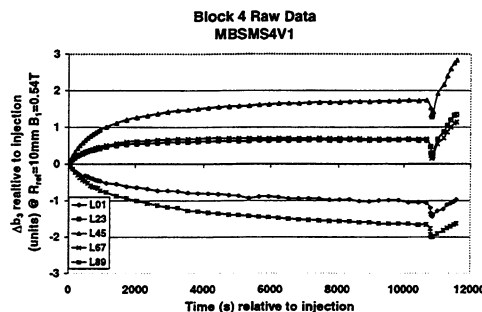


Figure 4.10: Sextupole decay and snapback measured by each coil of the Block4 longitudinal five-coil array.

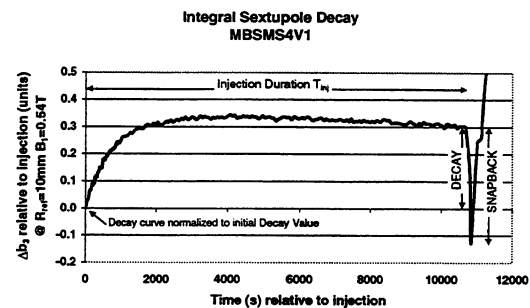


Figure 4.11: Integral sextupole decay and snapback of the short LHC dipole model magnet MBSMS4V1.

The reason for this positive and negative contribution from different coils can be attributed to the presence of a periodic pattern in the sextupole along the length of the magnet as discussed at length in Chapter 2. The magnet coils are built up with twisted Rutherford cable. In combination with a non-uniform current distribution this twisted cable leads to a periodic pattern in the harmonic components. The periodic pattern changes in time, both in amplitude and phase, following the change in cable current distribution.

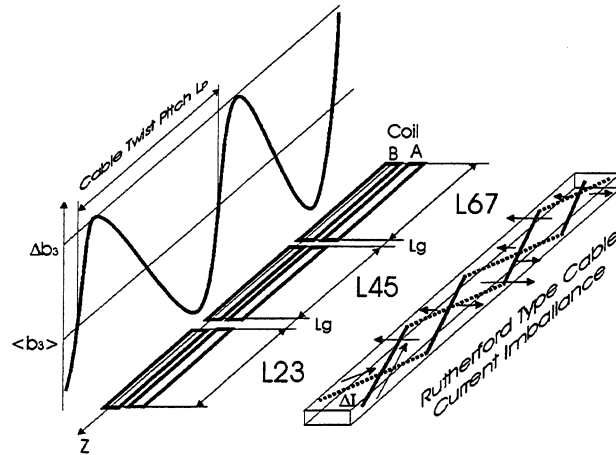


Figure 4.12: Periodic pattern influence on the rotating coil system in Block4.

Figure 4.12 shows the general concept of the equivalent rotating magnetic moment along the z -axis of a two-wire cable with a non-uniform current distribution. We show schematically the sextupole periodicity along the magnet, and the position of the measurement shaft. Note that for the short models we expect the amplitude to be roughly constant over the whole length of the measurement system. This condition appears to be very likely in accordance to the earlier estimation of a characteristic length for the periodic pattern as given in [76]. This characteristic length was calculated to be in the range of 2 meters on each side of the magnet heads. In our case, where the magnet has a total length of 1 meter, a strong interaction of incoming diffusion waves from both sides of the magnet can be expected, which leads to a more or less constant amplitude over the magnetic measurement coils L23, L45 and L67. These three inner coils are the so-called “mid-section” in our measurement system.

With reference to the scheme above, we write that the sextupole b_3 as a function of z is given by:

$$b_3(z) = \langle b_3 \rangle + \Delta b_3 \sin\left(2\pi \frac{z}{L_p} + \varphi\right) \quad (4.31)$$

where:

$\langle b_3 \rangle$ is the average value of the periodic pattern (caused by geometric and DC magnetization contributions).

Δb_3 is the amplitude of the periodic pattern signal.

L_p is the twist pitch of the Rutherford cable.

φ is the phase shift between origin of periodic pattern and measurement system origin.

The signal measured by a single coil (e.g. L23) is the integration of b_3 along the z -axis over the length L of the coil.

$$b_3^{meas}_{123} = \frac{1}{L} \int_0^L \left[\langle b_3 \rangle + \Delta b_3 \sin\left(2\pi \frac{z}{L_p} + \varphi\right) \right] dz \quad (4.32)$$

The division by L is necessary because we are automatically performing a normalization on the length of our measurement coils during data acquisition. Considering above $\varphi = 0$ and $L = L_p$ we get in particular

$$b_{3123}^{meas} = \langle b_3 \rangle. \quad (4.33)$$

In our case the measurement coil length is short, it is not an integer number of twist pitches, and its position cannot be adjusted. Therefore the result of the single coil measurement leads in any case to a sextupole value which is a function of coil length, twist pitch length, periodicity amplitude and phase. Therefore the variations of the periodic pattern amplitude and phase result in an artificial variation of the sextupole values measured by the single coils.

Once the shaft geometry and the cable twist pitch are known we can write the following system for the measured values in the three coils of the mid section:

$$b_3^{L_{23}} = \frac{1}{L_{23}} \int_0^{L_{23}} [\langle b_3 \rangle + \Delta b_3 \sin(2\pi \frac{z}{L_p} + \varphi_1)] dz \quad (4.34)$$

$$b_3^{L_{45}} = \frac{1}{L_{45}} \int_0^{L_{45}} [\langle b_3 \rangle + \Delta b_3 \sin(2\pi \frac{z}{L_p} + \varphi_2)] dz \quad (4.35)$$

$$b_3^{L_{67}} = \frac{1}{L_{67}} \int_0^{L_{67}} [\langle b_3 \rangle + \Delta b_3 \sin(2\pi \frac{z}{L_p} + \varphi_3)] dz \quad (4.36)$$

where the phases are related by the following expressions

$$\varphi_2 = \varphi_1 + 2\pi \frac{L_{23} + L_g}{L_p} \quad (4.37)$$

$$\varphi_3 = \varphi_2 + 2\pi \frac{L_{45} + L_g}{L_p} \quad (4.38)$$

where:

L_{23}, L_{45}, L_{67} is the length of the three inner coils (l_{23}, l_{45}, l_{67}) in the measurement system.

L_g is the gap between the measurement coils.

$\varphi_1, \varphi_2, \varphi_3$ is the phase shift between origin of the periodic pattern and each measurement coil L_{23}, L_{45}, L_{67} .

In the system above we have only two free parameters (Δb_3 and φ_1). To give an order of magnitude for the amplitude variation we have taken the data of MBSMS6V1. The snap-back can be seen as a constant value for all three coils in the measurement system, a property that indeed seems to be maintained throughout our measurements. We postulate that this value is representative of the *true* decay of the sextupole. If we use the snap-back value for the average sextupole value $\langle b_3 \rangle$ at the end of the decay, we can solve

numerically the system of equations above. We obtain in particular the following results for the phase and amplitude of the periodic pattern:

Table 4.6: Amplitude and phase of periodic sextupole pattern estimated for MBSMS6V1 mid section. The amplitude Δb_3 agrees within the order of magnitude of periodic pattern measurement results obtained from a 10-meter long model magnet.

$\Delta b_3 = 6,43$ units	$\varphi_l = 0,45$ rad
---------------------------	------------------------

The amplitude estimated above is comparable to results of direct periodicity measurements on 10-meter long model magnets. For 10-meter magnets the values for the periodic pattern amplitude in steady state are typically in the range of 10 units, with large variations at the coil ends.

We have repeated the same analysis for five magnets tested, on both sextupole and decapole components. The results are reported in Table 4.7. Again we note that the order of magnitude of the estimated amplitudes is consistent with previous direct measurements.

Table 4.7: Estimated periodic pattern sextupole and decapole amplitude for 1 m long MBSMS series magnets

	MBSMS3	MBSMS4	MBSMS5	MBSMS6	MBSMS8	
b_3	5.11	9.14	10.59	6.43	6.55	units
b_5	0.27	0.87	1.28	0.72	1.23	units

Finally we have to state that periodic pattern has less influence on decay measurements performed in SM18 with the 750 mm long single coil as the ratio of twist pitch to coil length is much smaller in this case.

4.4.5. Decay Characterization

We have parameterized the decay by fitting an exponential function to the field harmonics during injection porch [75, 98]. Depending on the type of measurement and the signal to noise ratio for the particular harmonics coefficient a function of one or two time constants was used. The functions are given in Equation 4.39 and 4.40. Usually Equation 4.39 can always be applied to allowed harmonics for short time decay measurements, which last for approximately 1000 s, when then operation current of the magnet is fixed. For long time decay measurements, which last for approximately 10000 s, it is sometimes not possible to apply Equation 4.40. The above explained periodic pattern effect does not allow a two time constant parameterization. Consequently long time decay measurements must be estimated with less fit quality by a single time constant fit.

$$c_{n,Fit}(t) = A + B \left(1 - e^{-\frac{t}{\tau}} \right) \quad t \in [0, T_{inj}] \quad (4.39)$$

$$c_{n,Fit}(t) = A + B \left(1 - e^{-\frac{t}{\tau_1}}\right) + C \left(1 - e^{-\frac{t}{\tau_2}}\right) \quad t \in [0, T_{inj}] \quad (4.40)$$

Parameter A is simply fixed to the initial harmonics value at injection. Thus B and τ , respectively B , C , τ_1 and τ_2 give the set of parameters which must be fit to the harmonics decay at injection. The parameter t is the time when the magnet is held on constant excitation current, from now on called injection. T_{inj} is the total injection duration. The quality of this fit is given by the standard deviation, which is derived from Equation 4.41.

$$\sigma_{c_n} = \sqrt{\frac{\sum_{i=1}^N (c_n(t_i) - c_{n,Fit}(t_i))^2}{N-1}} \quad (4.41)$$

According to the discrete number N of measurements during injection porch the time t is a discrete sample.

A typical decay respectively fit scenario due to periodic pattern influence on the five-coil rotating coil system is shown in Figure 4.13. We see the integral sextupole decay and snapback of MBSMS4V1 and the decapole decay of MBSMT1V1 aperture 1 (A1). The decay data of the first magnet can only be characterized by a single time constant fit, while a two time constant model was applied to the second magnet. The fit values are listed in Table 4.8

Table 4.8: Typical fit parameter for decay characterization.

	harmonic	A (units)	B (units)	C (units)	τ_1 (s)	τ_2 (s)
MBSMT1V1A1	b_5	$2.91 \cdot 10^{-1}$	$-1.19 \cdot 10^{-2}$	$-7.18 \cdot 10^{-2}$	249	4250
MBSMS4V1	b_3	-7.86	$3.21 \cdot 10^{-1}$	-	673	-

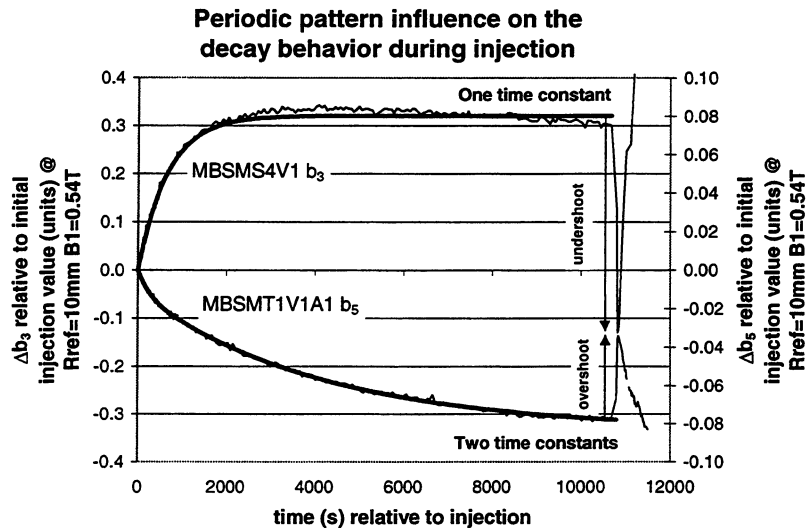


Figure 4.13: Two different fit scenarios of decay at injection porch presented as example of MBSMS4 and MBSMT1 magnetic measurement results.

4.4.6. Snapback Calculation

The snapback computation procedure has to measure the difference between the final decay value and the actual value when the multipole joins the hysteresis after the rapid bounce back when re-establishing the ramp conditions at the end of injection.

The snapback computation is performed automatically by applying the following procedure:

- In order to avoid noise influence the last five measurement points of the decay phase undergo an averaging process, which leads to the final decay value at the end of injection.
- The decision whether to search for a minimum or a maximum during the snapback phase (usually including not more than five measurement points because of the rapid behavior) can easily be deduced from the sign of the hysteresis slope before reaching injection.
- The snapback itself is computed as the difference of the final decay value and conditionally the minimum or maximum of the snapback phases.

This procedure appears to be very stable down to a signal to noise ratio where the slope of the hysteresis is attributed to random errors. We concentrate mainly on the allowed and the first few non-allowed harmonics. Random errors on these harmonics are small. Therefore we can believe that we can compute accurate values for b_3 , b_5 , b_7 , and for b_9 and for non-allowed harmonics a_2 and a_4 .

5. Experimental Results at LHC-MTA

The results of the magnetic measurements are presented here in two sections. In the first section, called *Standard Operation Cycle Experiment* we compare results from several magnets and we derive statistically significant numbers like decay and snapback amplitude or decay time constants. The second section is called *Operation Cycle Variation Experiment*. It deals with the influence of operation current variation on the sextupole snapback.

5.1. Standard Operation Cycle Experiments

5.1.1. Operation cycle definition

As mentioned during the historical review of this thesis the behavior of the decay or snapback depends strongly on the operation cycle history. Consequently results from magnetic measurements can only be compared with each other when applying a standardized operation cycle procedure. Thus the first step of systematic research must be the definition of an appropriate power cycle for the experiments.

The powering cycle can be logically separated into two parts. The first part causes a “normalized” condition of the superconducting magnet. This sequence starts with quenching the magnet, which deletes the memory of the previous powering history in the magnet's superconducting winding. The following cleansing cycle prepares well-defined operation conditions for all the pending measurements. In practice this means that the following measurement is performed on the reproducible hysteresis curve and not on the virgin curve.

The second part is understood as the *measurement cycle* itself. The measurements discussed in this thesis are usually made at the injection porch and the start of the ramp after injection.

Table 5.1 shows the nominal values of the standard operation cycle. A schematic drawing of the standard operation cycle is shown in Figure 5.1.

Table 5.1: Standard operation cycle parameters, which were used during the time dependent effect measurement program at CERN / MTA. Starting with MBSMS3V1 all the following short dipole model magnets were observed under these conditions.

Cycle part name	Shortcut	Standard value and unit
Pre-Cycle Current	I_{FT}	11750 A
Pre-Cycle minimum Current	I_{MIN}	50 A
Pre-Cycle Duration	T_{FT}	1800 s
Pre-Cycle Ramp Rate	RR_{FT}	50 A/s
Injection Ramp Rate	RR_{INJ}	1 A/s
Injection Current	I_{INJ}	810 A
Injection Duration	T_{INJ}	1020 s / 10000 s
Acceleration Ramp Rate	RR_A	1 A/s
Final Current		1500 A
Temperature		1.8 K

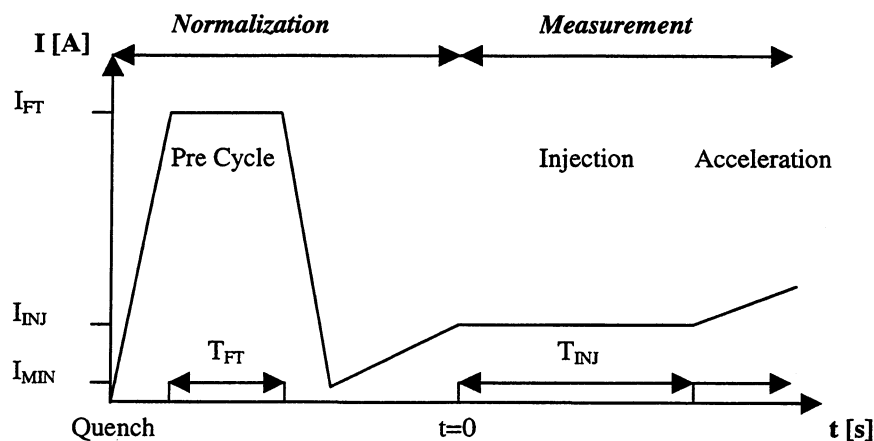


Figure 5.1: Schematic drawing of the standardized operation cycle and its elements for the dynamic effect experiments.

5.1.2. Statistical Analysis

The experimental set-up provides all the requirements to perform reproducible experiments on dynamic effect studies for a group of similar magnets. The statistical analysis of the experimental data provides information concerning the following three questions:

- Which are the harmonic coefficients that show systematic decay and snapback?
- Is there a correlation of decay between different harmonics?
- What are the statistical numbers characterizing the harmonics component decay and snapback?

5.1.2.1. Systematics of Multipole Decay and Snapback

The first analysis concerning the decay behavior of the harmonic components is focused on the question if there is some sort of system in the spectrum. In order to derive a statistically significant information about the decay behavior in the harmonics up to b_9 the whole population of one-meter long model magnets from the MBSMS series was used. The decay and the snapback were analyzed. The snapback of the interesting harmonics is plotted in Figure 5.2. In order to provide a useful presentation of the harmonics up to number 9 we have to scale the harmonics in the following way: $a_2...b_3$ with factor 1, $a_4...b_5$ with factor 10, $a_6...b_9$ with factor 50. We observe a systematic distribution for harmonics only in case of allowed multipoles. They are systematically distributed either with positive or negative sign. Non-allowed harmonics are randomly distributed around zero. Based on this information we can focus our observations on allowed harmonics only.

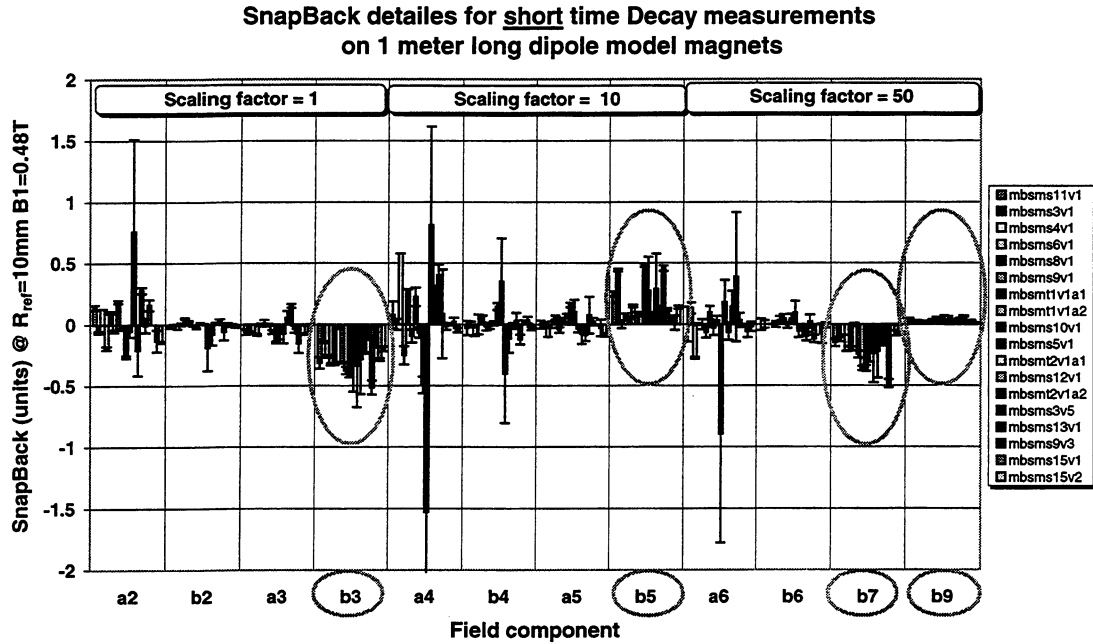


Figure 5.2: Spectral distribution of snapback for the MBSMS LHC dipole model series. Allowed harmonics are specially labeled. They are the only field components, which show a systematic distribution.

An equivalent analysis was performed on long time (10000 s) measurements during injection porch. Apart from an increase of amplitude nothing changed in the systematics of distribution.

5.1.2.2. Correlation of the Harmonics Component Decay

In early HERA publications [43] a correlation between the final dipole and sextupole decay rate was found. In this context the importance of this correlation in the scope of the existence of a unique source driving the harmonics decay during constant excitation is mentioned. From our point of view this correlation should be investigated in more depth. This opinion must be seen within the following context. The fact that a correlation between different harmonics exists and that it is really strongly pronounced could finally lead to a scaling between the harmonics.

Thus we recorded the decay during a waiting time of 1000 s at the injection porch. The experiment was performed on a number of short dipole model magnets of the MBSMS series. Plotting b_3 against b_5 as function of the injection duration reveals a strongly linear correlation for each of the magnets. The slope of this linear correlation is a characteristic property for all magnets. Figure 5.3 shows this fact.

Correlation between Sextupole and Decapole Decay of MBSMS magnets during 17 minutes of injection porch.

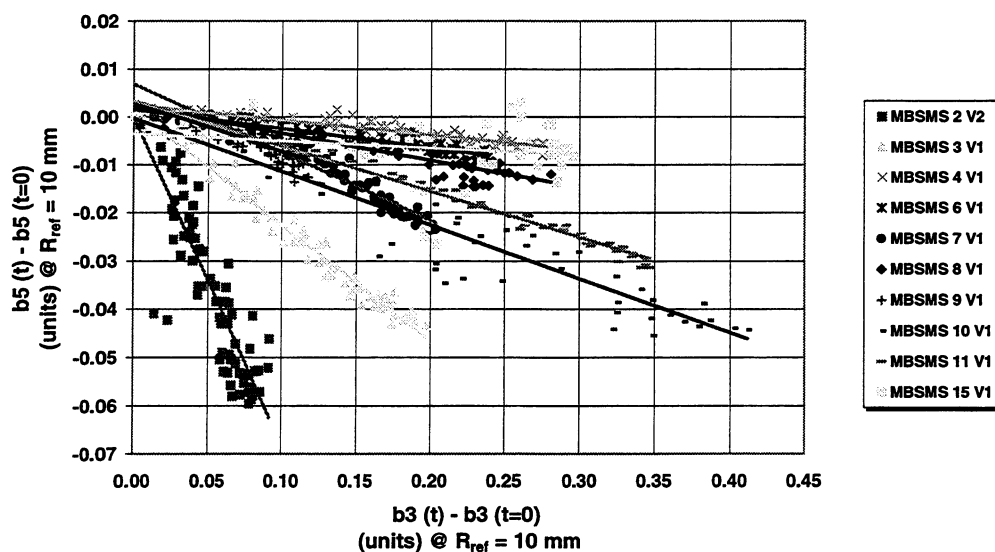


Figure 5.3: Correlation between the normal decapole and sextupole of the MBSMS series magnets during 17 minutes at injection.

A correlation between the dipole component and the sextupole component as shown in HERA publications is difficult to deduce. At HERA the dipole decay was measured by use of a NMR device. Instead rotating coil measurements are made to deduce the dipole component at LHC at present. The expected dipole decay is of the order of 10^{-4} T, which is difficult to measure by means of rotating coils. But we have seen the dipole decay in long time (10000 s) observations of sextupole and dipole component during injection porch. A possibly linear correlation appears when plotting the final decay value of the dipole component versus the final decay of the sextupole. It is planned to use NMR probes for dipole component measurements at LHC. Future measurements with NMR probes will provide a much clearer picture of the decay phase of the dipole during injection.

5.1.2.3. Statistics of Multipole Dynamics

Two quantities of interest can be derived from the above measurements. Firstly the mean of the snapback values for a duration of 1000 respectively 10000 seconds at injection for all the available one-meter long LHC model magnets can be derived. These numbers are shown in Figure 5.4. One must note the scaling factor ($a_2...b_3$ with factor 1, $a_4...b_5$ with factor 10, $a_6...b_9$ with factor 50) as used before for different harmonics in order to visualize them within one graph. In fact Figure 5.4 can be seen as a conclusion of Figure 5.2, where single magnet snapback values are shown. Better than in Figure 5.2 we see a systematic effect only on allowed harmonics while the mean of non-allowed harmonics is usually very small and embedded into the error bar around zero. These mean numbers, one for each multipole up to harmonic number 9, give a first impression concerning the distribution of mean values to be expected in an accelerator along its circumference.

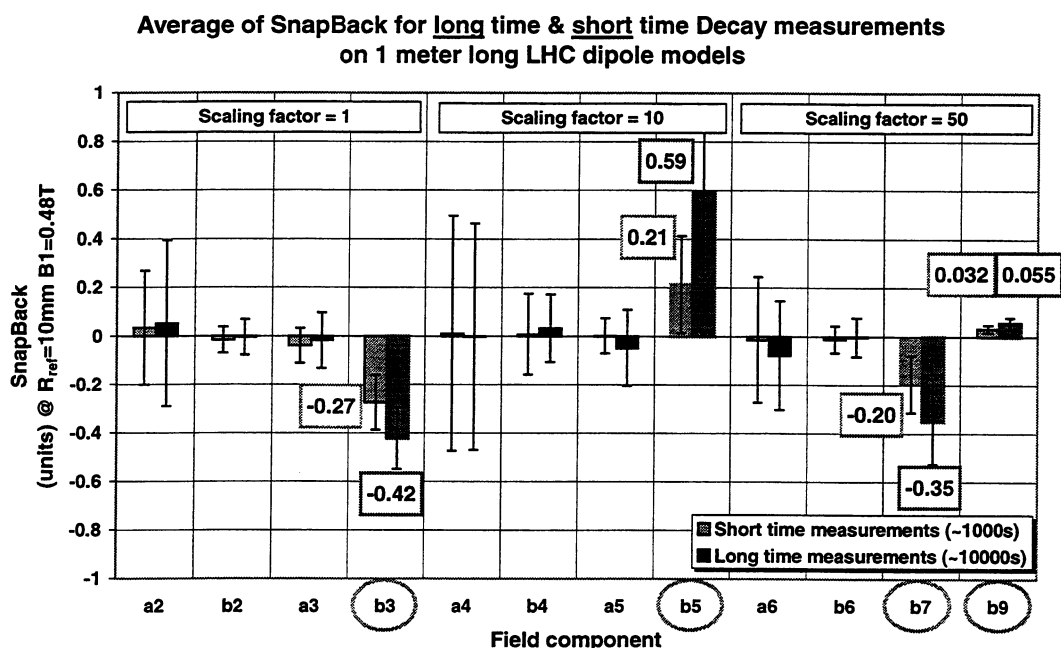


Figure 5.4: Statistics concerning the average of snapback obtained from the available population of one-meter long LHC dipole model magnets. A comparison between measurements obtained from 17 minutes and 2.7 h of injection duration is presented.

The summary of the mean numbers and their sigma is given in Table 5.2. Values are grouped according to their different injection duration and allowed harmonics are highlighted.

Table 5.2: Average of snapback values and their standard deviations for all available one-meter long LHC dipole model magnets. Long time and short time measurements at injection are compared. Allowed harmonics are highlighted.

Harmonic	1000 s @ injection		10000 s @ injection	
	\bar{x}	σ	\bar{x}	σ
a ₂	3.37E-02	2.34E-01	5.17E-02	3.42E-01
b ₂	-1.62E-02	5.35E-02	-4.65E-03	7.25E-02
a ₃	-3.91E-02	7.14E-02	-1.76E-02	1.14E-02
b₃	-2.74E-01	1.14E-01	-4.22E-01	1.26E-01
a ₄	1.08E-03	4.84E-02	-2.95E-04	4.66E-02
b ₄	8.12E-04	1.65E-02	3.18E-03	1.38E-02
a ₅	1.63E-04	7.19E-03	-4.83E-03	1.56E-02
b₅	2.13E-02	1.99E-02	5.92E-02	3.38E-02
a ₆	-2.85E-04	5.15E-03	-1.58E-03	4.49E-03
b ₆	-2.44E-04	1.09E-03	-5.93E-05	1.59E-03
b₇	-3.91E-03	2.35E-03	-6.99E-03	3.52E-03
b₉	6.39E-04	3.03E-04	1.10E-03	4.58E-04

Secondly an analysis of the decay behavior during the injection porch leads to characteristic time constants. The data for this analysis were obtained from long time (10000 s) and short time (1000 s) decay measurements at injection. During the injection

porch the decay of multipoles was fitted with a one-time constant decay model (see Equation 4.39) for short time decay measurements. For long time decay we applied a two time constant model (see Equation 4.40) to the field component decay when ever possible. The time constants for each magnet were then sorted according to the order of harmonics and the average was computed. Applying this procedure to short time measurements we derive average time constants for the allowed harmonics up to b_9 which can all be found in a range of a few hundred seconds (see Table 5.3). It is obvious, that the average values are already set in one order of magnitude. But the large local sigma, for example for b_5 and b_9 , still point to the dominant contribution of some bigger time constants to this small population or to a possibly strong periodic pattern influence on the measurement system. The average value of the first four allowed harmonics (b_3 to b_9) is 536 seconds, which allows a good estimation of the decay during injection.

Observing the spectrum of time constants for long time decay measurements we found an equivalent behavior for the first time constant $\bar{\tau}_1$. Again the average values of all the observed b_5 and b_9 time constants are embedded into large error bars with magnitude on the order of the values itself. The first average decay time constant of the short LHC dipole model population is now slightly reduced to 476. The average values for the second time constant $\bar{\tau}_2$ for long time measurements are more stable in respect to the relative deviations. However the sigma is still too large for a stable systematics. One should note that the large error bars for all the time constants are the consequence of periodic pattern influence on the fit results as mentioned above. By computing the total average of the first four allowed harmonics we derive 3894 seconds for the second average time constant. First and second time constant together allow a good estimation of the decay during the long time injection. Numerical values are shown in Table 5.3.

Combining the total average values of the first and the second time constant we compute a quotient of 8.2. This value verifies the current diffusion theory for the Rutherford type cable proposed by [76, 77, 78, 79], where a ratio of 9 between $\bar{\tau}_1$ and $\bar{\tau}_2$ was predicted.

Table 5.3: Allowed harmonics average time constants obtained from short and long time injection decay measurements on one-meter long LHC dipole model magnets.

Harmonic	1000 s @ injection		10000 s @ injection			
	$\bar{\tau}$ [s]	σ [s]	$\bar{\tau}_1$ [s]	σ_1 [s]	$\bar{\tau}_2$ [s]	σ_2 [s]
b_3	469	192	343	196	3864	3214
b_5	880	723	646	867	3993	2617
b_7	469	185	369	130	3096	1475
b_9	326	436	546	540	4623	2104
<i>average</i>	<i>536</i>		<i>476</i>		<i>3894</i>	

5.1.2.4. Conclusion of the Statistical Analysis

In this chapter we presented the standard decay measurements and their statistical interpretation.

We showed the presence of systematic time dependent effects on all allowed harmonics for the one-meter long LHC dipole model magnets series in case of the single aperture model as well as for the first twin aperture model design. The average values for allowed

harmonics are distributed systematically either on the negative or positive side of the spectrum of harmonics, alternating in sign from one order to the other. Non-allowed harmonic's snapbacks are randomly distributed on the positive or negative side of the spectrum within each order of the harmonic field component. Their average values are embedded into error bars around zero.

A correlation between the different harmonics was investigated. We found that the decay during the injection shows a strong linear correlation between b_3 and b_5 on the same magnet for the MBSMS series magnets. But the strength of the decay rate is inversely correlated. Thus stronger decay on b_3 leads to weaker decay on b_5 and vice versa.

The fact that systematic effects are observed on allowed harmonics only and that the decay of allowed harmonics is correlated allows focusing only on b_3 during the following experiments.

The statistics for the decay time constants show a systematic trend in the magnitude of theoretically predicted values. This prediction is based on a current diffusion model for current loop decay in a two wire Rutherford type cable and extrapolated to real size magnets. Analyses of the average values for the first two time constants and their quotient agree well with this model prediction. We hope that the large error bars of the presented average values for the available population of LHC dipole model magnets can be reduced by increasing the number of magnets tested.

5.2. Operation Cycle Variation Experiments

When observing time dependent effects in LHC dipole magnets, the most interesting question is the influence of different powering conditions on the snapback at the start of the acceleration phase. Therefore the standardized cycle was modified step by step. Only one parameter after the other was modified and the snapback was recorded and plotted as a function of this parameter variation. The operation cycle definitions, their standard values and the parameter variations are shown in Table 5.4. The drawing of the cycle and its parameters are shown in Figure 5.5. Following the experiments throughout this chapter shows how this procedure of systematically varying single parameters influences the snapback behavior of the LHC dipole model magnets.

Table 5.4: Standard operation cycle parameters and their variations.

Cycle part name	Shortcut	Standard value	Variation
Pre-Cycle Flat Top Current	I_{FT}	11750 A	0...12800 A
Pre-Cycle minimum Current	I_{MIN}	50 A	-
Pre-Cycle Flat Top Duration	T_{FT}	300 s	60...7200 s
Pre-Cycle Ramp Rate	RR_{FT}	50 A/s	33 up 100 down 100 up 33 down A/s
Pre-Injection Duration	T_{PreInj}	-	60...1800 s
Pre-Injection Current	I_{PreInj}	-	735...785 A
Injection Ramp Rate	RR_{INJ}	1 A/s	0.5...4 A/s
Injection Current	I_{INJ}	810 A	-
Injection Duration	T_{INJ}	1020 s	-
Acceleration Ramp Rate	RR_A	1 A/s	-
Number of Pre-Cycles		1	1...6
Number of Operation Cycles		1	1...4
Temperature		1.8 K	-

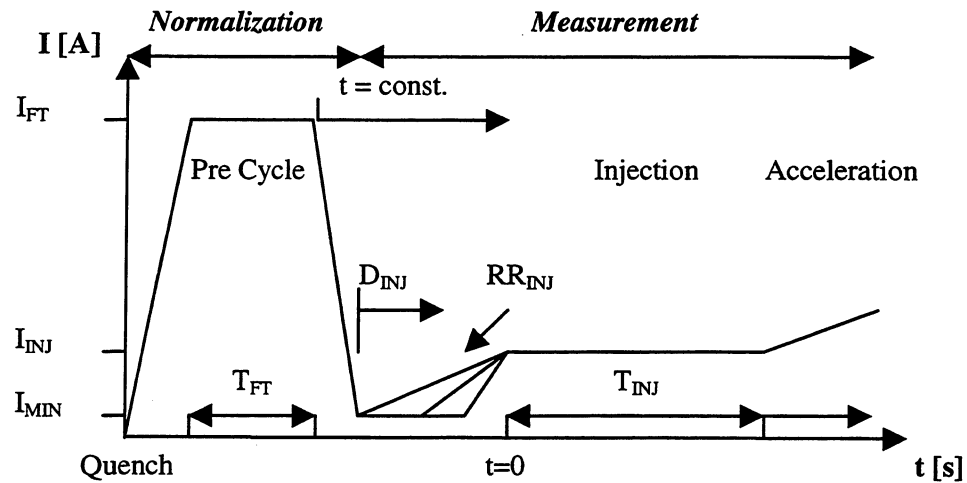


Figure 5.5: Drawing of the operation cycle and its parameters.

The operation cycle variation will be divided into two subsections. One provides information about the variations of the injection conditions and the other one deals with pre-cycle related operation parameter variations.

5.2.1. Injection Variations

The injection variation experiments cover variations of the pre-injection duration, pre-injection current and the ramp rate to injection.

5.2.1.1. Pre-Injection Duration

Figure 5.6 shows that different pre-injection duration times can significantly influence the snapback. The short (1 meter long) model dipole as well as the long (10 meter long) one show a reduction of about 50% after 30 minutes of pre-injection duration.

5.2.1.2. Pre-Injection Current

The pre injection current itself does not seem to influence the sextupole snapback behavior significantly. The injection current is usually placed at 810 A. We set up measurements at 735 A, 750A and finally at 785A, but the time between the end of the pre cycle and the injection porch was held constant. A maximum reduction of about 15% was observed on the long model magnet when the pre injection current was closest to the injection current. Figure 5.7 contains analyses results from a short model as well as from a long model magnet. But we see that the pre-injection current influences the longer magnet more than the shorter one.

5.2.1.3. Ramp Rate to Injection

For the ramp rate to injection experiment we performed a cycle, in which the time between the end of the pre-cycle and the injection porch was held constant. The slowest ramp (0.05A/s) therefore started directly after reaching the minimum current and the fastest one started after a rest at the minimum current for 1180 seconds. We clearly see an

increase of the sextupole snapback for higher ramp rates. The results of this experiment are shown in Figure 5.8.

5.2.2. Pre Cycle Variations

The pre-cycle variation experiments cover variations of the pre-cycle current, duration and ramp rate. It also deals with the influence of multiple pre-cycles and multiple operation cycles on the sextupole snapback.

5.2.2.1. Pre-Cycle Flat Top Current

The Pre-Cycle current shows (see Figure 5.9) a significant influence on the sextupole snapback. We see a nearly linear reduction of the snapback from high to low currents. But approaching 4000 A a significant and systematic bending is observed, which leads to a flat region between 4000 A and 0 A of the pre-cycle current. We performed measurements down to minimum pre-cycle current with the single aperture magnet MBSMS12V1 and with the twin aperture magnet MBSMT1V3. The result shows a flat approach around 0.1 units on the sextupole snapback. Thus the pre-cycle current below 4 kA does not significantly influence the snapback value or the decay rate of the sextupole component. Apart from this general rule the MBSMS and MBSMT magnets must be split into two groups. One group represents the five-block design, while the other group represents the modern six-block design. At least two of the six-block design magnets (MBSMS17V1 and MBSMS18V1) show a significantly stronger dependence on the increasing flat top current than the other five-block magnets. One must explicitly mention magnet MBSMS9V2. It shows very low snapback values. The reason for this extraordinary behavior is not known.

The magnet labeled as MTP1A3 (aperture 2) is a ten-meter long prototype of the historical 50-mm aperture design. Thus its behavior is different to all the others. There is still a general trend of the flat top current influence on the snapback values for this magnet. But the values appear to be significantly higher than for short models.

The 10-meter long dipole model MBL1AJ2 (aperture 1) also shows a snapback dependence on flat top current. Its snapback values were not directly available were estimated from decay measurements.

5.2.2.2. Pre-Cycle Flat Top Duration

Similar to the Pre-Cycle Flat Top Current experiment we have to split the results of the Flat Top Duration measurements (see Figure 5.10) into two groups. The criterion for the grouping is again the difference in the design.

The Pre-Cycle duration influence on the sextupole snapback for a five-block design can be characterized as an exponential increase starting after a short time on flat top. The behavior of each magnet is very similar. A saturation is observed for magnet number 12, which is exposed to flat top current of 11750 A and a flat top duration for 30 and 60 minutes. All the other magnets tend to saturate more slowly. It looks as if a characteristic time constant smaller than 1 hour can be interpreted by fitting the data set with an exponential model. The time constants should not deviate too much from magnet to magnet. In general we see that all the magnets increase their snapback monotonously value when the flat top duration is increased.

In contrast to this behavior the newer six-block design magnets show dramatically altered properties. The snapback value as a function of the flat top duration increases rapidly and reaches its maximum just below 20 minutes of flat top duration. Above this threshold the snapback decreases significantly and possibly shows saturation for longer flat top duration. This behavior is consistent for all six-block magnets.

Again we see that the first generation 10 meter long, 50 mm aperture prototype magnet MTP1A3 shows a much more pronounced flat top duration dependence than all of the present generation magnets.

5.2.2.3. Pre-Cycle Flat Top Duration-Current Surface

In the scope of real machine operation a combination of different Pre-Cycle Flat Top Durations and Currents seems to be a likely situation. That is why we explored the behavior of the one-meter long single aperture LHC dipole model MBSMS12V1 in an extended period of measurements. The results of these measurements are shown in form of the Pre-Cycle Flat Top Duration-Current Surface in Figure 5.11.

We observe that the sextupole snapback is nearly constant below 4000 A of the flat top current. In this regime the snapback value is only weakly dependent on the flat top duration.

The snapback increases in an almost linear way when the flat top current is increased above 4000 A. But now the strength of the snapback depends on the flat top duration as well.

5.2.2.4. Check of Systematics in b_5 and b_7

We have already seen that there is a high correlation between the decay of b_3 and b_5 during injection. This correlation may also show up in the operation cycle variation experiments. In order to verify this assumption we plot the snapback in the harmonics b_5 and b_7 as function of the Pre-Cycle Flat Top Current. The result is shown in Figure 5.12 and Figure 5.13. It is obvious that the allowed harmonics are very consistent within the given accuracy (error bar). Comparing the results with Figure 5.9 we again see the systematic alternation in sign for the allowed harmonics. Furthermore we see an equal trend concerning the increasing flat top current for the first allowed harmonics (b_3 , b_5 , b_7) on a small number of magnets.

5.2.2.5. Pre-Cycle Ramp Rate

We performed the pre-cycle ramp rate experiments by use of two different parameter sets for upward and downward ramp speed as documented in Table 5.5. The total Pre-Cycle duration was held constant. A schematic drawing of the cycles and the results of the snapback measurements are shown in Figure 5.14. The sextupole snapback differs by 0.068 units in the two operation cycles. The higher value was observed during the "slow-fast" cycle. The relative difference in the sextupole snapback in respect to a standard pre-cycle is around $\pm 10\%$.

Table 5.5: Pre-Cycle Ramp Rate experiment parameters. The purpose of this specific set of upward and downward ramp rates was to keep the total pre cycle duration constant in respect to a standard pre cycle. The ramp rate for a standard pre cycle is 50 A/s.

Cycle Type	Ramp Rate upwards (A/s)	Ramp Rate downwards (A/s)	b3 Snapback (units)	Relative difference to standard cycle (units)
Fast-Slow	100	33	-2.94E-01	-10.9%
Slow-Fast	33	100	-3.62E-01	9.6%
Standard	50	50	-3.30E-01	

5.2.2.6. Multiple Pre-Cycle

Three one meter long LHC dipole model magnets were exposed to a sequence of 1, 3 and 6 pre-cycles, followed by an injection porch. A quench was performed in between each of the three cycles. The result of this experiment (see Figure 5.15) is of high interest. At least after 3 to 6 pre-cycles a very fast saturation was observed. This implies a time constant even less than 40 minutes. The sextupole component snapback appears more or less as a constant value after this time of continuously cycling the magnet.

We have to point out the significantly smaller sextupole snapback in case of magnet MBSMS9.

5.2.2.7. Multiple Operation Cycles (Injection Reproducibility)

The result of the injection reproducibility experiment is shown in Figure 5.16. It is of great importance for the future accelerator operation. A cycle, which is likely to be a typical operation cycle, was applied to the magnet. It started with quenching the magnet (this is not a typical operation condition) followed by four total cycles without quenching in between. The snapback was always measured at the initial phase of the acceleration ramp. It was verified for at least three magnets that one can expect to have reproducible injection conditions after performing collision experiments at the flat top current. Since the total cycle duration is around 45 minutes, we assume to see a system time constant much smaller than 1 hour. Otherwise continuous cycles in operation conditions comparable to this would have to influence each other.

5.3. Conclusion of Measurements

In this chapter statistical results concerning the time constant of the field component decay during injection and average values of the snapback on one-meter long LHC dipole models were derived. As a result we showed that a systematic behavior in decay and snapback must be expected only for normal allowed field harmonics, while non-allowed harmonics and skew allowed harmonics are randomly distributed. Furthermore there is a significant correlation of the field component decay for the various allowed harmonics. These experiences support the strategy of observing the snapback behavior of allowed harmonics while varying different operation cycle conditions. The results of the operation cycle variation experiments will be used for the modeling of snapback in the following chapter.

The entire population of one-meter long LHC dipole model magnets, which were operated under several varied operation conditions, showed a consistent snapback

behavior. The snapback behavior of the 10 meter long, five-block design, 56 mm aperture magnet MBL1AJ2 and the 10 meter long, six-block design, 50 mm aperture, former generation dipole prototype MTP1A3 is similar to the general behavior of the one-meter long LHC dipole model. Two experiments (Pre-Cycle Flat Top Current and Duration) were performed on five-block design magnets and on six-block design magnets. There is a first indication that the snapback behavior of the six-block design magnets differs significantly from the behavior of the five-block design magnets. In future six block design magnets will be involved in the missing operation cycle variation measurements to clarify their snapback behavior in comparison to the five-block design magnets.

Apart from this very general discussion we can comment on the extent of the influence of each of the operation cycle variations on the sextupole snapback. Therefore the following two tables were produced. One table accounts for the five-block design and one table for the six-block design magnets. The tables contain the name of the varied parameter in the first column. The second column shows the maximum change in the sextupole snapback over the total range of parameter variations and over the total number of magnets involved in the particular experiment (see Table 5.4). Finally the tendency of the sextupole snapback when increasing one particular parameter is indicated in the last column.

Table 5.6: Operation cycle parameter influence on the snapback behavior of the five-block, one meter long LHC dipole model series MBSMS / MBSMT magnets.

Parameter	Maximum change in b3-snapback [units @ $R_{ref}=10\text{mm}$]	Tendency
Pre-Injection Duration	0.2	inverse
Pre-Injection Current	0.1	inverse
Ramp Rate to Injection	0.15	proportional
Pre-Cycle Flat Top Current	0.2	proportional
Pre-Cycle Flat Top Duration	0.2	proportional
Pre-Cycle Number	0.15	proportional
Multiple Operation Cycles	0 (one meter model) 0.05 (ten meter model)	- proportional

A corresponding table for the six-block design one-meter long model magnets shows quite well the difference in their sextupole snapback behavior in contrast to the five block design.

Table 5.7: Operation cycle parameter influence on the snapback behavior of the six-block, one meter long LHC dipole model series MBSMS magnets.

Parameter	Maximum change in b3-snapback [units @ $R_{ref}=10\text{mm}$]	Tendency
Pre-Cycle Flat Top Current	0.4	proportional
Pre-Cycle Flat Top Duration	0.2	proportional, passing maximum, inverse

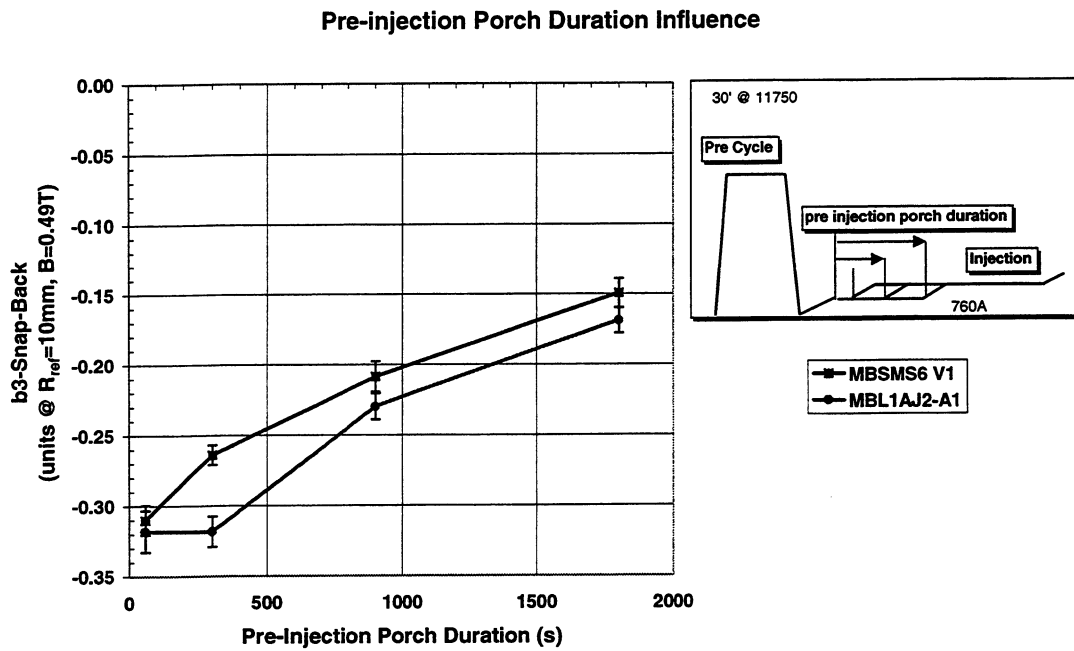


Figure 5.6: Pre-Injection duration influence on the sextupole snapback of a one-meter (MBSMS6V1) and a 10-meter (MBL1AJ2-A1) long dipole model.

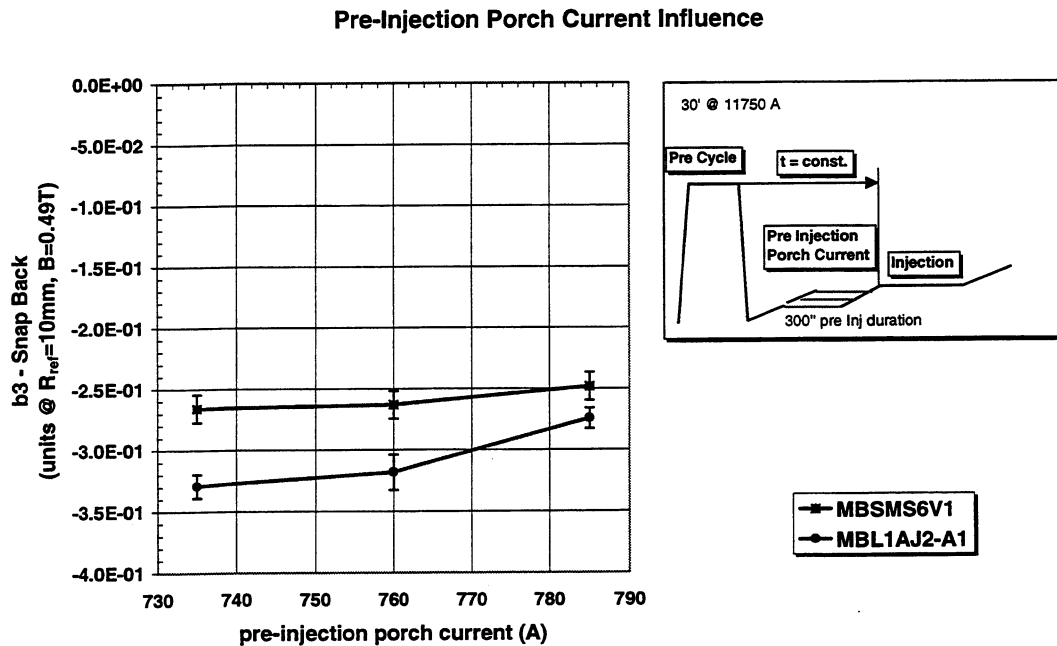


Figure 5.7: Pre-Injection current influence on the sextupole snapback of a one-meter (MBSMS6V1) and a 10-meter (MBL1AJ2-A1) long dipole model.

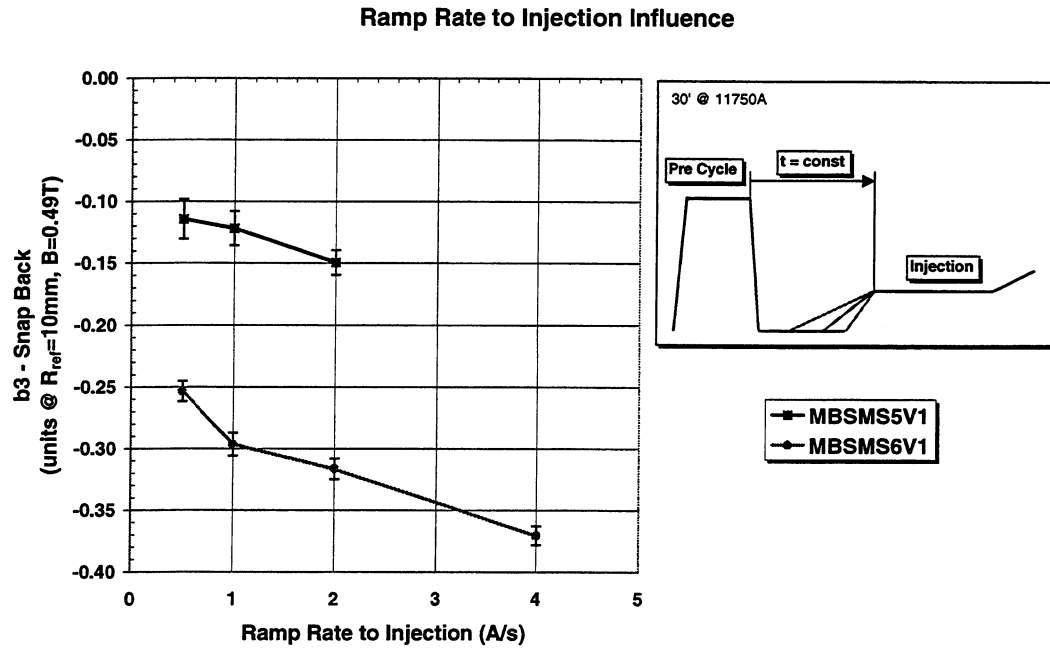


Figure 5.8: Ramp Rate to injection influence on the sextupole snapback of two one meter long LHC dipole model magnets.

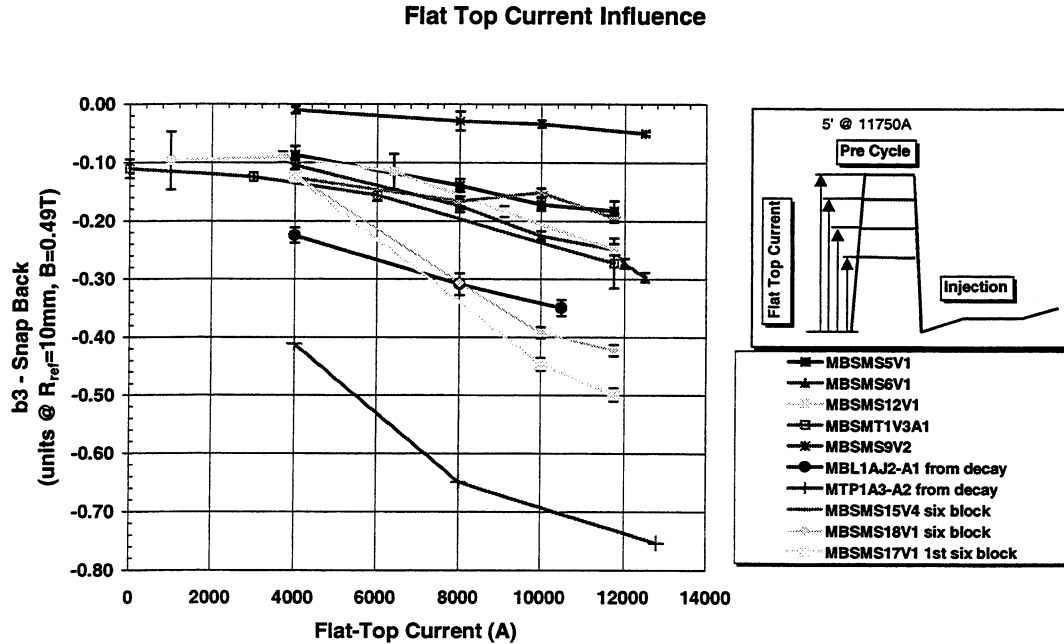


Figure 5.9: The Pre-Cycle Flat Top Current influence on the snapback of several one-meter long LHC dipole model magnets using the old five block design is comparable to the newer six block design models. The general trend also exists in case of a 10-meter long dipole model and a 10-meter long prototype of the old 50-mm aperture magnet.

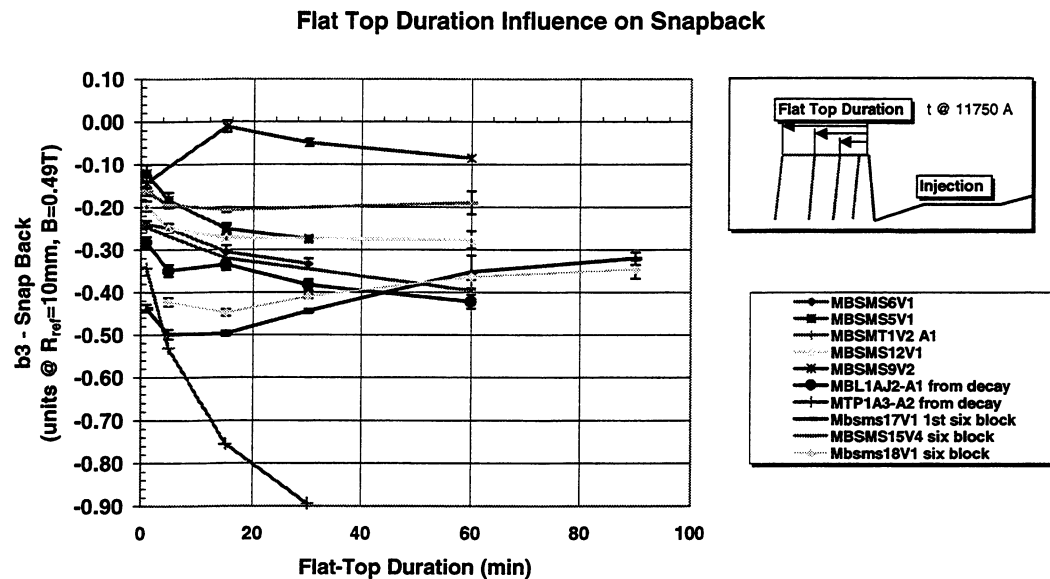


Figure 5.10: Pre-Cycle Flat Top Duration influence on the sextupole snapback for groups of five-block and six-block design magnets.

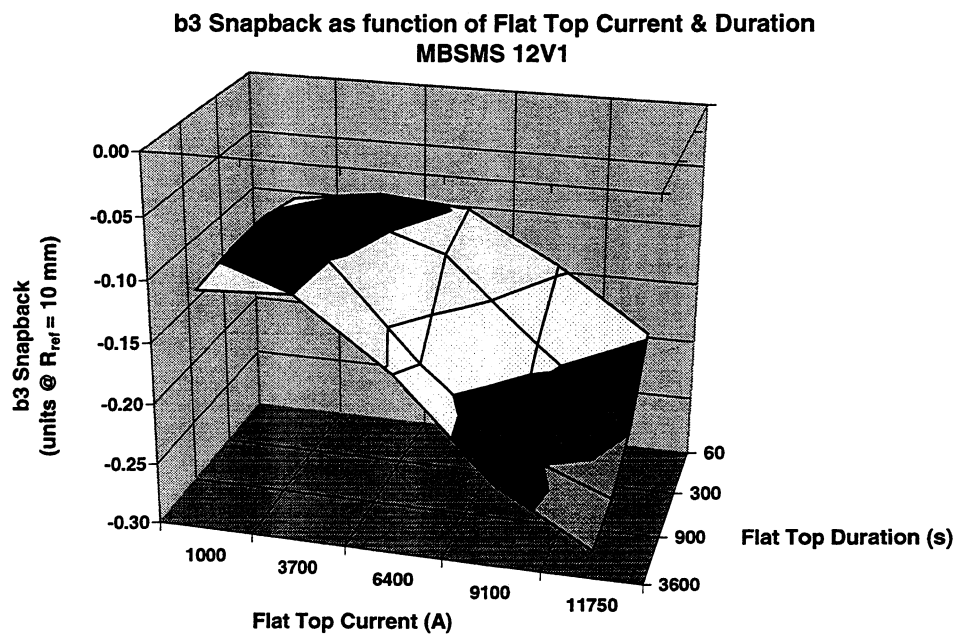


Figure 5.11: 3D plot of the sextupole snapback surface of the one meter long LHC dipole model magnet MBSMS12V1. The extent of the snapback is a function of the Pre-Cycle Flat Top Current and Duration.

Flat Top Current Influence

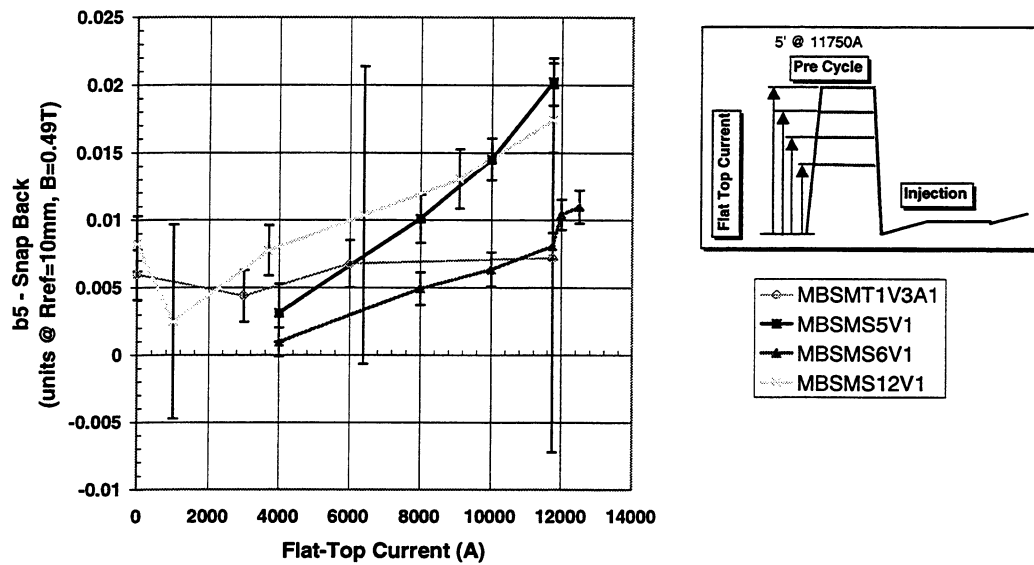


Figure 5.12: The Pre-Cycle Flat Top Current influence on the snapback of several one-meter long LHC dipole model magnets (five block design) shows the expected systematics for b_5 .

Flat Top Current Influence

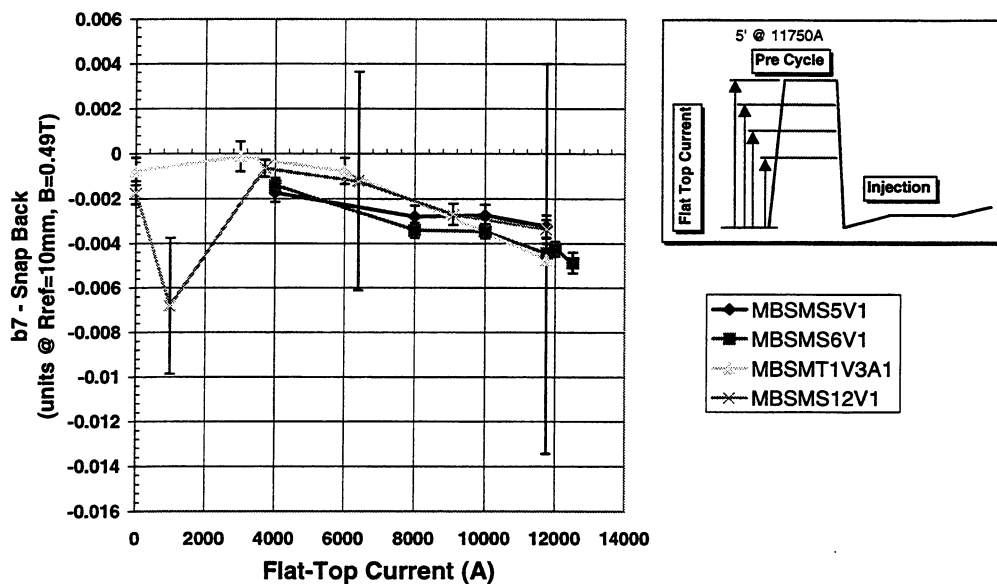


Figure 5.13: The Pre-Cycle Flat Top Current influence on the snapback of several one-meter long LHC dipole model magnets (five block design) shows the expected systematics for b_7 .

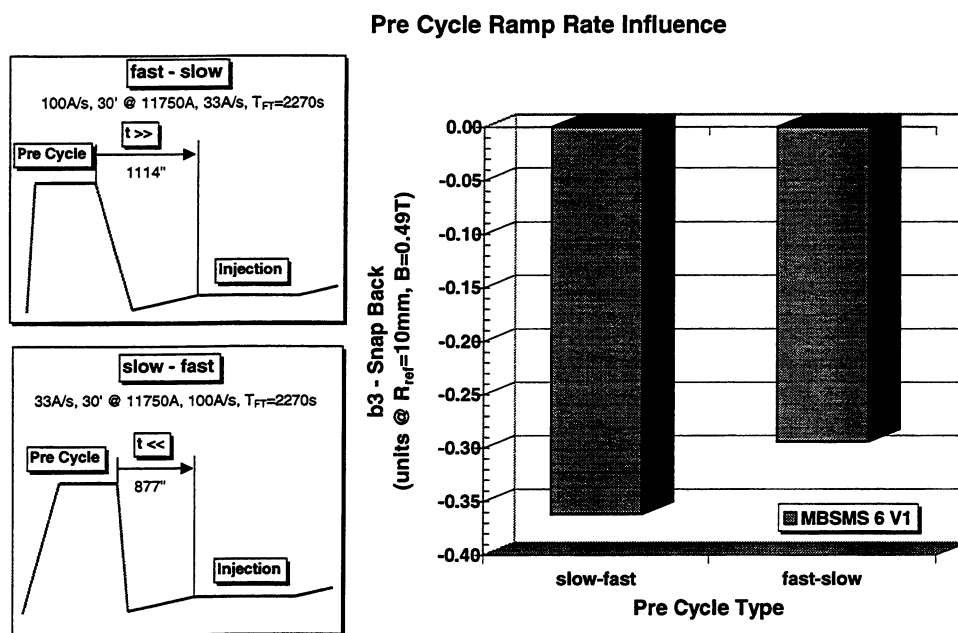
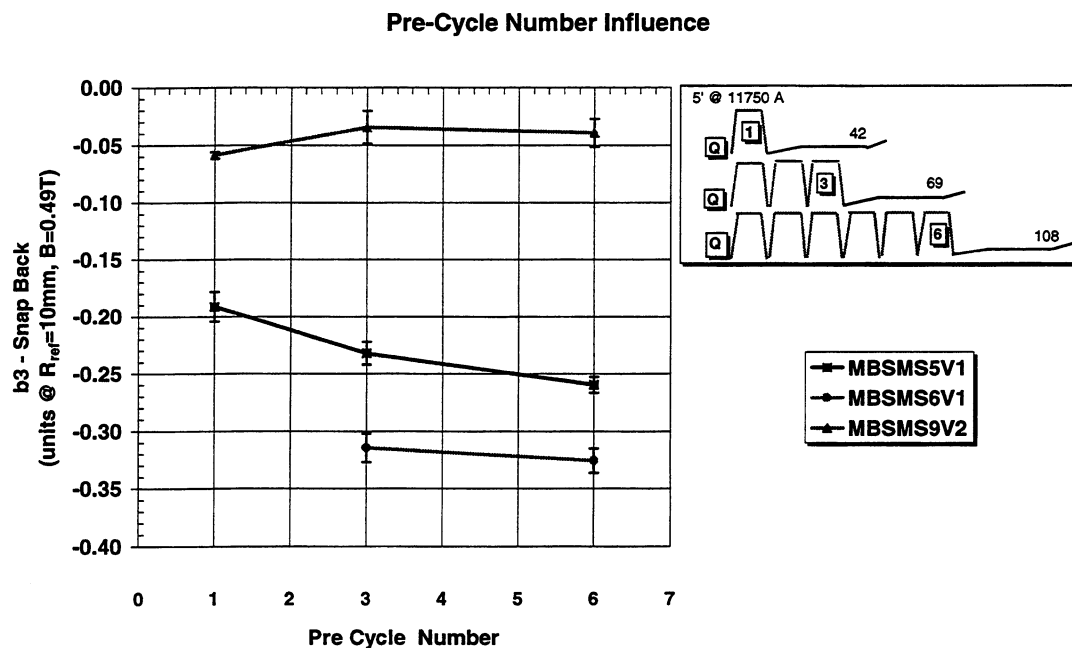


Figure 5.14: Pre-Cycle Ramp Rate influence on the sextupole snapback of the MBSMS6V1 one meter long LHC dipole model magnet.



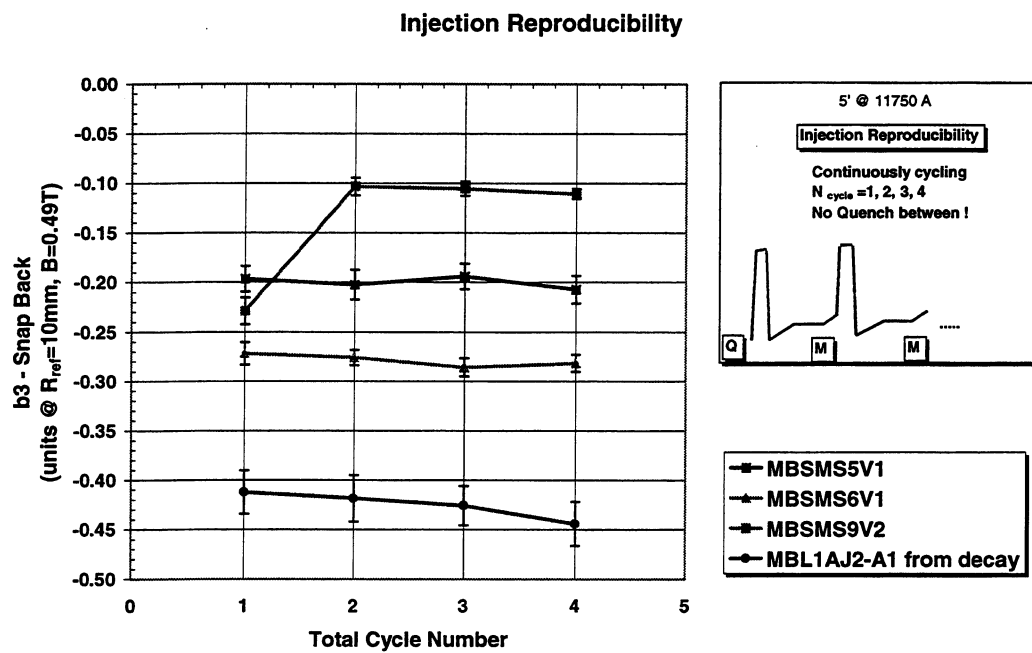


Figure 5.16: Multiple operation cycle (Injection Reproducibility) influence on the sextupole snapback of three one meter long MBSMS series magnets and one 10-meter long dipole model.

6. Modeling of Snapback

From a first point of view a simple parameterization of the results of snapback measurements, which we showed in Figure 5.6 to Figure 5.16, with polynomial functions could be a possible way of modeling the snapback behavior of the LHC dipole model magnets. But this technique would reach its limitations very soon. One should not forget that our parameterization would only work if one operation cycle parameter was varied and the other parameters were kept constant. This is indeed true because we have measured the curves under this condition; thus the parameters of the polynomial function are only valid for this particular situation.

Unfortunately we have to consider more complex powering conditions during real world operation of the magnets inside the accelerator complex. For example let us imagine that for some reason the beam must be aborted during the acceleration when the magnet is powered to an excitation current of 6195 A. What are we supposed to do with the magnet system in this situation? In principle we have three possibilities to reestablish well-known conditions.

In the first scenario we power the magnets up to nominal current and stay there longer than the saturation time constant we found in Figure 5.10 suggests. This would last maybe 1.5 hours for the one-meter long LHC model magnets and most probably much longer for 15 meter long real size dipoles. After this waste of time it should be possible to re-inject particles into our machine under well-controlled conditions.

Another possibility is a procedure, which was established for Tevatron injection. Six pre-cycles were used to erase machine history effects on the field component decay during injection. Under LHC conditions, with a maximum specified ramp speed of 10 A/s and nominal current of 11750 A, we would waste approximately four hours with cycling.

The third and most interesting alternative would be to ramp down the magnet immediately after beam dump and restart the injection procedure. This would provide the most efficient use of the accelerator. But therefore we need to know the state of our magnet system as function of arbitrary operation cycle situations with very high precision.

In order to predict the snapback amplitude as function of the operation cycle parameter variation with sufficient accuracy a reliable and consistent model is required. This chapter shows two different ways to scale snapback. One model is based on a phenomenological parallelism between the magnet behavior and a simple RL-circuit. The other model has the ability of modeling snapback as function of operation cycle variations by use of artificial neural networks (ANNs). In order to define the most reliable procedure we derive results for both approaches and compare these with the measurements.

6.1. The Analytical Operation Cycle Model

The empirical model is based on the simple assumption that the allowed field component decay at the end of the injection phase respectively snapback at the beginning of the acceleration phase must be somehow related to the decay of the so-called boundary induced coupling currents, BICCs [76], or supercurrents [77]. Due to the electromagnetic properties of the Ruhfurd-type cable the amplitude of this current imbalance during the operation is assumed to be proportional to the charging and discharging of a RL-circuit at

a certain time during the operation cycles. This circuit is charged during the ramp and discharged during constant transport current excitation. Taking the recent operation history in account and computing the actual current amplitude at the end of the injection plateau leads to a value proportional to the sextupole snapback.

The functional relation between operation cycle variations and snapback is given by Equations 6.1 and 6.2. It must be stated that the formalism applied here is in close connection with the current diffusion model of the two-wire Rutherford type cable simulation of L. Krempasky. But in contrast to this model, where the current imbalance in the two-wire model is given by a sum over current component, each of them linked to a time constant, we approximate the problem with only one amplitude and time constant. Thus our proposal can be seen as a first order approximation of Krempasky's current diffusion model.

$$f_i = \begin{cases} \dot{B}_i (1 - e^{-\frac{\Delta t_i}{\tau}}) e^{-\frac{\sum_{n=i+1}^m \Delta t_n}{\tau}} & \dots \quad \dot{I} \neq 0 \\ 0 & \dots \quad \dot{I} = 0 \end{cases} \quad (6.1)$$

The function f_i in Equation 6.1 is a representative of the current amplitude in a Rutherford type cable, which is established during a charging period in the operation cycle sequence of the duration Δt_i . The amplitude then decays during the following operation cycle sequences. This decay lasts over the total sum of time intervals Δt_n . The sum over all Δt_n characterizes the total duration of the following operation cycles. When different charging cycles are present during the operation cycle sequences the sum in Equation 6.2 includes the superposition of all amplitudes (see Equation 6.2) at a certain moment in the operation cycle history. This moment is usually the end of the injection plateau, where the maximum decay is observed. The snapback at this time ($t = 1020s$) is then given by:

$$SnapBack = \frac{\left| \sum_{i=0}^m f_i \right|}{Scale} + Flux \ln(1020), \quad (6.2)$$

obtained by scaling the amplitude of the currents f_i . Here m is the total number of cycle sequences. The scale factor takes the relation between current and magnetization changes into account, as well as the effect of a change of magnetization on b_3 . The Flux parameter describes the contribution of the flux creep to the b_3 decay. The three model parameters called τ ($=$ Time Constant), $Scale$ ($=$ scaling factor) and $Flux$ ($=$ Flux Creep parameter), were derived by fitting Equation 6.2 to the total available set of snapback measurement results for each magnet. A summary of these parameters for all the magnets used for the phenomenological modeling experiment, is shown in Table 6.1.

Apart from magnet number MBSMS12V1, which shows slightly reduced values, the model parameters show a relatively stable behavior. A clear correlation between the flux creep associated parameter and the sextupole hysteresis width cannot be observed.

The computed operation cycle influence on sextupole snapback is shown in Figure 6.3 to Figure 6.8. The simulations are labeled *ANALYTIC*.

Table 6.1: Model parameters derived by fitting Equation 6.2 into the total available number of snapback measurements.

Magnet	τ	Scale	Flux	Hysteresis @ B=0.54 T
Name	s	1/units	% / decade	units
MBSMS5V1	696	-4.25E-03	-0.26%	4.84
MBSMS6V1	690	-4.11E-03	-0.40%	5.91
MBSMS12V1	439	-9.26E-04	-0.17%	5.58
MBSMT1	595	-1.80E-03	-0.22%	6.45
MBL1AJ2-A1	595	-2.56E-03	-0.46%	6.5

6.2. The Neural Network based Snapback Model

6.2.1. Design and Training

The snapback prediction was performed using a three-layer perceptron. Six input neurons, twelve elements in one hidden layer and one output neuron form the network structure shown in Figure 6.1. The transfer function in our experiment is a hyperbolic tangent, which transforms from $\mathbb{R} \Rightarrow [-1, +1]$. The number of input neurons and output neurons is usually fixed by the abstraction of the physical system, while the number of neurons in the hidden layer is mostly a matter of trial and error. The number of hidden layers cannot be strictly determined either. Many applications of neural networks show sufficiently good results by using only three or four layers in total [85, 84].

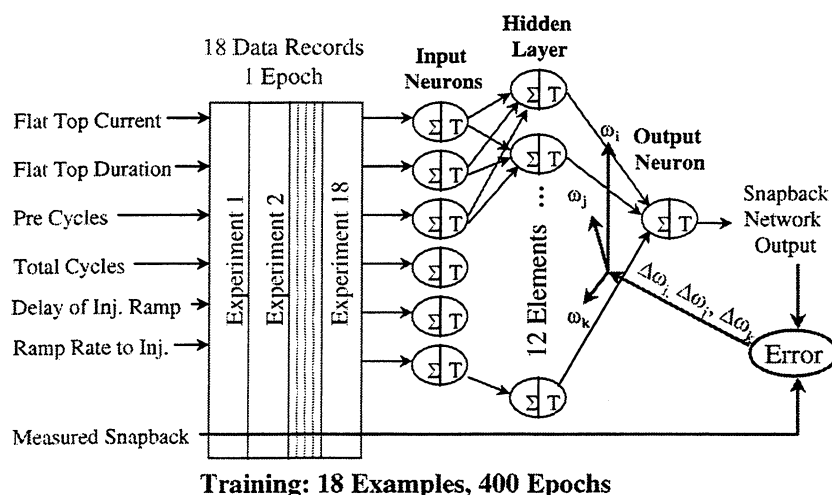


Figure 6.1: The artificial neural network experiment for MBSMS5V1 was performed on a basis of 18 Examples (measurements). Each example consists of a variation of one of the input parameters and one snapback value. The training of the network requires 400 Epochs (training cycles).

In order to apply a neural network to our problem, the standard operation cycle (see Figure 5.1) is divided into a serial sequence in time, namely Pre-Cycle Flat Top Current, Pre-Cycle Flat Top Duration, Number of Pre-Cycles, Number of Operation Cycles, Delay of Injection Ramp and finally the Injection Ramp-Rate. The standard operation cycle and

its sequences are shown in Figure 5.5. Its parameters respectively the variations of the parameters are reported in Table 5.4.

The operation cycle abstraction is then applied to the input neurons in form of a parallel input vector. The three-layer perceptron transforms this six-dimensional vector into a snapback value. After a successful training, the network provides an accurate map from $\mathbb{R}^6 \Rightarrow \mathbb{R}^1$ within the range of applied operation cycle variations.

The training of the network is based on 18 available snapback measurements on the short one-meter long LHC dipole model magnet MBSMS5V1. These measurements are called examples. We applied 400 epochs of these examples to the network. This procedure provided an optimal training performance. The mean-square error (MSE) (see Figure 6.2) asymptotically reached its minimum in the last training epoch. Thus the final network weights were stored for the following prediction experiments. Details about the software we used to perform the experiments can be found in the reference list [96].

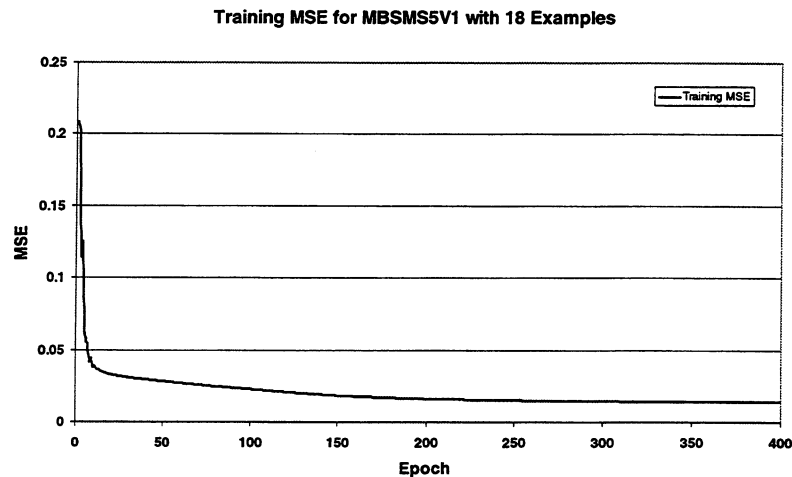


Figure 6.2: The Mean Square Error of the training process for the ANN drops significantly within the first few Epochs and reaches its final value asymptotically after 400 Epochs.

6.2.2. ANN response to Operation Cycle Variations

Results of the experiments, which are labeled NEURON in Figure 6.3 to Figure 6.8, generally show a very good agreement with the measured results in the range of parameter variations. Even if we extend the parameter variations for the Pre-Cycle Current to lower values than trained (Figure 6.3) we find the typical flat convergence towards a value of approximately -0.1 units, which we also find in several measurements for other short LHC dipole model magnets.

In contrast to this highly successful generalization there is a very unlikely saturation for Pre-Cycle Current values towards 12000 A, which is shown in Figure 6.3. This behavior must be due to the deviation of the measurement from the typical straight behavior for Pre-Cycle Currents above 4000 A (see Figure 5.9).

During the Pre-Cycle Number experiment (Figure 6.5) we observed another interesting detail in the network response. The snapback prediction for a fictive operation cycle without Pre-Cycle (zero value on the Pre-Cycle Number input neuron) does not lead to

the expected value if we do not set the Pre-Cycle Current and Pre-Cycle Duration network input to zero. But in fact, this input vector represents a non-physical parameter combination. The network response must be wrong, because the parameter combination does not exist in reality. Thus such non-physical combinations of parameters must be avoided. Another difference between the measurement and the network response, slightly larger than derived from the analytical model, was observed during the experiment for one single Pre-Cycle. But in fact, the network presents only the average of all available measurements. The particular value measured for the Pre-Cycle Number experiment with one Pre-Cycle is slightly higher than the average value.

Another dangerous situation can be deduced from the result of the Ramp-Rate to Injection experiment (Figure 6.7). In this case we observed a strong deviation from the desired output for the ramp rate value of 1 A/s. But if we study the operation cycle sketch in Figure 5.5, the wrong interpretation by the network is not difficult to understand. During the design phase of this operation cycle we decided to keep the duration between the end of the Pre-Cycle ramp and the beginning of the injection ramp constant. Comparing this with the first definition of the input neurons we immediately saw that the variable describing the delay between the end of the pre-injection ramp and the injection ramp is missing. The network was exposed to a specific situation during the training phase. Apart from the 0.5 A/s and the 2 A/s measurements, all other experiments were performed with the standard value of 1 A/s. Deduced from these measurements, which led to values of around -0.18 units, the network learned to predict -0.175 units. This is exactly the average value of all the available measurements performed at 1 A/s.

Due to the missing parameter concerning the delayed beginning of the injection ramp the measured value of -0.12 units during the Ramp-Rate to Injection experiment was obviously interpreted as a statistical fluctuation of a total number of 5 measurements at 1 A/s included in the training data set. The other two Ramp-Rate to Injection experiments (0.5 A/s and 2 A/s) are perfectly reproducible by the network response. This is due to a lack of information from the standard cycle measurements, where no other ramp rate than 1 A/s was measured.

Finally we performed a correction of the input structure of the network. The missing input neuron, representing the delay between the end of the pre-cycle ramp and the beginning of the ramp to injection, was added. Consequently the discontinuity in the network response disappeared. The snapback prediction with the help of the corrected network structure for different ramp rates to injection is shown in Figure 6.8.

Another apparent network response error was observed during the total cycle number experiment (Figure 6.6). We observed a significantly reduced snapback value in comparison to the actual measurement for one Pre-Cycle. But it can again be verified that the network response is caused by the averaging of all the measurements performed per default with only one Pre-Cycle. Thus the neural network performs precise average calculations.

6.2.3. ANN as an Averaging Tool

Based on the experience of the averaging properties during the last experiment we performed a second experiment of interest for series measurements. We wanted to see if dynamic effect prediction can be performed with neural networks during a standard accelerator operation in case of magnets with a small difference in their field dynamics

behavior. The three-layer perceptron described above was slightly modified. The number of input neurons was reduced from six to two according to the available input parameters, which were Pre-Cycle duration and current. We used the total set of variations of Pre-Cycle Current and Duration for the short LHC dipole model magnets MBSMS 5V1, 6V1, 12V1 and MBSMT 1V3 aperture 1, and trained the network to predict snapback. The result of this experiment is shown in Figure 6.9 and Figure 6.10. This experiment proves that the network is able to work as a nonlinear interpolation machine in case of measurements obtained from magnets, which show very similar field dynamics. This is exactly the situation we are confronted with during the pre series measurements as well as during the series measurements. Due to a number of different magnet producers using different cables from a number of different cable producers we expect to find typical distributions of decay and snapback, which are characteristic for each magnet production series. This result was already observed at HERA, where two different producers built the main bending dipoles [45].

6.3. Results and Discussion of modeling

The analytical results derived from the simple model are quite good as long as the prediction of snapback within an accuracy of maximum + 40 % of relative error and a typical error of ± 30 % is concerned.

In case of the *flat top current* experiment (Figure 6.3) the maximum relative error occurs at 4000 Ampere. This is due to the fact that the model function (see Equation 6.2), which contains an absolute value computation, can only roughly estimate the smooth approach towards - 0.1 units of snapback for 0 A of flat top current.

The situation is significantly better in the *flat top duration* experiment (Figure 6.4). Again the maximum error appears for low *flat top duration*. But the relative error is approximately - 20 %.

The functional approximations for the Pre-Cycle Number experiment (Figure 6.5) seem to be significantly better than the neural network response. But this is not really a property of the model; instead we have to remember the explanation of the averaging ability in case of the ANN approach. Thus the total performance of the empirical model is below the ANN prediction quality.

The *injection reproducibility* experiment (Figure 6.6) shows similar results. Results of measurements, which were carried through only once (2, 3, 4 total cycles), are of better accuracy than the measurement results obtained for one pre cycle. Again we have to refer to the averaging property of the ANNs.

In contrast to the above-observed proper approximations of snapback measurements the analytical model response is completely wrong in case of the *ramp rate to injection* experiment (Figure 6.7). Not only the higher relative error is obvious, but also the trend is wrong.

6.4. Conclusion of snapback modeling

In this chapter we proved on the one meter long LHC model magnet MBSMS5V1 that the three layer perceptron can reproduce and extrapolate the nonlinear behavior of snapback due to operation cycle variations more successfully than a simple phenomenological model. Attention must be paid to a useful combination of values applied to the input neurons. Using the measurement results obtained during the pre

series and series measurements in order to train a neural snapback prediction network for future use during standard accelerator operations, requires an exact definition of a standard cycle before starting these measurements. This standard cycle must consist of exactly the same sequences, which are used in the standard machine operation cycle. Each sequence, which might be a subject of operation cycle variation, can then be defined as an input neuron.

Furthermore a successful test of the non-linear approximation ability of the neural network was performed for a group of four short LHC dipole models. In comparison to the empirical model and in case of different dipole producers the averaging behavior of the neural network might be of high interest because of the more accurate approximation of the strongly non-linear snapback dependence on operation cycle variations.

The empirical model is not based on a solid physical background of the superconducting dipole magnet and therefore provides only a poor description of the snapback behavior. The fit quality is due to the limitation caused by the combination of functions, which were used to model the system behavior. The intuitive approach of combining RL circuit charging and discharging with flux creep leads to a prediction quality with $\pm 30\%$ of relative error.

On the other hand the neural network does not provide information about the possible physical behavior of the dipole magnets. But the network successfully learned the typical nonlinear mapping between input (operation cycle sequences) and output (snapback) of the observed physical system from a small number of measurements. Thus the prediction quality can be significantly increased up to $\pm 10\%$ of relative error. The quality of snapback prediction derived by using the neural network is always better than the error bar of our measurements.

Based on this experience a neural network approach for snapback and decay prediction that may be included in a correction system control unit seems to be a possible scenario for the LHC acceleration operation.

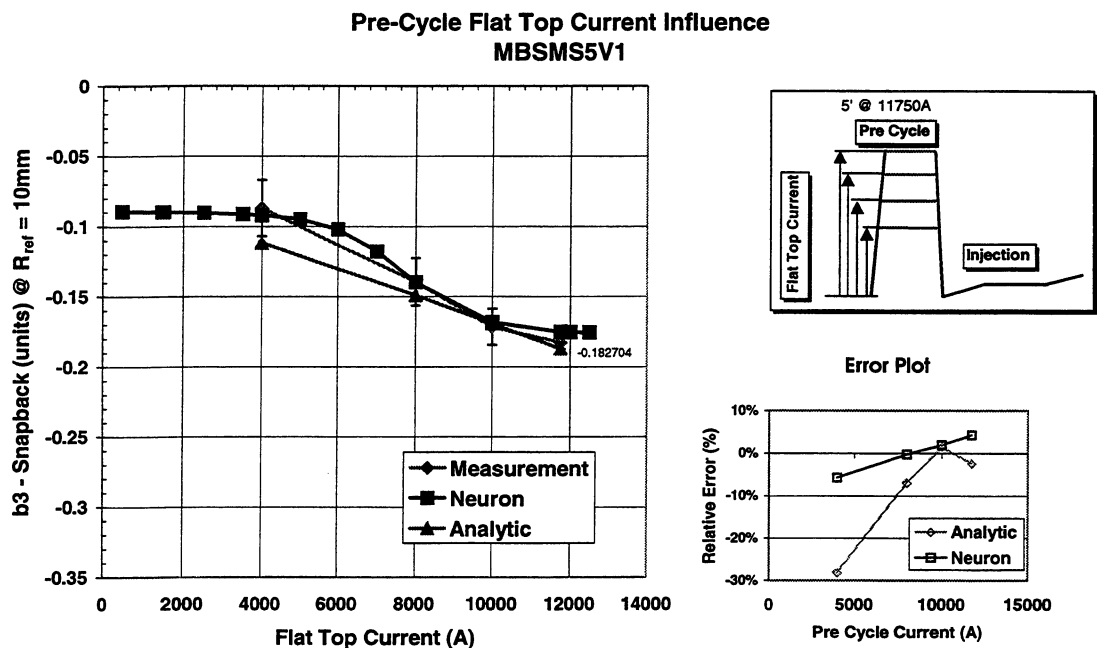


Figure 6.3: Pre-Cycle Flat Top Current Influence for MBSMS5V1. The neural network derives a more smooth approximation of the measured snapback values between 4000 A and 11750 A. Predicted values below 4000 A show the typical saturation towards -0.1 units.

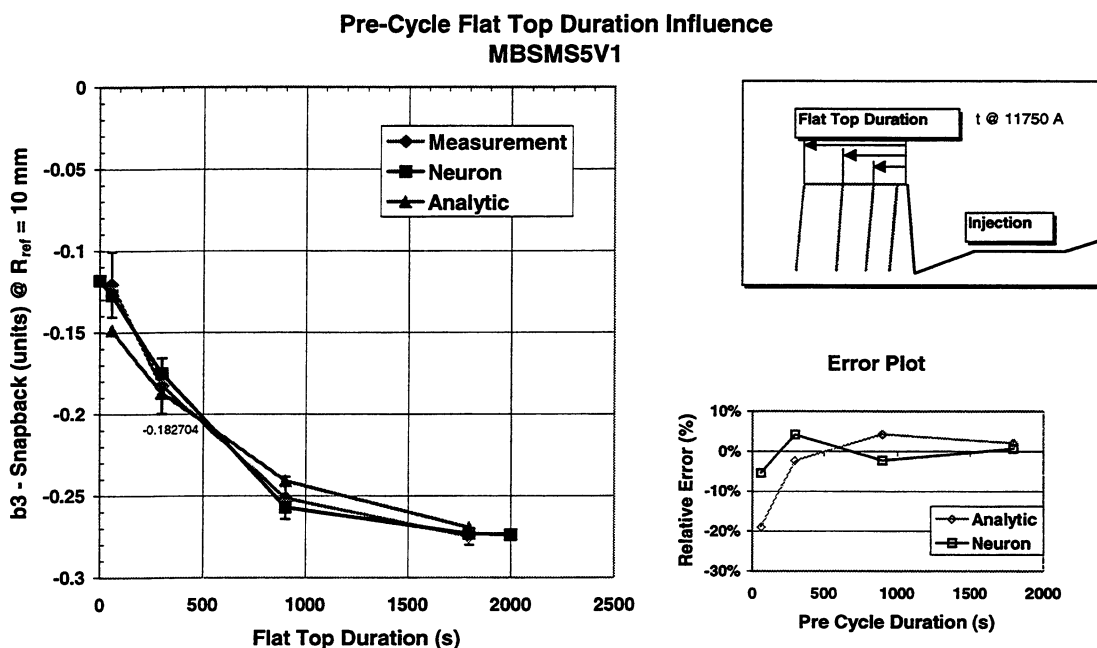


Figure 6.4: Pre-Cycle Flat Top Duration Influence for MBSMS5V1. The analytical as well as the neural network approach approximate the measurements correctly. The neural network derives a better accuracy for a very short pre-cycle duration.

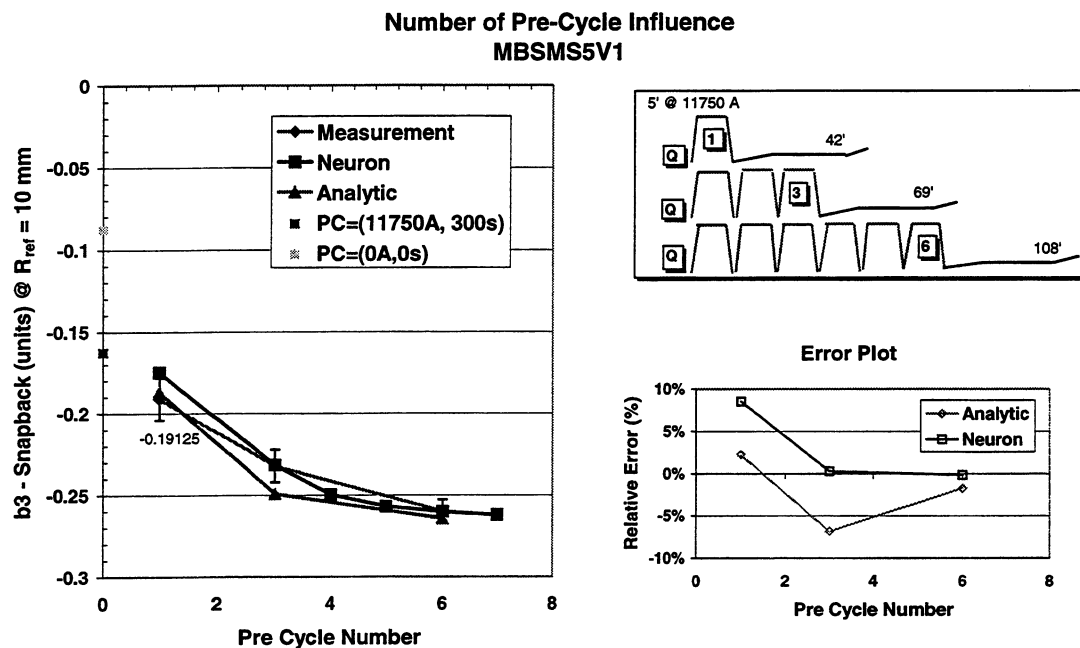


Figure 6.5: The Multiple Pre-Cycle experiment shows a fast saturation after a few numbers of pre cycles. This behavior is accurately reproduced by the ANN as well as by the empirical model. The deviation at the first total cycle is due to the averaging property of the ANN.

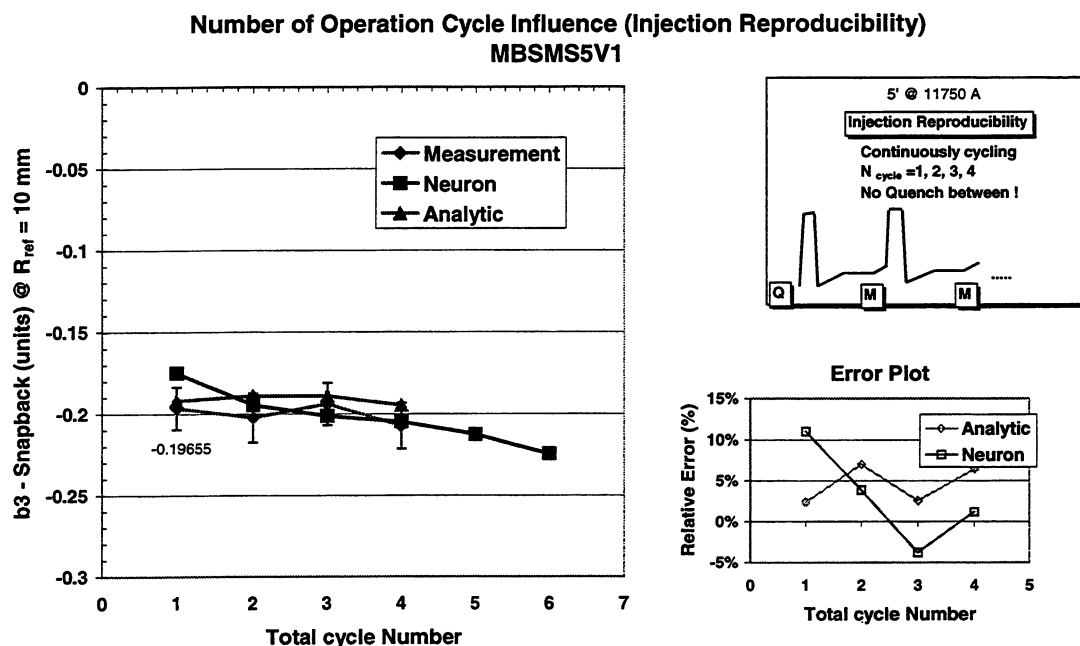


Figure 6.6: Multiple Operation Cycle Influence for MBSMS5V1 (Injection Reproducibility Experiment). A continuous cycling of the magnet reveals a stable appearance for snapback at the end of injection (injection reproducibility). The neural network as well as the analytical model derives comparable values with an acceptable accuracy. The deviation at the first total cycle is due to the averaging property of the ANN.

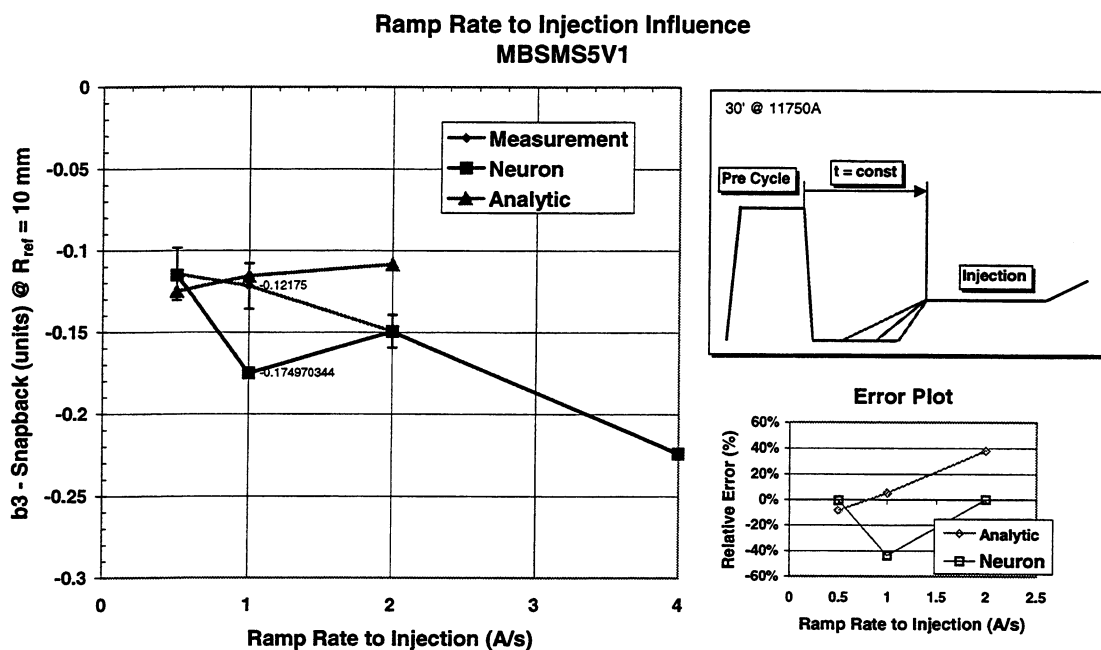


Figure 6.7: Ramp Rate to Injection Influence for MBSMS5V1. The apparently wrong prediction for the 1 A/s measurement is due to a missing input neuron representing the duration of delay between the end of the pre cycle and the ramp to injection.

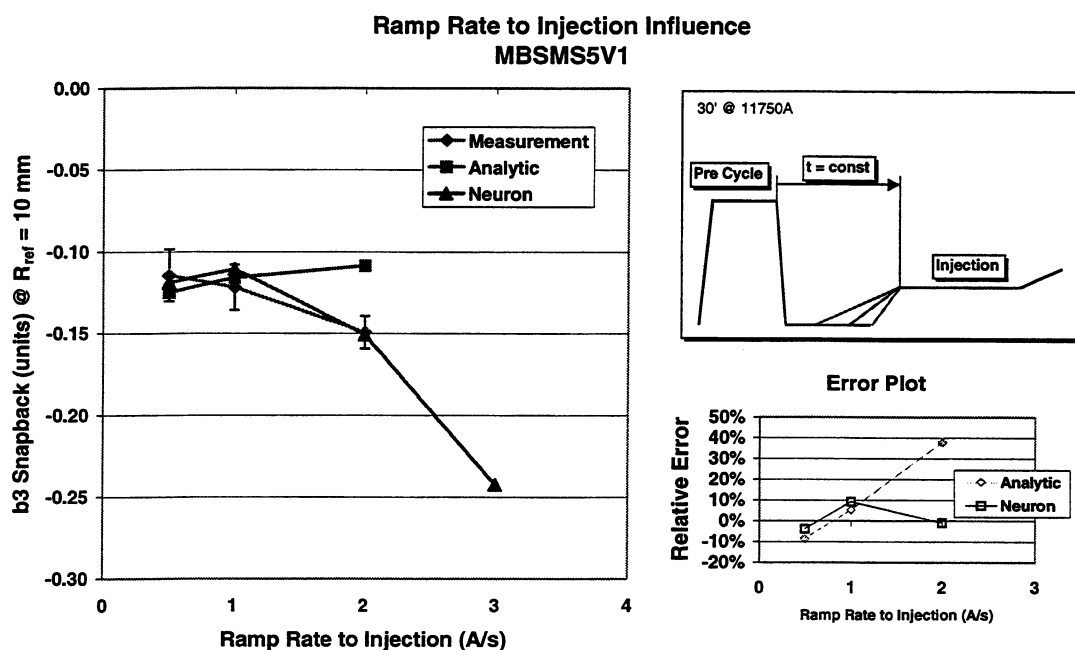


Figure 6.8: Ramp Rate to Injection Influence - Corrected. The corrected network structure derives accurate tendencies. The analytical model shows an obvious problem for these kinds of operation cycle variations.

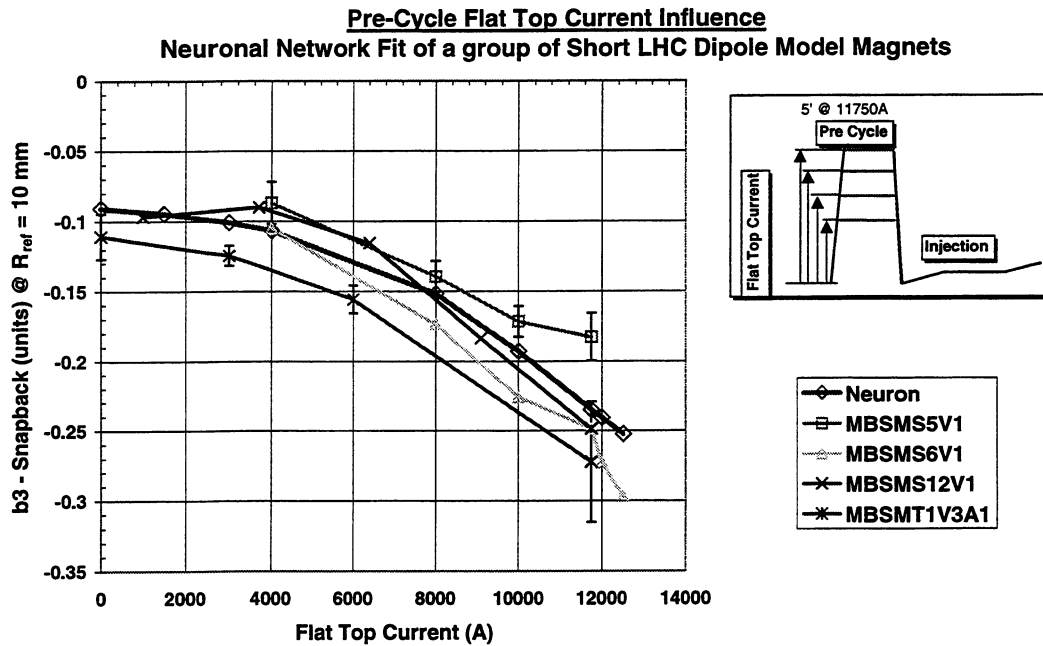


Figure 6.9: Flat Top Current Influence for a group of short LHC dipole model magnets. The neural network was trained to estimate the snapback behavior for a group of similar short LHC dipole model magnets. We performed the training with all-available flat top duration and current measurement results.

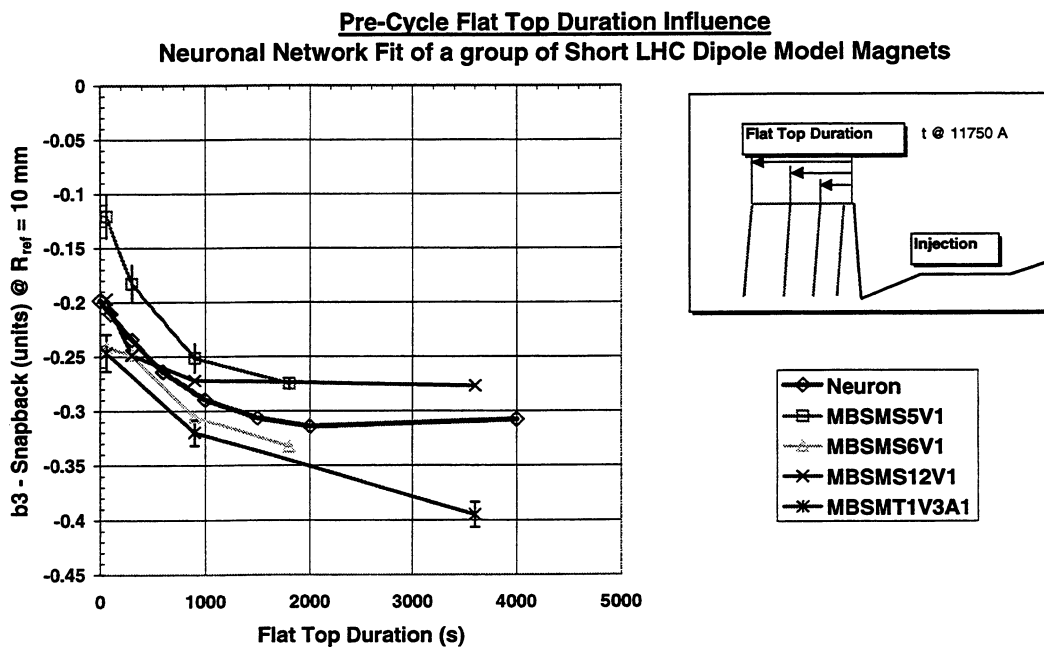


Figure 6.10: Flat Top Duration Influence for a group of short LHC dipole model magnets. Similar to the equivalent experiment for Flat Top Current the neural network works as a "neural averaging machine".

7. Application to Series Measurements

One of the fundamental decisions to be made in the LHC project concerns the number of magnets that must be measured in *cold* conditions. As opposed to *warm* measurements, cold measurements are time consuming and require cryogenic equipment, thus affecting both budget and time scale. For this reason it is advantageous to limit the number of magnets measured cold. On the other hand warm measurements do not provide information on the superconducting features of the magnet, including decay and snapback. As the LHC is critically dependent on the knowledge of both effects, we try to use a statistical simulation to establish the minimum number of magnets that must be fully characterized *at cold*.

One aspect concerning the problem of choosing a proper number of magnets is determined by chromaticity requirements for the LHC. During the injection the chromaticity must be corrected to a scatter of about 1 to 5 units. For the LHC we know that a change of 1 unit of sextupole results in a change of 150 units of chromaticity. From this we derive the bounds for our sextupole accuracy, which are given with $\Delta b_3 = 6.66 \cdot 10^{-3}$ units for 1 unit of change in chromaticity and $\Delta b_3 = 3.33 \cdot 10^{-2}$ units for 5 units of change in chromaticity. The required sextupole accuracy must now be seen in relation to the actual mean of sextupole snapback, which is given with $-2.74 \cdot 10^{-1}$ units @ $R_{\text{ref}} = 10\text{mm}$. Based on this mean we derive a required accuracy of sextupole control of 2.4 % in case of the lower bound of chromaticity and an accuracy of 12 % in case of the upper bound. Based on these two numbers statistical methods provide a good tool to derive the required number of magnets.

Another aspect of the problem is the required time to perform a full characterization of the snapback behavior of the LHC dipole magnets. The details of the measurements for the full characterization are listed in Table 5.4. From the present point of view it will be necessary to scan the Pre-Cycle Flat Top Current and Duration surface as shown in Figure 5.11 for all magnets involved in the full characterization. But the magnetic measurement time for this full characterization for only one magnet would last at least 40 hours and approximately the same duration for the quench and consecutive cool down to 1.8 K of operation temperature. Performing this full characterization on all magnets would by far exceed the time horizon of starting the LHC's operation. Thus only a fraction of magnets can be used for a full characterization.

7.1. Basic Considerations

At first let us observe a small sample of one-meter long LHC model magnets, which were involved in the Pre-Cycle Flat Top Current experiment (see Figure 7.1) above 4000 A. These are MBSMS5V1, MBSMS6V1, MBSMS12V1, MBSMT1V3 aperture 1, MBSMS9V2, MBSMS17V1 (first one meter long single aperture six block design model). We actually mix single aperture, twin aperture model magnets and the five-block and six-block design. But we have a good reason for doing so.

The group of magnets we have chosen constitutes the worst case for flat top current variations above 4000 A. We see magnet MBSMS9V1 that evolves very flat in comparison to magnet MBSMS17V1 that has the maximum slope. Thus we assume that the standard deviation of the mean describing the flat top behavior of our theoretical population must be embedded within 3σ , which is determined by the bound of

MBSMS9V1 and MBSMS17V1. These magnets define the worst case solutions of snapback measurements.

During the Pre-Cycle Flat Top Current experiment we observed a second fact. Most magnets show a very flat snapback behavior below 4000 A. It looks like BICCs or supercurrents play a minor role and another effect is dominant below 4000 A. This effect could be related to thermally activated flux creep. Flux creep is an intrinsic property of the superconducting material. A normal distribution of snapback seems to be a correct assumption for flat top currents below 4000 A.

Due to these considerations we decided to compute a reliable mean of snapback values at 0 A with a certain sigma. Starting from 0 A of flat top current a scaling law generates snapback measurements for 1500 A, 3000 A, 4000 A, 8000 A and 11750 A of flat top currents for the total population of 1232 magnets. These data provide the base for the sampling experiments.

7.2. The Parameterization

The parameterization starts by performing an ANN fit of a group of magnets, which were involved in the Pre-Cycle Current experiment. The ANN fit derives a mean snapback of -0.235 units at 11750 A. Comparing this mean with the mean of the total number of 18 one-meter long LHC dipole models reveals an offset of 0.039 units. Thus the ANN fit was shifted by this value. The functional dependence is reproduced with good accuracy by Equation 7.1.

$$b_{3, \text{Snapback}}(I_{\text{FlatTop}}) = C - 1 \cdot 10^{-9} I_{\text{FlatTop}}^P \quad (7.1)$$

The parameters of this fit are C , which determines the snapback value for 0 A of the Pre-Cycle current, and P , which is the exponent of the non-linear scaling of snapback due to Pre-Cycle current variations. Fitting Equation 7.1 to the measured snapback values of the magnets that were mentioned in the previous section, leads to a set of numbers like the mean of C , its standard deviation and the mean of P and its standard deviation. These numbers are shown in Table 7.1. The measured snapback dependence on Pre-Cycle current variations for this group of magnets is shown in Figure 7.1.

Table 7.1: Basic parameterization of five sample magnets in the Pre-Cycle Flat Top Current experiment.

<i>Magnet</i>	<i>Parameters</i>	
	<i>C [units]</i>	<i>P</i>
MBSMS5V1	-0.0809	1.9768
MBSMS6V1	-0.0891	2.0261
MBSMS12V1	-0.0808	2.0194
MBSMT1V3 ap.1	-0.1130	2.0155
MBSMS9V2	-0.0461	1.6903
MBSMS17V1	-0.0946	2.1220
<i>Mean</i>	-0.0841	1.975
<i>Standard deviation</i>	0.022	0.1472

The mean of C is no longer of interest, because of the above-mentioned shift of the ANN fit, which fixed this value to -0.130 units. The mean of parameter P represents the exponent derived from fitting Equation 7.1 to the ANN fit ($P=2.00$), also with good accuracy.

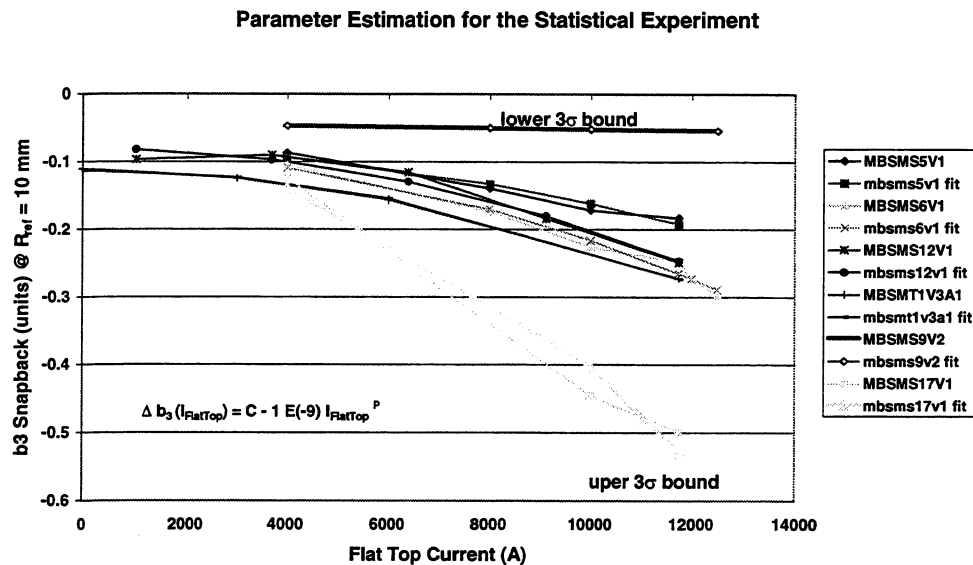


Figure 7.1: Definition of the three-sigma bounds for the statistical simulation experiment.

The standard deviations of both parameters must be representative for the 3 σ bound of the mean value in order to determine magnet MBSMS9V2 and MBSMS17V1 as worst case magnets. Thus we verified that a mean of 0.022 in case of parameter C is a good measure of a 3 σ bound. But the standard deviation of parameter P was reduced to 0.0492 by a factor of 3. The final parameters are shown in Table 7.2.

Table 7.2: Final parameter for the statistical simulation of the Pre-Cycle Flat Top Current experiment for a population of 1232 one meter long LHC dipole model magnets.

	Parameters	
	C [units]	P
Mean	-0.130	1.975
Standard deviation	0.022	0.0492

7.3. The Population

The parameter C and its sigma from Table 7.2 finally allowed us to generate a normal distribution of the snapback of a population of 1232 one-meter long LHC dipole model magnets at 0 A of the Pre-Cycle current. Furthermore a normal distribution of 1232 exponents P was generated. Each exponent characterized the Pre-Cycle flat top current influence on snapback for one particular magnet. Applying C and P of each of the 1232 magnets as input for Equation 7.1 generates snapback measurements for 1500 A, 3000 A, 4000 A, 8000 A and 11750 A of Pre-Cycle flat top currents. This population was the base for the sampling experiment. But before we performed the statistical experiment we derived so-called reference mean values for all seven operation currents in order to compare them with the mean values of samples with varying sample size.

Apart from that we were interested in a statistical description of the development of the originally normal distribution of the snapback values from 0 A up to 11750 A of the Pre-Cycle flat top current. *Kurtosis* and *skewness* of the distributions were computed for this

characterization. The skewness characterizes the degree of asymmetry of a distribution around its mean. It is a number that describes the shape of the distribution. The kurtosis is also a non-dimensional quantity. It measures the relative peakedness or flatness of the distribution in comparison to a normal distribution. The mean, standard deviation, kurtosis and skewness values for our experiment are shown in Table 7.3.

Table 7.3: Analysis of the evolution of the distribution of the population of one meter long LHC dipole model magnets when performing a non-linear Par-Cycle Flat Top Current simulation.

Parameter	Par-Cycle Flat Top Current						
	0 A	1500 A	3000 A	4000 A	8000 A	10000 A	11750 A
Mean	-0.1309	-0.1329	-0.1389	-0.1451	-0.1877	-0.2196	-0.2533
Standard Deviation	0.0193	0.0193	0.0195	0.0201	0.0322	0.0458	0.0617
Kurtosis	-0.0197	-0.0019	0.0389	0.0552	0.9204	1.7567	2.2797
Skewness	0.08799	0.09663	0.1205	0.1189	-0.5636	-0.9372	-1.1303

The numbers clearly show that the originally normal distribution of snapback turned into a relatively flat distribution hanging to the left under the influence of the non-linear flat top current scaling law. This is visualized by plotting the frequency versus snapback value for each of the flat top currents. This way of analyzing the distributions showed that the standard deviation is relatively stable up to 3000 or 4000 A. But the sigma increases dramatically above 4000 A. Observing the parameters kurtosis and skewness revealed that the distribution deviates significantly from a normal distribution in the current range above 4000 A. Thus we conclude that the application of statistical methods, which are based on a normal distribution of the population might lead to inaccurate results. Hence we have to trust in the results derived from our non-linear statistical simulation.

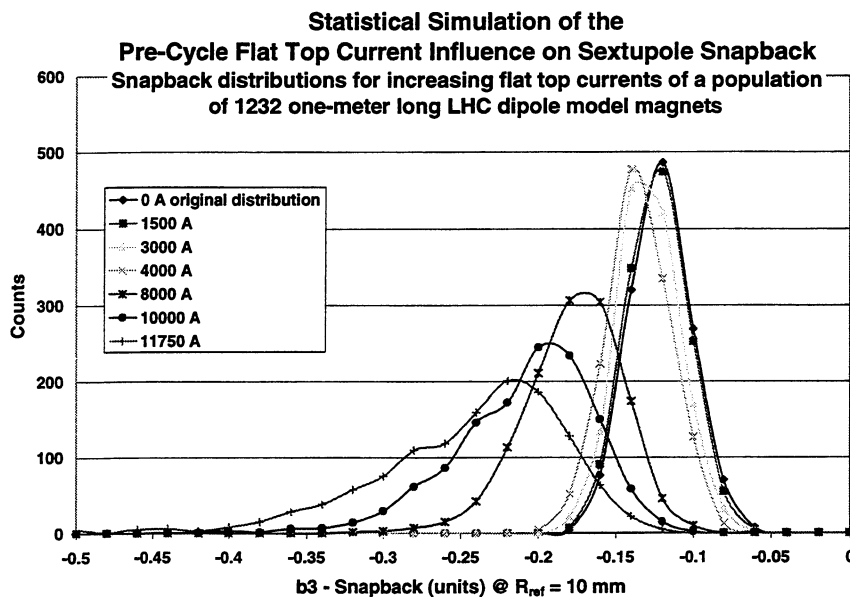


Figure 7.2: Evolution of the originally normal distribution of the population of magnets when simulating the flat top current influence on sextupole snapback with Equation 7.1.

7.4. Series Measurement Scenarios

In order to derive the accuracy of the mean of snapback, which depends on the number of measured magnets, we simulated series measurements by means of random sampling experiments on the base of our population of 1232 dipole magnets. The sample size was 20, 50, 100, 150, 200, 250, 300, 350, 400, and 500 magnets. Figure 7.3 shows a typical result of one of the sampling experiments for a sample size of 20 magnets.

For each sampling experiment we computed the mean of the snapback and the relative error in comparison to the reference values of the population for each current. In order to derive statistically significant numbers each sampling experiment with fixed sampling size (= one simulation of the series measurement) was repeated 50 times. The 50 relative errors were averaged. The standard deviation of this mean was finally plotted versus the sample number. Each flat top current was the parameter for one of the result lines plotted in Figure 7.4. Numerical results are shown in Table 7.4.

These numbers represent the expected accuracy (3σ) of the mean of the sextupole snapback as function of the flat top current and sample size. Due to the nonlinear functional extrapolation (see Equation 7.1) the accuracy depends not only on the sampling number but also on the flat top current. The accuracy of the mean of the sextupole snapback can now be connected with the precision of chromaticity control.

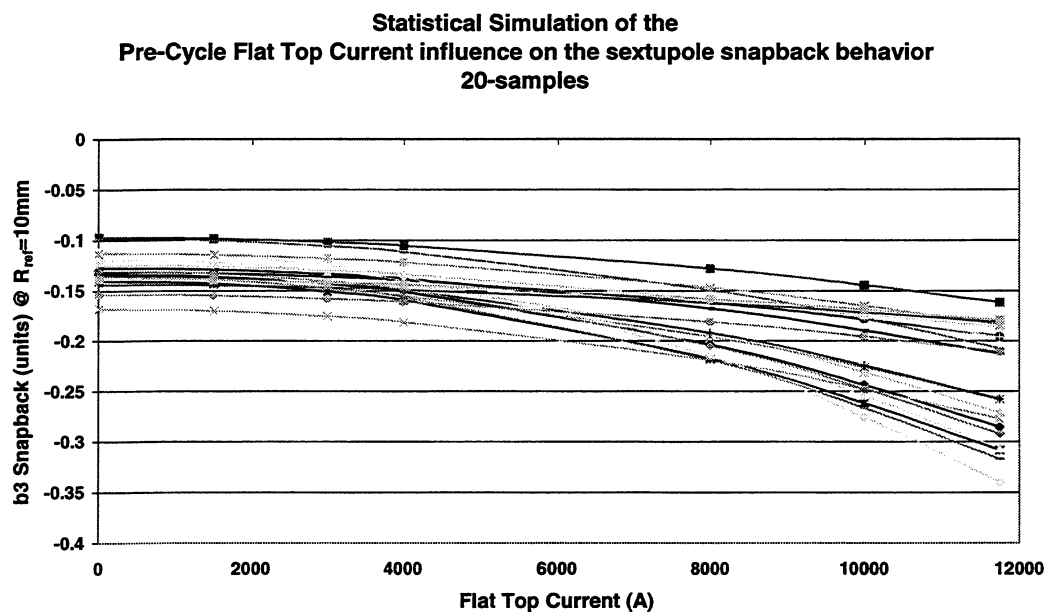


Figure 7.3: Demonstration of the sampling experiment for a sampling size of 20 magnets out of a population of 1232 one meter long LHC dipole model magnets.

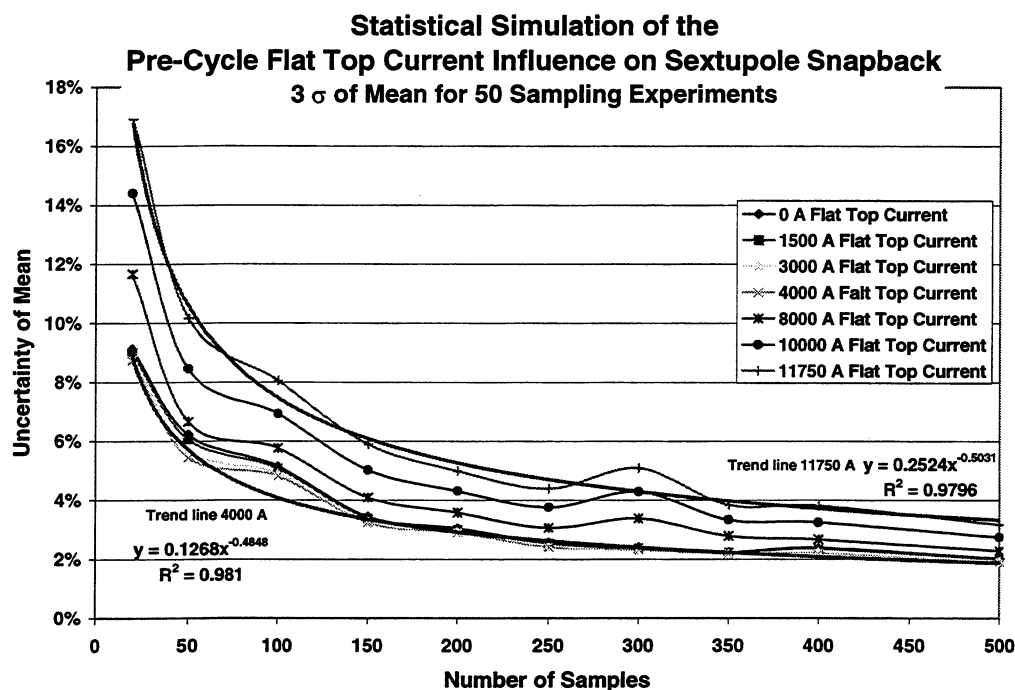


Figure 7.4: Sextupole snapback mean accuracy as function of the number of samples for different flat top currents. Each sampling experiment contains 50 samples of the population.

Table 7.4: Result table of the statistical simulation of the sampling experiment, which was carried through by generating a population of magnets, which underwent the Pre-Cycle Flat Top Current experiment. The numbers in the table show the relative error between mean of sampling experiments and mean of the population for a given flat top current. They are representative for a 3 σ uncertainty of the mean.

Samples	Pre-Cycle Flat Top Currents (A)						
	0	1500	3000	4000	8000	10000	11750
20	9.14%	9.01%	8.78%	8.76%	11.65%	14.41%	16.91%
50	6.22%	6.07%	5.70%	5.46%	6.66%	8.46%	10.16%
100	5.15%	5.07%	4.90%	4.82%	5.76%	6.93%	8.05%
150	3.44%	3.39%	3.28%	3.24%	4.09%	5.03%	5.90%
200	3.04%	3.00%	2.92%	2.89%	3.58%	4.31%	4.99%
250	2.56%	2.52%	2.44%	2.41%	3.06%	3.75%	4.39%
300	2.39%	2.36%	2.30%	2.32%	3.38%	4.29%	5.09%
350	2.23%	2.21%	2.18%	2.19%	2.78%	3.33%	3.83%
400	2.38%	2.34%	2.25%	2.20%	2.66%	3.25%	3.81%
500	2.01%	1.98%	1.92%	1.89%	2.28%	2.73%	3.16%

7.5. Conclusion

In this statistical simulation we proved that a possibly normal distribution of snapback measurements of a population of LHC magnets might evolve non-linear when running through the Pre-Cycle Flat Top Current experiment. Thus only a statistical simulation of the operation cycle variation experiments can illustrate the populations behavior.

According to the required accuracy of the mean we see that the 12 % threshold can already be achieved with approximately 50 measured magnets. Note that we defined the accuracy of 12 % as the 3σ limit. Furthermore the simulation shows that an accuracy of 2.4 %, which corresponds to a chromaticity control to a level of 1 unit, cannot be achieved under the given circumstances. Even though that the normal distribution of snapback at 0 A of the Pre-Cycle flat top current was mapped by a non-linear transformation we see that the measured accuracy still scales by the square root of the sample size. This result confirms the functional relation ship (Equation 7.1) between the accuracy of the mean and the required number of samples on the condition of a normal distribution of the population.

8. Conclusion of Decay and Snapback Studies

The major result of this work is a scaling law for the prediction of the decay respectively snapback in the LHC dipole magnets due to accelerator operation conditions. We summarize the main results in detail in the following paragraphs.

A statistical analysis of the behavior of the field components at injection showed that there is a systematics in decay and snapback only on allowed harmonics. The sign of the measured decay and snapback values for one allowed harmonic is consistent over the whole population of tested magnets. But the sign of the decay and snapback alters between different allowed harmonics. Non-allowed harmonics are randomly distributed in amplitude and sign. The decay of allowed harmonics is correlated during constant operation current excitation, e.g. injection. The observed correlation of the decay among different allowed harmonics might be an indication for a unique source of field component decay. This effect might be used to scale between allowed harmonics decay during injection. As far as the time constants of the field component decay are concerned we have seen that they agree with the theoretical models, but there are certain difficulties regarding the measurement technique.

According to the historical review and the theoretical publications the periodic pattern is most likely to be the reason for the field component decay. Today we are of the opinion that the unbalanced currents (*BICCs* or *supercurrents*) in the strands of the Rutherford type cable are the source of the field component periodicity. Those currents are established in parts of the magnet, where the cable is exposed to a spatial field sweep rate variation during ramps. The current imbalance decays during constant excitation. The decay of the unbalanced current is supposed to be the reason for the periodic pattern decay and the decay of integral field components during constant excitation. But we have to state that a complete theoretical framework does not yet exist.

In the results of the *Operation Cycle Variation Experiment* we found a very similar snapback behavior for magnets based on one of the two fundamental design concepts (five-block or six-block design). The snapback amplitude of the five-block design LHC dipole model magnets is consistent when operating the magnets under varied operation cycle conditions. The statistical analysis of the field component decay showed a significant correlation of the decay for the different allowed harmonics. The *Pre-Cycle Current Influence on Snapback Experiment* proved that the amplitude of the snapback shows this correlation under any varied operation cycle condition. As expected we found alternating signs among them but an equal trend for one operation cycle parameter variation.

The operation cycle influence on the allowed field component snapback cannot be modeled by simple polynomial fits to the data of each experiment. The reason for this is the complexity of the operation conditions during real LHC experiments. Hence we doubt if an accurate derivation of the parameters, their interaction and their non-linear dependence on the operation cycle variations is possible.

We established a phenomenological model for the dependence of the sextupole snapback on operation cycle variations for one-meter long LHC dipole model magnets with the five-block design. The model is based on the idea that the final decay at the end of the injection or the snapback at the beginning of the acceleration is due to a charging and discharging of an inductive-resistive circuit only. The empirical model is valid only for the twin aperture and single aperture model based on the five-block design. But even for this group of magnets we see some restrictions concerning the prediction quality. A measurement on six-block magnets revealed that at least one model parameter describing the coil geometry is missing.

A sufficiently accurate prediction was finally ensured by the use of artificial neural networks (ANNs). They learned proper prediction only from a small number of experiments and do not have any restrictions concerning their adaptation to particularities of design variations.

8.1. ANN Training, Testing and Implementation

Our positive experience regarding ANN's finally defined the course we held to as far as decay and snapback prediction is considered. The neural network approach appears to be the most successful and flexible tool for the precise prediction of decay and snapback due to magnet operation cycle variations.

The flexibility of the ANN system proves to be worthwhile regarding the hard and software implantation. The software we used for our ANN experiments allows studies of network behavior by use of MS-EXCEL tables as input, output and analysis device. The use of the MS-EXCEL interface allows an easy visualization of the results in form of charts. These features provide a high flexibility and transparence in data processing. Furthermore the software enables the conversion of the network structure into ANSI C++ code. This code can be used on different platforms. Thus the final time consuming training, cross verification and testing of a certain network structure can be performed on very powerful workstations. After finishing the training the network can be implemented into the correction system. At this level of implementation the network is provided with the actual operation cycle condition and can predict the snapback value. The computed snapback values can be processed by the conventional corrector system.

Due to the fact that different magnet and cable producers are involved in the construction of the LHC main bending dipoles, one should consider a strategy of implementing networks with different weights corresponding to the different production lines. But this strategy must be matched with other considerations like sorting strategies [81].

Finally we have to remember that the correction system of artificial neural intelligence, which learned to predict snapback by means of operation cycle variations from series and pre-series measurements, is based on the concept of offline training of the ANNs. Most probably one might also consider online learning of the network during the commissioning phase or the initial operation phase of the LHC. This possibility is only mentioned at this stage of the project and will not be dealt with in detail. A feasibility

study seems to be necessary. This study could finally show which of the two learning procedures leads to the most successful operation conditions of the LHC accelerator.

In summary, the success of the ANN in our experiments and the wide flexibility and reliability of the commercially available tools allow us to propose the implementation of a symbiosis of conventionally programmed and adaptive elements in the future dynamic effect correction system of the LHC accelerator.

8.2. Cold Measurements

We have shown that the required number of full characterizations of history effects by means of cold measurements can be limited to 50 magnets out of a population of 1232 dipoles in order to fulfil the conditions concerning the uncertainty limit of the snapback mean in respect to the chromaticity. A statistical simulation of the non-linear flat top current influence on the snapback resulted in this number.

8.3. Outlook

The experiments discussed in this work were focused on the decay and snapback of five-block design one-meter long LHC dipole model magnets. Future experiments should provide the statistics of field dynamics and the operation cycle variation influence on the allowed harmonics for short and long models and prototype magnets respectively, which are now based on the final six block coil design.

Performing a sufficient number of full characterization measurements should provide a reliable mean and sigma of the snapback. Based on this characterization further simulations of series measurements should cover all the operation cycle variations in order to provide a better estimation of the minimum required number of cold measurements in order to fulfil beam parameter requirements.

The snapback-scaling laws were derived by means of a measurement technique (rotating coils) that has no limited time resolution. A more precise parameterization of the snapback phase can be obtained by use of a hall plate based measurement system. Such a sextupole sensitive measurement system [103] was designed and is already in practical operation at LHC-MTA. First results of eddy current studies verified the principle of the design.

Besides improving the dynamic effects measurement technique and data modeling tasks concerning the accelerator operation respectively beam quality control requirements at LHC, some open questions regarding the physics of the observed phenomenon will have to be answered. In the scope of future theoretical and experimental work a closed formalism concerning current redistribution, periodic patterns and field component magnetization decay in the superconducting LHC magnets will be established.

9. Appendix I: Introduction to Neural Networks

Historically the interest in neural computing is based on the fascination of the human nervous system. The interactions of the basic neural elements have been the subject of various studies leading to fundamental knowledge about learning. In Figure 9.1 one can see a rough but very instructive time scale [85] of the research performed in this relatively new field of science.

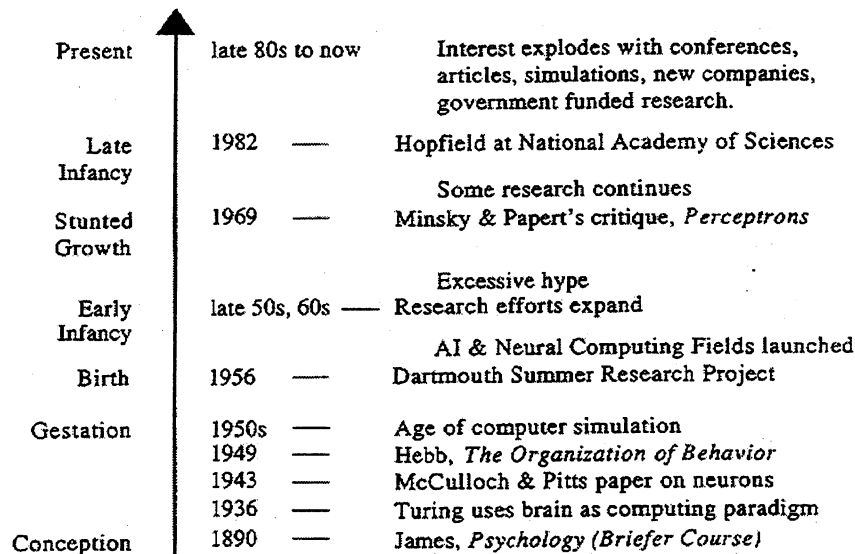


Figure 9.1: Rough time scale of the early years of neural network research showing the major milestones.

It lasted only 30 years, after having established the basic concepts and first "powerful" computers were available, until neural networks found their way into real world applications [86]. The dramatically increasing interest is mainly based on the fact that advanced learning rules for neural networks have been established. Thus a new capability of neural networks was recognized. Neural networks can offer solutions to problems that are very difficult to solve using traditional algorithmic decomposition techniques. The potential benefits of a neural network approach are [87]:

- ♦ **learning** from the interaction with the environment, rather than by explicit programming;
- ♦ **few restrictions** are placed on the type of functional relationship that can be learnt;
- ♦ **ability to generalize** (interpolate and extrapolate) the training information to similar situations.

Based on this flexibility the neural network is a strong tool that can be used in various applications. In recent years there have been a number of applications of neural networks to nuclear and high-energy physics for heavy quark tagging and event classification, jet identification, cluster detection, and nuclear spectroscopy. But these physics-related uses are just one specific case of a much larger class of applications in pattern recognition. For example there have been recent papers on the application of neural networks to

handwritten text recognition and segmentation; neural networks are applied to 3-D object classifications using visual, thermal, sonar, and radar signals, as well as face recognition. Other fields of research are speech recognition, speech translation and part-of-speech tagging. Furthermore we have to add robotics place learning and cartography to this list of technical applications.

Neural networks are also used in biological signal processing, medical image processing, and medical decision support.

The trend of using neural networks in economics became a "hot" topic approximately eight years ago when they were first applied to stock price prediction and stock selection. The list of applications mentioned above is not thought to be complete. It should rather give an idea of the usage of neural networks to the reader who is not familiar with this subject.

But before introducing a new application of neural networks in the field of prediction of dynamic effects in superconducting accelerator magnets, some insight into the fundamental principles of biology and the translation into neural computing should be gained.

9.1. Biological background

The basic item of the human nervous system is an individual cell called *neuron*. A typical neuron with its functional elements is shown in Figure 9.2. The neuron's structure, its elements and its ability to process information are discussed in the following section.

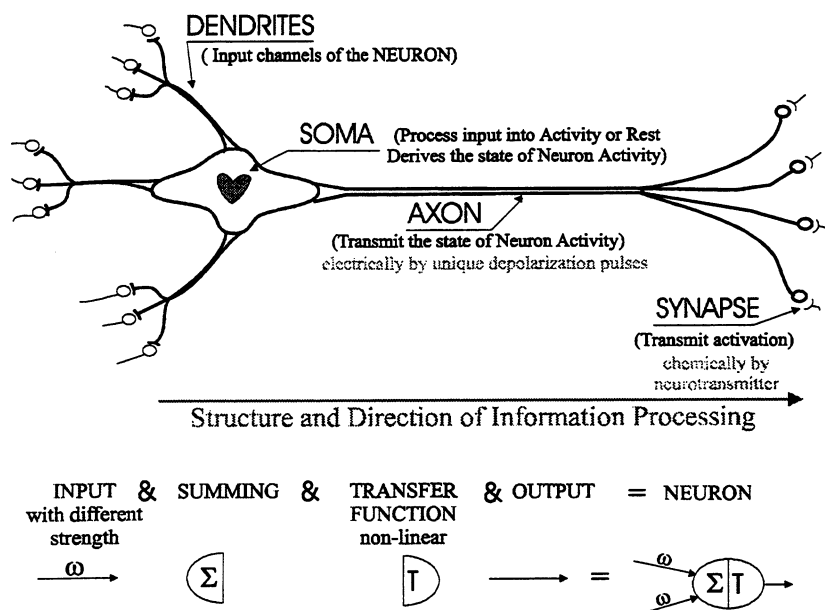


Figure 9.2: The biological neuron and its mathematical abstraction. The typical Multi Layer Perceptron structure consists of the network input, input layer, hidden layer, output layer and network output. The strength of interconnection between the nodes of the network is defined by weights, which have to be defined during the training period.

All our *sensory*, *motor* and *spiritual* properties are based on a sophisticated interconnection and interaction of an enormous number of these neurons. The total

number of neurons [86] in the human cortex is estimated to be about $3 \cdot 10^{10}$ to 10^{12} . This huge number of elements is distributed in layers over the full depth of the cortical tissue. Understanding the complex structure of the nervous system has been subject of several studies since the Middle Ages. It was soon revealed that the understanding of the brain functions requires detailed studies of its unique element. Systematic research was established after the invention of the electron microscope some 50 years ago. The basic neuron was found in all nervous structures. The *soma* (cell body) is connected with several *dendrites* on one end and to a single tubular fiber, the *axon* on the other end, which then splits into a number of small branches. The dendrites receive information from interconnected neurons and carry the impulses towards the cell body, while the axon transmits signals through its branches to other nerve cells or muscle fibers. The end of the axon branches and the corresponding following elements (either dendrites or cell body or axon of other cells) are separated by a small gap, called *synapse*.

The cell activity respectively inactivity is represented by a combination of electrical and chemical processes.

When not propagating an impulse the plasma membranes exhibit a voltage gradient - inside negative with respect to the outside - that is generated by transport proteins.

The value is determined by the concentration of certain ions in the exterior and interior (*protoplasm*) region of the neuron. Its value of -70 mV can be explained by the Goldman equation [5], which is an extension of the Nernst equation:

$$V = 58 \log \frac{P_K [K^+]_a + P_{Na} [Na^+]_a + P_{Cl} [Cl^-]_i}{P_K [K^+]_i + P_{Na} [Na^+]_i + P_{Cl} [Cl^-]_a} \quad (9.1)$$

Where P_x is the permeability for each type of ion and symbols in brackets indicate ion concentrations. For typical values of these concentrations see Table 9.1.

Table 9.1: Typical ion concentration [95] inside and outside of the axon [m mol / liter]

	<i>inside [i]</i>	<i>outside [a]</i>
K^+	400	20
Cl^-	30	590
Na^+	60	436
P^{2+}	high	very low
Legend: K^+ = Potassium ion, Cl^- = Chlorin ion, Na^+ = Sodium ion, P^{2+} = Protein ion		

Signals are initiated at synapses by depolarizations of the post-synaptic membrane's resting potential. This opens up Na^+ and K^+ -ligand-gated channels in the post-synaptic membrane and allows influx of Na^+ and efflux of K^+ along their electrochemical gradients. The potential difference immediately reaches a value between +30 to +40 mV. During the following recovering period the channels are restored to their closed state and the cell interior changes its polarity with respect to the exterior until it again reaches the resting potential of -70 mV. Finally the cell is ready to fire again.

The intensity of a nervous signal is encoded by the frequency of succession of the invariant depolarization pulses of activity.

The direction of the impulse transmission is the same in most neurons. The discharging process starts at the cell body, travels along the axon and reaches the synaptic gap. There the electrical signal is usually translated into a chemical signal based on

neurotransmitters. These transmitter substances pass the gap and are encoded by receptors in the post-synaptic cell membrane.

The influence of a given synapse on the activity of a post-synaptic cell depends on several effects. Its major contributions are the inherent strength of its depolarization effect, its location with respect to the cell body, and the repetition rate of the arriving signals. The mechanism of learning is strongly dependent on the plasticity of this neural connectivity. Originally postulated by Hebb [88], the so-called Hebb's rule says that the strength of a synaptic connection can be adjusted, if its level of activity changes. This emphasizes the importance of a synapse, which repeatedly triggers the activation of its post-synaptic neuron. Its synaptic strength will grow, while others will weaken.

The really important topic as far as learning is concerned, is the sophisticated subject of setting the strength of interconnections between neurons.

It is worth mentioning that neurobiology does not end at this point. But a deeper understanding of this matter is not really necessary for our experiment and would go beyond the scope of this publication. Finally one should mention that the current research is divided into two, not necessarily distinct, categories, which are focused on the devices of new theory regarding the brain's functionality and the application to real world problems.

After understanding the principle of learning in the natural system, we will now explore how this can be realized in a technical application called artificial neural network.

9.2. The Multi Layer Perceptron

In order to derive an artificial neural network we have to perform some symbolical as well as mathematical abstractions of the neuron. Based on the knowledge of biological properties we define the neuron by use of four basic elements. We need at least one adjustable input line. A summation unit adds up all the incoming signals. This sum signal must be transformed by a certain transfer function into an output signal. The simplification of the unique element of the nervous system is shown in the lower part of Figure 9.2. The representation of the learning ability requires a cluster of these neurons. A typical structure of such a cluster is shown in Figure 9.3.

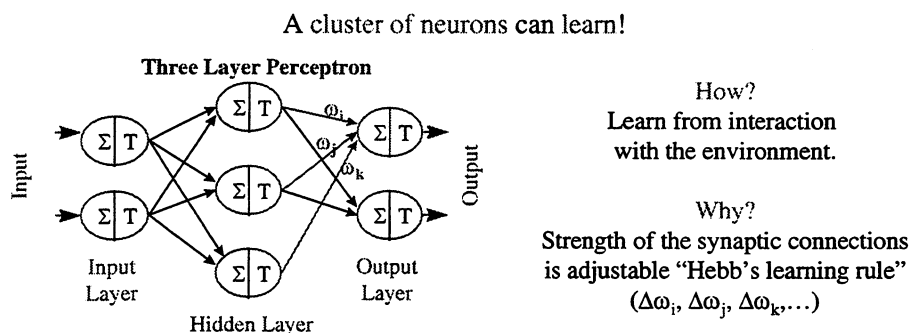


Figure 9.3: A cluster of neurons and its ability of learning - Hebb's learning rule.

The technical realization of the biological counterpart is generally called Artificial Neural Network (ANN). Biological properties must be translated into the language of information theory.

Thus we have to provide a definition of an ANN [86]:

A neural network model is defined as a directed graph with the following properties:

- A state variable n_i is associated with each node i .
- A real value weight ω_{ik} is associated with each link (ik) between two nodes i and k .
- A real-value bias (activation threshold) ϑ_i is associated with each node i .
- A transfer function $f_i[n_k, \omega_{ik}, \vartheta_i, (k \neq i)]$ is defined for each node (neuron) i ; it determines the state of the node as a function of its bias, of the weights of its incoming links (synapses), and of the node connected by these links.

The transfer function usually takes the form

$$f\left(\sum_k \omega_{ik} n_k - \vartheta_i\right), \quad (9.2)$$

where $f(x)$ is either a discontinued step function or a smoothly increasing generalization known as a sigmoidal (see Figure 9.4 c) function. Some other possible transfer functions are shown in Figure 9.4 a, b, d [85]. All of these transfer functions map the input from $\pm \infty$ to a bounded interval (i.e. $[0, 1]$ or $[-1, 1]$).

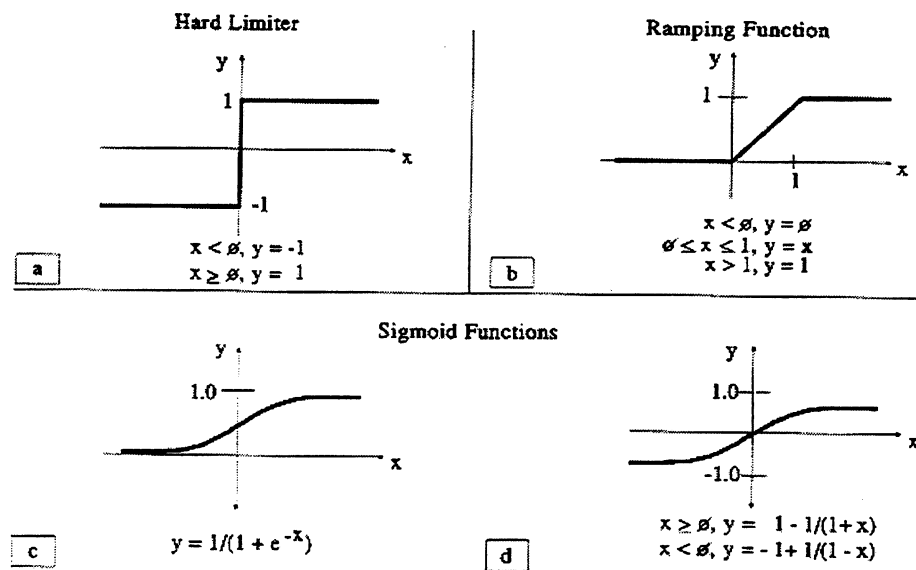


Figure 9.4: Some different transfer functions commonly used in ANNs.

Input neurons are nodes without links (synaptic connection) towards them, while output neurons are nodes without links away from them.

A network structure without closed path is a so-called feed forward network. This network topology may consist of several layers of neurons and is named multi layer perceptron. Around 1960 Frank Rosenblatt et al., who studied in detail a simple perceptron consisting of two layers, introduced the name perceptron [89]. This structure was supposed to be a simplified model of the biological mechanism of processing sensory information, i.e. perception. After more than 20 years the interest in layered feed forward networks suddenly increased. This was due to the discovery of an efficient

algorithm for the determination of the synaptic coupling strength. This learning algorithm is based on an iterative modification of the synaptic strength in order to minimize the difference between desired output and network output. This so-called error back-propagation, reinvented by several groups of scientists [90] [91], is based on a gradient method yielding to a required modification of synaptic strength. But this method is just one of a much bigger class of learning algorithms which are classified as supervised learning. This method of learning is only available if the desired output is already known in advance. This means that one has to explore at first the complex behavior of the physical system, which is the subject of the studies. Analyzing this behavior and considering that no analytical description can be derived due to the strong and obviously unknown nonlinear effect of this system on its variables one might have a good chance to apply a multi layer perceptron to solve this problem of modeling. Using a continuous transfer function in each node of the network leads to a continuous dependency of the output on the network's input. This continuous transfer function is e.g. a sigmoidal transfer function.

Under this condition the network might be used as a universal non-linear approximator. In 1989 Hornik et al. established [92] that any continuous nonlinear function can be approximated to within an arbitrary accuracy by a three-layer multi perceptron with sufficient nodes in the hidden layer. This property is extended to logical functions by choosing appropriate weight vectors and activation functions [93]. Therefore the basic structure of the multi layer perceptron is very flexible and can be employed in a wide variety of modeling and control tasks.

Especially in our situation, in which measurement time is very limited, it is of high interest that the network seems capable of learning poorly understood, high-dimensional functions from only a small amount of training data [94]

In the chapter of modeling snapback we showed how the ability of a supervised-trained neural network was adapted to the problem of snapback prediction for a superconducting dipole magnet.

References

- [1] CERN the world's leading particle physics research laboratory, Communication & Public Education Group, CERN, April 1996
- [2] LEP the large electron positron collider, Communication & Public Education Group, CERN, January 1997
- [3] Forty-first Annual Report of the European Laboratory of Particle physics, Volume 1, Communication & Public Education Group, CERN, Geneva, 1996
- [4] Forty-third Annual Report of the European Laboratory of Particle physics, Volume 1, Communication & Public Education Group, CERN, Geneva, 1998
- [5] K. Wille, Physik der Teilchenbeschleuniger und Synchrotronstrahlungsquellen, Teubner Studienbücher, Physik, 2nd Edition, ISBN 3-519-13087-4, Stuttgart, 1996
- [6] J. le Duff, High Luminosity, CAS, Fifth advanced accelerator physics course, CERN, 94-06, Vol. 1, 515-537, 22 November 1995
- [7] Eberhard Keil, The CERN Large Hadron Collider LHC, LHC Project Report 83, Geneva, December 6, 1996
- [8] R.L. Evans, The Large Hadron Collider Project, ICEC16, Kitakyushu, Japan, 20-24 May 1996, LHC Project Report 53, Geneva, 20 September 1996
- [9] R. Perin, Superconducting Magnets for the Large Hadron Collider, 10th General Conference of the European Physical Society, September 9-13, 1996, Sevilla, Spain, LHC Project report 52, Geneva, October 8, 1996
- [10] The Large Hadron Collider - Conceptional Design, CERN/AC/95-05 (LHC), 20 October, 1995
- [11] LHC - The Large Hadron Collider - Accelerator Project, CERN/AC/93-03 (LHC), 8 November 1993.
- [12] Design Study of the Large Hadron Collider (LHC) - A multiparticle collider in the LEP tunnel, CERN 91-03, Geneva, 2 May 1991.
- [13] D. Richter, DC measurement of electrical contacts between strands in superconducting cables for the LHC main magnets, IEEE Trans. Appl. Supercond. : 7 (2) (1997) (786-792). 1996, LHC-Project-Report-67, Geneva, 1996
- [14] L.R. Evans, LHC Status Plan, Particle Accelerator Conference, Vancouver, 12-16 May 1997, LHC-Project-Report-101, Geneva, 1997
- [15] M.N. Wilson, Calculation of minimum quench energy in the Rutherford cable, Presented at ASC '96, Pittsburgh, 1996
- [16] A.P. Verweij, Review on Boundary-induced Coupling Currents, Presented at CEC/CMC '97, Portland, USA, LHC-Project-Report-152, Geneva, 5 November 1997
- [17] M. Martini, Transverse Beam Dynamics, Joint Universities Accelerator School, Archamps, 1998.
- [18] Superconducting Super Collider - Conceptual Design, SSC-SR-2020, March 1986.
- [19] C. Paul, Numerical Calculation of the Saturation Induced Field Errors in the Main Dipole of CERN's future Large Hadron Collider, PhD thesis, Fakultät für Elektrotechnik, Technische Universität Graz, September 1997.
- [20] R. Wolf, The Decay of the Field Integral in Superconducting Accelerator Magnets Wound with Rutherford Cables, 15th International Conference on Magnet

- Technology : MT-15 Beijing, China ; 20 - 24 Oct 1997, LHC Project Report 175, Geneva, 14 May 1998
- [21] R. Wolf, Persistent Currents in the LHC Magnets, Presented at the 12th International Conference on Magnet Technology, Leningrad, 23-28 June, 1991
 - [22] T. Ogitsu, influence of Cable Eddy Currents on the Magnetic Field of Superconducting Particle Accelerator Magnets, PhD, Institute of Applied Physics, Tsukuba, Japan, 1994
 - [23] P. Proudlock, LHC Workshop on Dynamic Effects and Their Control, CERN, Geneva, 5-7 February 1997
 - [24] R. Bailey, Dynamic Effects and their Control at the LHC, LHC-Project-Report-124, CERN, Geneva, 1997
 - [25] J. Gareyte, Accelerator Physics Issues of the LHC, Invited paper - 5th European Particle Accelerator Conference, EPAC96, Sitges, (Barcelona), Spain, 10-14 June 1996, LHC-Project-Report-10, Geneva, 5 August, 1997
 - [26] J.P. Koutchouk et al., Overview of the LHC Dynamic Aperture Studies, Subm. to:1997 Particle Accelerator Conference : PAC '97 Vancouver, Canada ; 12 - 16 May 1997, LHC-Project-Report-106, Geneva, 1997
 - [27] R. Bartolini, W. Scandela, Sorting Strategies for the LHC Dipoles, Subm. to:1997 Particle Accelerator Conference : PAC '97 Vancouver, Canada ; 12 - 16 May 1997, LHC-Project-Report-117, Geneva, 11 June, 1997
 - [28] Accelerators at Fermilab, <http://www.fnal.gov/pub/accelerator.html>
 - [29] J. Rossbach, P. Schmüser, Basic course on accelerator optics, CAS, Fifth general accelerator physics course, CERN 94-01, Vol. 1, 17-115, 26 January 1994
 - [30] S. Guiducci, Chromaticity, CAS, Fifth general accelerator physics course, CERN 94-01, Vol. 1, 191-206, 26 January 1994
 - [31] E.J.N. Wilson, Non-linearities and resonances, CAS, Fifth general accelerator physics course, CERN 94-01, Vol. 1, 239-251, 26 January 1994
 - [32] J. Buon, Beam phase space and emittance, CAS, Fifth general accelerator physics course, CERN 94-01, Vol. 1, 89-115, 26 January 1994
 - [33] A.D. Finley et al., Time dependent chromaticity change in the Tevatron, Proc. of 87 Part. Acc. Conf., Washington, 151-153, March 16-19, 1987
 - [34] D.E. Johnson and D.A. Herrup, Compensation of time varying Fields in the Tevatron Superconducting Magnets, Proc. of 89 Part. Acc. Conf., Chicago, 521-523, March 20-23, 1989
 - [35] D.A. Herrup et al., Time-Varying sextupole corrections during the Tevatron Ramp, Proc. of 89 Part. Acc. Conf., Chicago, 518-520, March 20-23, 1989
 - [36] D.A. Herrup et al., Time variations of field in Superconducting magnets and their effects on accelerators, IEEE Trans. Mag., Vol. 25, No. 2, 1643-1646, March, 1989
 - [37] R.W. Hanft et al., Studie of time dependence of field in Tevatron superconducting dipole magnets, IEEE Trans. Mag., Vol. 25, No. 2, 1647-1651, March, 1989
 - [38] SSC Newsletter, Volume1, Number 1, November 12, 1984
 - [39] M. Barnett, <http://het.brown.edu/news/ssc/sscdead.html>
 - [40] The Drell Report - HEPAP'S Subpanel on Vision for the Future of High-Energy Physics, DOE/ER-0614P, <http://www.hep.net/ftp/mirrors/ssc/new/history/fullreport.html>, Washington, DC, USA, May 1994

- [41] W.S. Gilbert et al., The effect of flux creep on the magnetization filed in the SSC dipole magnets, SSC-MAG-244 and LBL-26598, June 1989
- [42] DESY in FOCUS, http://www.desy.de/pr-info/desy-fokus_e.html
- [43] H. Brueck et al., Time dependence of persistent current effects in the superconducting HERA magnets, Contribution to the 11th International Conference on Magnet Technology - MT-11, Japan, Aug. 28 - Sep. 1, 1989, and HERA 90-01, January, 1990
- [44] H. Brueck et al., Time dependence of persistent current field distortions in the superconducting HERA magnets, presented at EPAC-1990, Nice, June 12-16, 1990
- [45] H. Brueck et al., Time dependent filed distortions from magnetization currents in the superconducting HERA magnets, Cryogenics, Vol. 30, Supplement, 605-609, September, 1990
- [46] R. Meinke, Superconducting magnet system for HERA, IEEE Trans. Mag., Vol. 27, No. 2, 1728-1734, March, 1991
- [47] H. Brueck et al., Observation of periodic pattern in the persistent current filed of the superconducting HERA magnets, Reports at the 12th International conference on magnet technology, Leningrad, USSR, June 24-28, 1991, and DESY HERA 91-11, July, 1991
- [48] N.L. Smirnov, The methods of UNK SC-dipoles magnetic measurement, IHEP 91-178, 1991
- [49] M. Wake, Test of 1.5 meter model 50 mm SSC collider dipoles at Fermilab, Conference record of the 1991 IEEE Particle Accelerator Conference, Vol. 4, 2173-2175, 1991
- [50] A. Devred et al., Time decay measurements of the sextupole component of the magnetic field in a 4 cm aperture, 17 m long SSC dipole magnet prototype, SSCL-462, May, 1991, and FERMILAB-Conf-91/148
- [51] R. Stiening, A possible mechanism for Enhanced Persistent Current Sextupole Decay in SSC Dipoles
- [52] M. Halemeyer, Eine neue Methode zur Bestimmung der Megnetisierung von supraleitendem Kabel und ihre Zetabhängigkeit, Diploma, II. Inst. f. Exp.-phys. d. Univ. Hamburg, March, 1992, and DESY HERA 92-13, March, 1992
- [53] O. Meincke, Messung und Kontrolle der Q-Werte und Chromatizitäten im HERA-Proton-Ring, Diploma, II. Inst. F. Exp.-phys. d. Univ. Hamburg, April, 1992, and DESY HERA 92-08, April, 1992
- [54] A.K. Ghosh et al., Axial varaitions in the magnetic field of superconducting dipoles, Supercollider 4, Edited by J. Nonte, Plenum Press, New York, 765-772, 1992
- [55] A.K. Ghosh et al., Time dependent magnetization effects in superconducting accelerator magnets, 15th International Conference on High Energy Accelerators, Vol. 2, 665-667, July 20-24, 1992
- [56] A.K. Ghosh et al., Axial Varaitions in the magnetic fied of superconducting dipoles and quadrupoles, PAC '93, 2742-2744, 1993
- [57] W.B. Sampson and A.K. Ghosh, Induced axial oscillations in superconducting dipole windings, ASC-94
- [58] A.K. Ghosh, The ramp rate dependence of sextupole field in superconducting dipoles, IEEE Trans. Mag., Vol. 30, No. 4, 1718-1721, July, 1994

- [59] J. Buckley et al., Dynamic magnetic measurements of superconducting magnets for the LHC, ASC '94, Boston, October 16-21, 1994, and CERN LHC Note 294
- [60] L. Bottura et al., Field errors decay and "Snap-Back" in LHC model dipoles, CERN-LHC-Project-Report-55, Geneva, 1996
- [61] L. Bottura, Experimental evidence of boundary induced coupling currents in LHC prototypes, Presented at 1996 Applied Superconductivity Conference, Pittsburgh, Pa, August 25-30, 1996
- [62] L. Bottura, Field Dynamics in superconducting magnets for particle accelerators, CAS, Anacapri, Italy, 4. Aug. 98, CERN 98-05
- [63] B.J. Holzer, Impact of persistent currents on accelerator performance, Particle Accelerators, Vol. 55, [461-471] / 215-225, 1996
- [64] H. Brueck et al., Correction of the influence of persistent currents in the HERA proton ring, EPAC '96, 392-394, 1996
- [65] The 1 m long single aperture dipole coil test program for LHC, CERN-LHC-Project-Report-25
- [66] S. Russenschuck, Comparative Study of Different Coils for the LHC Main Dipoles, CERN-LHC-Project-Report-159, Geneva, 1997
- [67] N. Andeev, Present State of the Single and Twin Aperture Short Dipole Model Program for the LHC, CERN-LHC-Project-Report-177
- [68] L. Walckiers, The harmonic coil methode, CAS, Hyatt Conference Centre, Montreux, Switzerland, CERN 92-05, 16-20 March 1992
- [69] A. Devred, Rotating Coil Arrays for Magnetic Measurements of Superconducting Particle Accelerator Magnets, Commissariat à l'Energie Atomique/Saclay, Service des Techniques de Cryogénie et de Magnétisme, 91191 Gif-sur-Yvette Cedex, France
- [70] L. Bottura, Standard Analysis Procedures for Field Quality Measurement of the LHC Magnets - Part I: Harmonics, CERN LHC MTA Internal Note, MTA-IN-97-007, Geneva, 1997
- [71] I. Bejar, Measurement of AC Loss and Magnetic Field during Ramps in the LHC Model Dipoles, CERN-LHC-Project-Report-241, Geneva, 1998
- [72] H.W. Weber, O. Hittmair, Supraleitung, ISBN-3-521-06113-2, Verlag Karl Thimig, München, 1979
- [73] E.W. Collings, *Applied Superconductivity, Metallurgy, and Physics of Titanium Alloys*, Vol.1, Fundamentals, ISBN 0-306-41690-6, Plenum Press, 1986
- [74] E.W. Collings, *Applied Superconductivity, Metallurgy, and Physics of Titanium Alloys*, Vol.2, Applications, ISBN 0-304-41691-3, Plenum Press, 1986
- [75] A. Akhmetov, Test & Analysis Note, SSCL, MD-TA-239, January 5, 1993
- [76] A.P. Verweij, Electrodynamics of Superconducting Cables in Accelerator Magnets, Ph.D., ISBN 90-9008555-6, Twente University (NL), 1995
- [77] L. Krempasky, C. Schmidt, Theory of "supercurrents" and their influence on field quality and stability of superconducting magnets, J. Appl. Phys. 78 (9), 5800-5810, 1 November 1995
- [78] L. Krempasky, C. Schmidt, Influence of a longitudinal variation of dB/dt on the magnetic field distribution of superconducting accelerator magnets, Appl. Phys. Lett 66 (12), 1545 - 1547, 20 March 1995

- [79] L. Krempasky, C. Schmidt, A possible explanation of the problem of ramp rate limitation in large superconducting magnets, IEEE Transactions on Magnetics, Vol. 32, No 4, 2340 - 2344, July 1996
- [80] L. Krempasky, R. Bussjäger, C. Schmidt, Experimental verification of supercurrents induced in superconducting cables exposed to AC-field, presented at the 15th Intern. Conf. on Magnet Technology (MT-15), paper OF1-6, Beijing, China, Oct. 1997
- [81] R. Bartolini, M. Giovannozzi, W. Scandale, E. Todesco, Test of the sorting methods at the CERN-SPS, LHC-Project Reoprt 38, Geneva, Switzerland, 29 July, 1996.
- [82] Lothar Sachs, Statistische Methoden - Ein Soforthelfer, Springer-Verlag, Titel-Nr. 1701., 1970
- [83] W.H. Press, B.P. Flannery, S.A. Teukolsky, W.T. Vetterling, Numerical Recipes - The Art of Scientific Computing (Fortran Version), Cambridge University Press, ISBN 0 521 38330 7, 1990.
- [84] P.M. Mills, A.Y. Zomaya, M.O. Tade, Neuro-Adaptive Process Control - A Practical Approach, John Wiley & Sons Ltd, ISBN 0 471 95997 9.
- [85] M. McCord Nelson, W.T. Illingworth, A practical guide to Neural Nets, Addison-Wesley Publishing Company, ISBN 0-201-52376-0, Sixth Printing, January 1994.
- [86] B. Mueller, J. Reinhardt, M.T. Strickland, Neural Networks An Introduction, 2nd Edition, Springer, ISBN 3-540-60207-0, 1995.
- [87] Martin Brown & Chris Harris, Neurofuzzy adaptive modelling and control, Prentice Hall International (UK), ISBN 0-13-134453-6, 1994.
- [88] D.O. Hebb, The organization of behaviour, New York, Wiley, 1949.
- [89] F. Rosenblatt, Principles of Neurodynamics: Perceptron and the Theory of Brain Mechanism, Washington DC, Spartan, 1961.
- [90] D.E. Rumelhart, J.L. McClelland, Parallel Distributed Processing: Exploration in the Microstructure of Cognition, Vol 1, MIT Press, Cambridge, MA, 1986.
- [91] D. Parker, Learning Logic, Tech. Report, TR-47, Center for Computational Research in Economics and Management Science, MIT, MA, 1985.
- [92] K. Hornik, M. Stinchcombe, H. White, Multilayer Feedforward Networks are Universal Approximators, Neural networks, Vol. 2, pp. 551-560, 1989.
- [93] S.W. Ellacott, Aspects of Numerical Analysis of Neural Networks, Acta Numerica, pp. 145-202, 1994.
- [94] W.A. Wright, Neural Networks for Military Robots, Agard Lecture series 179, Artificial Neural Network Approaches in Guidance and Control, Chapter 7, 1991.
- [95] Richard F. Thompson, Das Gehirn - Von der Nervenzelle zur Verhaltenssteuerung, Spektrum der Wissenschaft, Heidelberg, ISBN 3-89330-696-X, 1990.
- [96] NeuroSolution by NeuroDimension, Inc., <http://www.nd.com>.
- [97] M. Schneider, L. Bottura, Time Dependent Effects in the MBSMS series magnets, CERN LHC Internal Note, MTA-IN-96-011, Geneva, October 18, 1996
- [98] M. Schneider, L. Bottura, "Decay analyses in 1 m long LHC dipole magnets", CERN LHC Internal Note, MTA-IN-97-004, Geneva, May 15, 1997
- [99] M. Schneider, L. Bottura, "High pre-cycle current influence on decay in the 1 m long LHC dipole model magnet MFISC V2", CERN LHC Internal Note, MTA-IN-97-005, Geneva, May 15, 1997

- [100] M. Schneider, L. Bottura, "Time Dependent Effects on the one meter long LHC dipole model magnets: MBSMS9V1, MBSMS10,V1, MBSMS11V1 and MBSMT1V1", CERN LHC Internal Note, MTA-IN-97-013, Geneva, November 1, 1997
- [101] M. Schneider, L. Bottura, "Snapback Scaling Laws for the superconducting one meter long LHC dipole model magnets", CERN LHC Internal Note, MTA-IN-1998-045, Geneva, August 27, 1998
- [102] L. Bottura, M. Schneider, L. Walckiers, R. Wolf, "Cable Magnetization Effects in the LHC Main Dipole Magnets", to appear in Adv. Cryo. Eng., 1998.
- [103] M. Schneider, N. Smirnov, Dynamic Effects in the LHC Dipole Magnets - The Hall Probe Sextupole Measurement System Part I, CERN LHC Internal Note, MTA-IN-98-042, Geneva, June 15, 1998